CARBON NANOTUBE FIBERS: MECHANICAL BEHAVIOR AND THE EFFECTS OF THE SPACE ENVIRONMENT

Ryan A. Kemnitz, Major, USAF

AFIT-ENY-DS-18-D-036

DEPARTMENT OF THE AIR FORCE
AIR UNIVERSITY

AIR FORCE INSTITUTE OF TECHNOLOGY

Wright-Patterson Air Force Base, Ohio

AFIT-ENY-DS-18-D-036

CARBON NANOTUBE FIBERS: MECHANICAL BEHAVIOR AND THE EFFECTS OF THE SPACE ENVIRONMENT

DISSERTATION

Presented to the Faculty

Department of Aeronautics and Astronautics

Graduate School of Engineering and Management

Air Force Institute of Technology

Air University

Air Education and Training Command

In Partial Fulfillment of the Requirements for the

Degree of Doctor of Philosophy

Ryan A. Kemnitz, BS, MS

Major, USAF

October 2018

AFIT-ENY-DS-18-D-036

CARBON NANOTUBE FIBERS: MECHANICAL BEHAVIOR AND THE EFFECTS OF THE SPACE ENVIRONMENT

Ryan A. Kemnitz, BS, MS

Major, USAF

Committee Membership:

Dr. Carl Hartsfield
Chair

Dr. Richard Cobb
Member

Dr. Benjamin Akers
Member

ADEDJI B. BADIRU, PhD
Dean, Graduate School of Engineering and Management

AFIT-ENY-DS-18-D-036

Abstract

Carbon nanotube materials are promising multifunctional materials for incorporation into aerospace structures because of their high tensile strength, high electrical conductivity, and low density. This research aimed to characterize the mechanical failure mechanisms of carbon nanotube fibers and examine the effects of the space environment on their material properties. Tensile tests were conducted at varying strain rates and on fibers of varying gage lengths to examine the underlying failure mechanisms and impact of the fiber microstructure on fiber strength. Tensile strength and elastic modulus were observed to increase with increasing strain rate and decrease with increasing gage length. The observed effects were similar to those observed for polymeric fiber materials. Atomic oxygen exposure was found to severely degrade the tensile strength and electrical conductivity of CNT yarns after an exposure equivalent to one year in Low Earth Orbit. Intense ultraviolet radiation did not significantly impact the mechanical or electrical properties of the fibers after an exposure equivalent to 3 years in Low Earth Orbit.

Acknowledgments

I would like to express my heartfelt gratitude to my wife for her encouragement and support for these years during my research. I am indebted to Dr. Shankar Mall for his accepting me as his final doctoral student and providing me with support and guidance in the beginning of my studies. I am also indebted to Dr. Carl Hartsfield for becoming my research advisor after Dr. Mall's death and guiding me through the remainder of my doctoral program. I owe thanks to my research committee, Dr. Richard Cobb and Dr. Benjamin Akers, for their insightful comments and careful reading of my research. Finally, I am indebted to the excellent lab technicians of AFIT and AFRL for their expertise and support in my research: Scott Apt, Josh Dewitt, Keith Long, Mike Ranft, Jamie Smith, and Greg Smith.

Ryan A. Kemnitz

Table of Contents

Page

List of Acronyms

AFIT – Air Force Institute of Technology

AIC – Akaike Information Criterion

AO – Atomic Oxygen

CDF – Cumulative Distribution Function

CNT – Carbon Nanotube

CSA – Chlorosulfonic Acid

CV – Coefficient of Variation

FIB – Focused Ion Beam

GEO – Geosynchronous Orbit

GF – Gauge Factor

KS – Kolmogorov-Smirnov

LD – Linear Density

LEO – Low Earth Orbit

LVDT – Linear Variable Differential Transducer

MEO – Medium-Earth Orbit

ML – Maximum Likelihood

MLE – Maximum Likelihood Estimator

MWNT – Multi-wall Carbon Nanotube

SEM – Scanning Electron Microscope

SWNT – Single-wall Carbon Nanotube

UV – Ultraviolet Radiation

List of Figures

List of Tables

CARBON NANOTUBE FIBERS: MECHANICAL BEHAVIOR AND THE EFFECTS OF THE SPACE ENVIRONMENT

I. Introduction

Materials for Aerospace Electromechanical Applications

Carbon nanotubes (CNTs) are very small cylindrical molecules with exceptional strength and electrical conductivity. CNTs are only a few nanometers wide and a few micrometers long. CNTs can be assembled into solid fibers composed of only CNTs which are aligned along the length of the fiber. CNT fibers are quickly approaching the tensile strength of the strongest carbon fibers and the electrical conductivity of the most conductive metals, while having a similar density as carbon fibers. The low density of these materials makes them desirable for spacecraft design where reducing mass is a priority due to the high cost of launching objects into space. There remains a need to characterize how and why these CNT fibers fail and how their properties are affected by the space environment to assess their suitability for space applications.

Copper is one of the most widely used electrical conductors because of its high electrical conductivity and ductility. Copper's primary disadvantage is its relatively high density, 8.94 g/cm^3. CNT fibers may become drop in replacements for copper wires because of their high electrical conductivity and lower density, 1.5 g/cm^3. CNT fibers are woven into CNT yarns to carry higher currents or mechanical stresses. Recent research in CNT fiber synthesis has demonstrated a fiber with an electrical conductivity 83% less than that of copper [1]. The replacement of copper with CNT fibers may translate into an 85% decrease in mass of electrical power and data transmission cables. Several research

groups have already demonstrated that current CNT materials can successfully operate as drop in replacements for electrical conductors in military grade cables [2] [3] [4].

A critical factor in the deployment of space systems is the cost to launch them into orbit. Launch into Low Earth Orbit (LEO) ranges between $6,000-$20,000/kg [5]. Prices for launch into Geosynchronous Orbit (GEO) from a 2003 survey of then-recent launches ranged from $16,000-$60,000/kg [6]. Replacing copper with CNT fibers may save hundreds of kilograms on a large military or scientific spacecraft which would allow satellite designers to include larger, more sophisticated sensors, more fuel to extend mission life, increase spacecraft component redundancy, or simply make satellite launches more affordable by moving to a smaller launch vehicle.

Mass savings alone may motivate the adoption of CNT fiber wiring replacements in spacecraft design. The same argument cannot be made for replacing carbon fibers with CNT fibers in composite structures. CNT fibers are as strong as many commercially available carbon fibers and fiber synthesis research indicates CNT fibers may achieve the same strength as the strongest carbon fibers [1]. However, CNT fibers and carbon fibers have approximately the same density. The primary advantage of CNT fibers over carbon fibers is their electrical conductivity. CNT fibers are 1-2 orders of magnitude more conductive than carbon fibers [7]. This combination of properties may enable CNT fibers to serve multiple roles simultaneously in spacecraft, such as structural reinforcement and strain sensing, or power and data transmission.

The design possibilities for a material with such a unique combination of exceptional properties is exciting, but characterization of failure causes and mechanisms in CNT fibers is lacking. Also, the effects of the space environment on CNT fibers are

not well characterized. There is a tremendous amount of work that is needed to understand the behavior of CNT fibers to assess their suitability for space applications.

Problem Statement

There are multiple factors which affect the mechanical behavior of fibrous materials such as microstructural defects, fiber microstructure, and environmental effects which may modify the former factors. The impact of these factors on the behavior of state-of-the-art CNT fibers are not well characterized. This research attempts to characterize the effects of these factors to inform spacecraft design engineering on the proper utilization of CNT fibers.

Research Objectives

1. Determine the effects of microstructural fiber defects on the mechanical properties of CNT fibers and whether these defects give rise to a relationship between fiber length and tensile strength.
2. Determine the effect of the fiber microstructure on the strain rate dependence of short-term mechanical properties and the static loading behavior of CNT fibers.
3. Determine the effects of the space environment on the material properties of CNT fibers.

Material Description

CNT fibers and yarns used in this research were purchased from Dexmat (Houston, TX) [8]. Initially, a three-ply, 21 fiber yarn was purchased from Dexmat in October 2016. This yarn was used for the space environment characterization study. A

second yarn composed of 7 fibers was obtained in 2018 for the single fiber testing. Properties of each are summarized in Table 1.

Table 1: Material Properties [8]

Supplier	Dexmat (2016)	Dexmat (2018)
Yarn Construction	3 ply/ 7 filaments/ply	Single ply/ 7 filaments
Diameter (μm)	113 +/- 5	22.10 +/- 1.01
Linear density (tex)	7.4	0.50 +/- 0.045
Density (g/cm^3)	0.75	1.3
Electrical Conductivity (MS/m)	2.81	N/A
Specific Conductivity ($S\ m^2/kg$)	3750	N/A
Tensile Strength (GPa)	0.83 +/- 0.040	1.044 +/- 0.093

Methodology

The objectives outlined in the problem statement were accomplished by the following tasks:

1. Determine the effect of gage length[1] on the mechanical behavior of CNT fibers by tensile testing single fibers of varying lengths at the same strain rate and examining the microstructure of untested and tested fibers.

[1]Gage length is defined as the length of material being stressed also known as the length of material between the grips of a tensile testing machine or the length between the locations where the material is cemented on gripping tabs

2. Determine the effect of strain rate on the mechanical behavior of CNT fibers by tensile testing single fibers at varying strain rates and static loading single fibers and examining the microstructure of untested and tested fibers.
3. Determine the effect of ultraviolet light and atomic oxygen exposures on the electrical and mechanical properties of CNT fibers by conducting the following analyses on terrestrially exposed specimens.
    a. Tensile testing
    b. Conductivity measurements
    c. Piezoresistance measurements
    d. Raman spectroscopy
    e. Microstructural examination

Tensile testing was conducted in accordance with ASTM D3822. The electrical measurements, piezoresistance measurements, Raman spectroscopy, and microstructural examination were conducted in accordance with practices gleaned from other works in general materials science and CNT characterization literature [9] [10] [11]. The intensity of the ultraviolet light exposure was compared with space-based exposure with NASA design documentation [12]. The atomic oxygen exposure was contracted to an outside research facility which has been validated by comparison with space exposed specimens.

Assumptions/Limitations

Simulated space exposures are conducted under much higher intensities of light and fluxes of atomic oxygen than are present in the space environment. It is assumed in the researched conducted herein that the effects caused by higher intensities scale linearly

with time. There was not any information of which the author was aware at the time of this research to doubt this assumption.

It is assumed that the results presented herein are representative of acid-spun CNT fibers and yarn under consideration.

Implications

The results obtained in this research are intended to inform spacecraft design engineers on the mechanical and failure behavior of CNT fibers as well as the effect of the space environment on their mechanical and electrical properties. The single fiber tensile testing with fibers of different gage lengths provides insight on the role of defects in the mechanical properties of CNT fibers. The observed relationship between tensile strength and gage length can be used to predict the tensile strength and its variability at smaller gage lengths relevant to loading scales in composite structures. The variant strain rate testing and static loading testing examine the impact of the fiber microstructure on the relationship between the fiber tensile strength and the rate of mechanical loading. This relationship determines how CNT fibers will behave under different load profiles which is useful for the effective design of composite structures which incorporate CNT fibers. Finally, the results of the space environment testing will inform spacecraft design engineers on the suitability of CNT fibers in the space environment and how CNT fibers should be protected from exposure if incorporated into spacecraft structures.

Organization of Dissertation

The first chapter provides the motivation for the research, the problem statement, a description of the material studied, and an overview of the methodology used to

investigate the problem. The second chapter explains what CNTs are, how CNTs are formed into fibers, and the material properties of CNT fibers. The third chapter outlines the methodology used in this research. The fourth chapter discusses the analysis and results. Concluding remarks are offered in the fifth chapter.

II. Literature Review

Chapter Overview

The purpose of this chapter is to explain what CNTs are, how they are formed into macroscopic fibers, and the mechanical and electrical behavior of CNT fibers. First, a basic description is provided of the structure of CNTs. Next, an overview of methods to create CNT fibers, which is referred to as CNT fiber synthesis, is presented. Then the mechanical behavior of CNT fibers is reviewed followed by statistical methodologies which have been used in the study of the tensile strength of polymer fibers. Next, a brief description is given of the electrical and electromechanical behavior of CNT fibers. Finally, a review is given of the space environment and past research which has investigated impacts of the space environment on CNT fibers.

Carbon Nanotubes

Carbon can form many different allotropes or bonding structures. The fullerene family is an allotrope of carbon, when carbon takes on the shape of a sphere, tube or ellipsoid. CNTs are members of the fullerene family. CNTs are tubes of carbon covalently bonded in a hexagonal lattice. The tubes are essentially rolled-up graphene sheets. CNTs have been synthesized in both single wall or multi-wall forms. Single wall tubes are hollow inside and only a few nanometers in diameter [13]. Multi-wall carbon nanotubes (MWNT) are concentrically nested single wall tubes of different diameters. MWNTs were the first CNTs synthesized. Sumio Iijima discovered CNTs when he observed MWNTs had grown on the cathode of an arc-evaporation reactor intended for the synthesis of other fullerenes [14]. His discovery initiated great public interest in these

new nanotubes because of their unique tube-like structure and their potential applications as electrical and structural materials.

CNTs owe their exceptional mechanical and electrical properties to the strong covalent carbon-carbon bonds. The properties of individual nanotubes depend on the orientation of the bonding in the cylinder relative to longitudinal axis of the fiber. The bonding orientation determines what is known as the chirality of the nanotube. These chiralities are referred to as either zigzag, armchair, or chiral. These terms correspond to the appearance of the bond pattern of the carbon traced normal to the nanotube longitudinal axis. Figure 1 provides a simple schematic of the bond appearance corresponding to each chirality. All armchair CNTs are metallic in nature, while zigzag and chiral CNTs are either metallic or semiconducting depending on the diameter of the nanotube and bonding orientation [13]. Roughly one third of the non-armchair chiralities have metallic character. Synthesis methods generally create a third of each chirality.

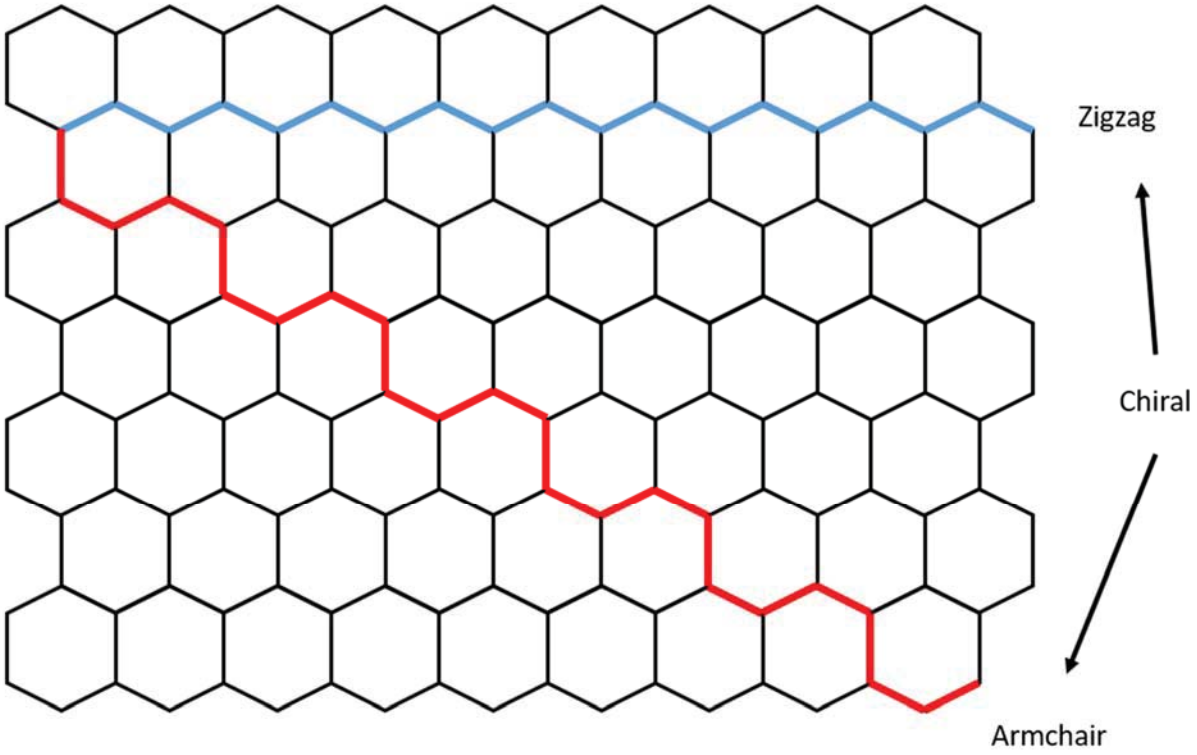

Figure 1: Appearance of CNT bonding orientations based on diagrams in [13]

CNT Fiber Synthesis

There are two routes to assemble CNTs into macroscale fibers, solid-state spinning and wet-spinning. Solid-state spinning combines the nanotube and fiber synthesis into a single continuous process; whereas wet-spinning only involves synthesis of the fiber. The majority of mechanical, electrical and space effects characterization work in the past was accomplished with solid-state spun fibers. The CNT fibers studied in this research are wet-spun CNT fibers. Discussion of the two spinning methods is provided to give perspective on the impacts of fiber synthesis to fiber properties.

The wet-spinning process was the first developed process for creating a fiber from CNTs. The process is very similar to those processes used to synthesize polymeric fibers,

like Kelvar. Wet-spinning begins by dispersing bulk CNTs into a solution. Vigolo, *et al.* [15] used sonication to disperse single-walled CNTs (SWNT) into an aqueous solution of sodium dodecyl sulfate, which is adsorbed by the CNTs to prevent rebundling. The use of sonication to separate CNTs is not ideal because it can cause damage to the CNTs which degrades the performance of the final fiber. The sodium dodecyl sulfate solution prevents re-bundling by electrostatic repulsion. The dispersed CNT solution, called the dope, is extruded through a spinneret and through a coagulant liquid, such as water or acetone. The coagulant encourages CNT alignment and densification of the CNTs in the fiber morphology by surface tension. After passing through the coagulant, the fiber is collected onto a winding drum. Vigolo, *et al.* [15] spun their fiber into a poly(vinyl alcohol) matrix to help hold the fiber structure together. The weak fiber exhibited a strength of only 150 MPa and an elastic modulus of 15 GPa [15].

The wet-spinning method made a huge leap forward when Ramesh, *et al*. [16] discovered that SWNTs would spontaneously dissolve when placed in superacids, acids with acidity greater than 100% sulfuric acid. This discovery eliminated the time consuming and CNT damaging sonication process used by Vigolo, *et al.*. The use of superacid dissolution demonstrated that CNT fibers could potentially be made by an industrially viable spinning process. Additionally, dissolving SWNTs into superacids does not cause damage to the CNTs. As the weight percentage of CNTs in a superacid solution is increased, an aligned crystalline phase will form. Ericson, *et al*. [17] demonstrated that the aligned crystalline phase solution could be extruded through a spinneret to form a highly-aligned, pure fiber. The mechanical and electrical properties of Ericon's fibers were poor but the new process enabled future work to harness the

excellent properties of CNTs. Ten years later, Behabtu, *et al*. [18] made further improvements to Ericson's spinning method by using longer SWNTs (5 μm vs. < 1 μm) along with a better superacid solvent, chlorosulfonic acid (CSA), to achieve much stronger and more conductive pure CNT fibers. These fibers exhibited a tensile strength of 1.0 GPa and an electrical conductivity of 2.9 MS/m. The tensile strength is on the same order of magnitude as high-strength fibers used in composites, while the electrical conductivity is an order of magnitude less than copper.

As more uniform supplies of long, high quality CNTs become available commercially, the wet-spinning process is predicted to produce fibers with tensile strengths rivaling the strongest carbon fibers and electrical conductivity rivaling that of copper [1].

Two distinct solid-state spinning processes were invented shortly after the invention of Vigolo's wet-spinning method. The solid-state process is so called because it directly spins nanotubes into a fiber without the aid of a solution pre-cursor. Zhu, *et al*. [19] synthesized the first solid-state fiber. CNTs had self-assembled into long fibers (several centimeters) inside their CVD reactor, the synthesis was assisted by the vertical orientation and gas flow inside their reactor. Li, *et al*. [20] directly harnessed the mechanism that created Zhu's fiber and spun long fibers directly from a CVD reactor. This process is known as the floating catalyst method due to the utilization of metal nanoparticles which are injected into a reactor as opposed to simply serving as CNT growth sites on a fixed surface. As hydrocarbon vapor is catalyzed in the presence of metal nanoparticles in the CVD reactor, the disassociated carbon grows on the metal nanoparticles and forms a cloud of CNTs or aerogel. Li, *et al*. [20] found that the aerogel

could be directly drawn from the reactor and wound onto a winding drum to form ribbons or fibers depending on the type of winding process. This spinning process has been modified and improved upon to form strong, conductive CNT fibers.

The same year as Zhu's discovery of a self-assembled fiber, Jiang, *et al*. [21] demonstrated that a CNT fiber could be made by drawing fibers from a vertically grown array or forest of CNTs. An array of CNTs is a solid mass of CNTs aligned in one direction. As CNTs are pulled from the array, nearby CNTs are recruited into the form of a fiber and self-assemble into a macroscopic fiber by way of weak van der Waals forces between the nanotubes. Zhang, *et al*. [22] made a significant improvement to Jiang's process by twisting the fiber during the drawing process. The drawing and twisting process works by the same principle as textile thread spinning (cotton, wool, etc.) which has been in use for many thousands of years. The CNTs are bound to one another by the spinning process. The fibers in Zhang's work were found to have tensile strengths greater than 460 MPa, and the strength was not degraded by tying a knot into the spun CNT fiber. Extreme heating at 450 deg C or exposure to cryogenic temperatures did not degrade the mechanical performance of the fiber. While fibers with impressive properties have been created by the array spinning process, the process is not as scalable as the floating catalyst method. The array-spinning method is a useful method for researchers to create fibers for small-scale, inexpensive research.

The various fiber synthesis methods discussed have undergone significant refinement which have resulted in stronger and more conductive fibers. Processes which improve alignment and density of the fibers have produced the best results in both synthesis methods. Increasing alignment and increasing density reduces the room for

voids between CNTs which allows for stronger bonds between nanotubes, which increases the overall fiber strength [23]. The following sections will discuss the mechanical and electrical behavior of fibers as well as statistical methods used to analyze the strength of similarly structured materials.

Mechanical Behavior of CNTs and CNT Fibers

Theoretical studies into the mechanical properties of CNTs predict that the elastic modulus and tensile strength of perfect CNTs, both single- and multi-wall, will be approximately 1 TPa and 100 GPa, respectively. Researchers were able to experimentally validate the 1 TPa elastic modulus prediction value early after the discovery of CNTs; however, measured tensile strengths fell short of the predictions. More recently, researchers have been able to experimentally verify the maximum 100 GPa tensile strengths of both SWNTs [24] and MWNTs [25] by improving the supporting substrate-CNT interface and eliminating post-treatments to the CNTs which induce defects into the tubes.

Despite these impressive mechanical characteristics, researchers have been unable to translate the impressive strength and stiffness of individual CNTs to macroscale structures such as fibers or sheets. Koziol, *et al*. [26] synthesized the strongest CNT fiber with a tensile strength of 9 GPa. Their strongest fiber had a gage length, the distance between the grips which hold a specimen, of only 1 millimeter. This distance was likely spanned by long CNTs, meaning the test was . For longer gage lengths, CNT fiber strengths lie in the range of 1-2 GPa [18] [26] [27]. Many fibers reported in literature exhibit strengths far less than these exceptional values reported above. It is possible that

CNT based fibers have reached their maximum potential in this 1-2 GPa strength range, but more recent work suggests that improvements in CNT synthesis may lead to fibers as strong as high-strength carbon fibers [1].

Several researchers have attempted to identify the limiting factors in fiber strength. The key contributing factors identified are: the mechanical properties of constituent CNTs, the intermolecular forces between CNTs, and the load transmission mechanisms as the fiber morphology changes during load application [28].

The first factor, the strength of constituent nanotubes, has been investigated utilizing molecular dynamics simulations and microscopy. Zhu, *et al*. [29] used computational modeling techniques to examine the effect of topological tube defects and found that such defects may reduce tube strength by an order of magnitude. Ouyang, *et al*. [30] examined SWNTs by scanning tunneling microscopy and observed a relatively high occurrence of topological defects, approximately 10% of SWNTs studied, on tubes grown by the laser-vaporization method, which is known for producing high-quality nanotubes. If constituent CNTs alone governed fiber strength, Zhu, *et al*. [29] and Ouyang, *et al*. [30] suggest fibers should be exhibiting strengths on the order of 10 GPa, which is like that found by Koziol, *et al.* [26] when examining extremely long CNTs.

The second factor, intermolecular forces, not only affects the strength of CNT fibers but also how they fail. The various spinning processes for creating CNT fibers rely upon van der Waals forces between CNTs to hold the CNTs in the fiber together. These bonds are relatively weak in comparison to the strong covalent bonds between carbon atoms within a tube. Yakobson, *et al*. [31] predicted that assemblies of tubes would fail at strengths far less than the strength of the individual tubes. Yu, *et al*. [32] observed only

the outermost shell of MWNTs under tension would carry the load and the remaining shells would slide past each other by a sword-in-sheath type failure mechanism, indicating weak load transfer between shells.

Deng, *et al*. [33] observed through tensile testing with in-situ Raman spectroscopy that interfacial slippage between the constituent materials limits the tensile strength of CNT fibers. Rao, *et al*. [28] used finite element modeling along with in-situ small-angle X-ray scattering analysis to study the mechanical behavior of CNT fibers. Their testing revealed large hysteresis from successive loading cycles, indicating a permanent change in the internal morphology of the fiber. This change is attributed to the progressive slipping of constituent CNTs and distortion of the fiber microstructure until catastrophic failure.

Rao, *et al*. [28] also analyzed the effect of misalignment within the as-made fiber and its effect on the progression of failure within the fiber under tensile load. They found as the fiber is progressively loaded, the weakest bonds break and segments of CNTs that had previously been carrying load relax, and so other CNTs or bundles of CNTs must take on the load they were carrying. There is a high strain energy penalty for reformation of contacts once the initial morphology has been disrupted. Therefore, as the loading progresses, fewer of the initial contacts reform and the total number of contacts within the fiber drops. This initial phase of weak bond breakage progresses until maximum alignment is reached and the onset of stick-slip occurs. Stick-slip is characterized by the failure and reattachment of contacts within the fiber during incremental steps of strain [28]. Above a threshold, the stress redistribution is too great, which prevents reattachment of contacts and causes the fiber to fail.

Koziol, *et al.* [26] tested a variety of different gage length fibers to study the effects of random defects on fiber strength. They observed a bimodal distribution of fiber strengths on short fibers (1-2 mm) but not with longer 20 mm fibers, which Koziol, *et al.* attributed to strength limiting defects randomly distributed throughout their fibers on length scales of millimeters. Equally likely, the bimodal distribution arose because of the random distribution of CNT lengths present in their fibers. A few tested fibers likely had very long CNTs spanning the gage length which resulted in the higher strength peak of the probability density function, while most tested fibers did not have long CNTs spanning the gage length, resulting in the much lower strength peak. Their fiber tensile test results showed a large degree of dispersion. The tensile strengths of their fibers exhibited a standard deviation of 15.7% of the mean. The ratio of the standard deviation and the mean is called the coefficient of variation (CV) and is often expressed in percentage form. It expresses the normalized degree of dispersion of a property. In contrast, the tensile strengths of metals exhibit CVs of about 5%.

The large degree of variation observed in the tensile strength of CNT fibers warrants the use of statistical approaches to better model their behavior. The next section introduces statistical approaches which have been used in the study of the tensile strength of other fibers.

Statistical Approaches to the Study of Fibrous Materials

Statistical variability in the tensile strength of fibrous materials is not unique to the fibers synthesized by Koziol, *et al*. [26] or CNT fibers in general [23]. Brittle fibrous materials exhibit a large degree of statistical variability in their mechanical properties,

which is due to variability in size, shape, orientation of fibers as well as the presence of micro- and macroscopic defects. The foundation of these approaches is the weakest-link theory which was first applied to the study of textile fibers by Fredrick Peirce [34]. More generally, Weibull [35] stressed the need for statistical approaches to analyze the strength of materials based upon variability and weakest-link effects and the inadequacy of contemporary theories of the strength of materials to describe their behavior. Coleman [36] built upon reaction rate theory developed by Tobolsky and Eyring [37] to show that weakest-link relationships arise from the behavior of molecular bonds under applied stress. His model can describe the behavior of fibrous materials under a variety of loading histories whereas weakest-link theory is limited to viewing each moment of loading as non-interacting statistically independent events. The weakest-link theory will be summarized first with a following discussion of Coleman's model.

Peirce [34] proposed that fibers could be viewed as a chain of elements with randomly distributed strengths and that the strength of the fiber is determined by its weakest element or link. The probability of failure of a chain of elements is dependent upon the probability of failure of its constituent elements. The probability of survival of a given fiber element when subjected to stress, σ_i, is assumed to be a statistically independent event with a certain probability, $F(\sigma_i)$. The probability of failure for each element is $1 - F(\sigma_i)$ and the probability of failure of a fiber composed of n statistically identical, independent elements is $1 - F_n(\sigma_i)$ which gives rise to the weakest-link equation

$$1 - F_n(\sigma_i) = [1 - F(\sigma_i)]^n. \tag{2.1}$$

The weakest-link relationship combined with an expression for a chosen parent distribution, $F(\sigma_i)$, allows for the calculation of the probability distribution of fibers of length $L = nL_0$, where L_0 is the element length.

The Weibull distribution has become the preferred choice to describe the variability in strength of many brittle fibers, including: aramid [38], carbon [39] [40], ceramic [41] [42], and CNT [23] [43] fibers. Researchers [44] have questioned the validity of blindly using the Weibull distribution to model the statistical variability of the strength of fibrous materials. Smith and Phoenix [45] showed that the Gumbel distribution may be a more suitable distribution for the strength of fiber bundles. Amaniampong and Burgoyne [44] experimentally observed that the best parametric distribution was dependent on the material tested. They found that the Gumbel model was more appropriate for aramid yarns, while the Weibull model was more appropriate for polyester yarns. Determining the best parametric distribution for a set of strength data is difficult. Amaniampong and Burgoyne [44] utilized the Kolmogorov-Smirnov (KS) test as a model selection tool. They determined parameter estimates for a variety of 2-parameter distributions and judged whether the resulting distributions passed the test. The KS test is a useful tool; however, when the parameters for many 2-parameter distributions are estimated by maximum likelihood methods, several statistical distributions will pass the KS test for a set of strength data. The Akaike Information Criterion is another statistical test which is more powerful than the KS test for model selection. Its use will be discussed in Chapter III. Arguments for selecting the appropriate distribution will be considered later; however, because of the wide use of the Weibull distribution in past fiber research, its use will be discussed further.

Wagner, *et al*. [46] used the maximum likelihood method to determine Weibull parameters for fibers of different gage lengths. These parameters were compared via the relationship of Equation 2.1 and the weakest-link relationship failed to calculate the correct statistical distribution at other gage lengths. These observations cast doubt on the applicability of the weakest-link equation for the strength of some fibers. The fiber synthesis method of these fibers was relatively mature, which may have eliminated rare occurrences of severe fiber defects which may lead to the appearance of the weakest-link effect in natural fibers and synthetic fibers with immature synthesis processes. This hypothesis suggests that with maturity in the fiber synthesis process, weakest-link scaling of strength should be expected to weaken or disappear entirely as large, critical defects are eliminated by manufacturing controls.

The following discussion will develop the justification for the Weibull distribution as the appropriate distribution to describe the tensile strength of fibers and how the Weibull distribution relates to weakest-link theory. The weakest-link relationship is concerned with the probability of failure of very small elements. If the number of elements in a fiber is very large, then extreme value theory [47] provides only three feasible limit distributions for the minima of independent, identically distributed (iid) random variables. The three limit distributions for minima are the Frechet, Weibull and Gumbel distributions. Of these, only the Weibull obeys physically sensible boundary conditions, namely at zero stress, the fiber will not fail, $F(0) = 0$, and as stress grows very large, the probability of failure becomes certain, $F(\infty) = 1$.

These physical considerations along with the model's mathematical simplicity were motivating factors for Weibull's formulation of the model [35]. Coleman [48] has

also used extreme value theory to argue that the Weibull distribution is the appropriate distribution for modeling the strength of brittle fibers. So, there is reasonable justification for selection of the Weibull distribution to model the statistical variability of the strength of fibers.

The cumulative distribution function (CDF) of a variable, σ, represents the probability that the variable takes on values less than some value. The CDF of the two-parameter Weibull distribution, in terms of tensile stress, σ, is represented by the equation

$$F(\sigma) = 1 - \exp\left[-\left(\frac{\sigma}{\alpha}\right)^{\beta}\right] \tag{2.2}$$

where α and β are the scale and shape parameters, respectively. The CDF of the Weibull distribution represents the probability that a fiber will fail at a stress less than some stress value, σ. The scale parameter is like the Gaussian mean, and the shape parameter, a unitless quantity, is inversely related to the dispersion or variation of the data. If the Weibull distribution is the CDF for the strength of the elements in Equation 2.1, it becomes the weakest-link Weibull equation

$$F(\sigma_i, L) = 1 - \exp\left[-\left(\frac{\sigma_i}{\alpha}\right)^{\beta}\right]^{n} = 1 - \exp\left[-n\left(\frac{\sigma_i}{\alpha}\right)^{\beta}\right]. \tag{2.3}$$

Additionally, when the location and severity of flaws are taken to occur as a compound Poisson process, all real, nonnegative values are admissible for n [49]. Watson and Smith [38] modified Equation 2.3 by making the number of links, n, equal to the length of each tested specimen, L, and modifying the scale parameter, α, by the equation

$$\alpha_L = L^{-\frac{1}{\beta}}\alpha, \tag{2.4}$$

which results in the expression of the weakest link Weibull solution used in the gage length effects analysis in this research

$$F(\sigma; L) = 1 - \exp\left[\left(\frac{\sigma}{\alpha_L}\right)^{\beta}\right]. \tag{2.5}$$

While the weakest-link theory is a useful tool for characterizing the statistical strength distributions of fibrous materials, its major shortcoming is its inability to account for differences in loading history. The weakest-link theory only accounts for tensile strength of fibers under a linearly increasing stress. Coleman [36] developed a theory which could relate the strength of fibers when subjected to a linearly increasing stress history, static loading, and dynamic or fatigue loading. Under certain molecular breakdown assumptions, Coleman's model yields the Weibull distribution for tensile strength experiments while also providing kinetic interpretations for the model parameters. These interpretations explain how temperature and rate of loading affect the Weibull parameters. The full development of Coleman's model will not be repeated here but the useful relationships between the parameters and loading type will be presented. Coleman's model shows that the Weibull distribution arises for static loading with respect to time to failure in the form

$$F(t) = 1 - \exp\left[-\left(\frac{t}{r}\right)^{s}\right] \tag{2.6}$$

where s and r are the shape and scale parameters, respectively. Coleman's model relates the shape parameter of a static loading Weibull distribution for time to failure to the distribution for strength by the equation

$$\beta = s(\rho + 1) \tag{2.7}$$

where ρ is a positive constant. The scale parameter, α, in Equation 2.5 is related to the shape parameters by the relationship

$$\alpha = \left[R(\rho + 1)\left(\gamma^{-1}\mu^{-\frac{1}{s}}\right)\right]^{\frac{1}{\rho+1}} \tag{2.8}$$

where R is the rate of loading in units of stress per time, and γ and μ are positive constants. This relationship shows that the Weibull scale parameter, α, should be linearly related to the rate of loading in log-log coordinates with slope $1/(\rho + 1)$. The scale parameter, α, is closely related to the sample mean and so the importance of ρ is apparent because it represents the sensitivity of tensile strength to loading rate. Large values of ρ represent low sensitivity to loading rate, and small values indicate high sensitivity. Coleman's model relates ρ to the activation energy, so the physical significance of ρ is that it describes the strength of bonds being broken at different loading rates. Low values of ρ, signify that weak bonds are dominating the mechanical behavior, where high values of ρ indicate that stronger intermolecular bonds, such as covalent bonds, are dominating the mechanical behavior.

The weakest-link model is unable to relate loading history to statistical model parameters, but the kinetic Coleman framework can provide some physical interpretation of the implications of different loading types. The weakest-link model will be used to analyze the flaw population interactions with tensile strength, while the Coleman model will be used to assess physical implications of different loading histories on CNT fibers.

Electrical Behavior of CNTs and CNT fibers

In addition to the mechanical behavior of CNTs and CNT fibers, their electrical properties and the effects of the space environment on their electrical properties is also of interest. This section gives a brief overview of the electrical conductivity of CNTs and CNT fibers and the contributing factors to this property.

CNT fibers have also generated significant interest in their ability to perform as electrical conductors. Experiments with individual CNTs have found electrical conductivity on the order of 10^7 S/m, the same as highly conductive metals [50]. Wei, *et al*. [51] observed individual CNTs could withstand extremely high current densities for hundreds of hours. Furthermore, there was no observable change in the resistance of the CNTs or their morphology during the extended exposure. These impressive properties have not been achieved in macroscale fibers. The most electrically conductive CNT fibers had an electrical conductivity of 8.5 MS/m, which are 85% less than the electrical conductivity of copper [1] [52].

The primary source of resistance in CNT networks is the resistance to charge transfer between nanotubes, which is also called charge “hopping” resistance [53]. Several factors influence charge transfer resistance; the length of nanotubes, defects on nanotubes, alignment of the network, and packing density. The properties of the constituent nanotubes are important because longer, defect free nanotubes will transfer charge over a longer distance before needing to pass its charge to nearby nanotubes, thereby reducing the resistance of the network. Achieving exceptional electrical conductivity in these materials will involve improving the quality and length of the constituent nanotubes as well as the alignment and packing density of the network.

The electrical behavior of CNTs and CNT fibers can be influenced by the application of mechanical strain. This strain-affected electrical behavior is referred to as the electromechanical behavior of CNTs. The electromechanical behavior may also shed light upon microstructural changes to the CNT fibers and so relevant electromechanical CNT research is reviewed in the following section.

Electromechanical Behavior of CNTs

The electromechanical behavior of CNTs has been well documented through investigations into the piezoresistive effect in CNT materials [10]. Piezoresistance is a unique property of materials that relates a change in electrical resistance to an applied mechanical strain. This effect was first discovered by Lord Kelvin in 1856 and its principle is utilized for mechanical strain gauges [54]. Bridgman [55] took the first piezoresistance measurements in 1925 with several types of metals and a variety of researchers have made measurements and characterized the effect in other materials. The primary measure of piezoresistance is the unitless quantity, gauge factor (GF). It is defined by the following equation

$$GF = \left(\Delta R/R_0\right)/\epsilon \tag{2.9}$$

where ΔR is the change in resistance of the material between the strained and unstrained state, $R_0$is the resistance of the material in its unstrained state, and ε is the applied strain.

It is expected that the electrical conductivity of a material would change due to a change in cross-sectional geometry with applied strain due to the Poisson effect. Piezoresistance is characterized by a larger resistance change due to applied strain than

would be expected due to purely geometric changes. If geometric changes were the sole factor in piezoresistance, one would expect GFs to be governed by the equation

$$GF = 1 + 2v \tag{2.10}$$

where v is the Poisson's ratio of the material. Examining nickel, with a Poisson's ratio of 0.31, the preceding equation would predict a GF of 1.62, whereas experimentally nickel has been found to have a GF of -10 [54]. Higher magnitude GFs indicate better sensitivity to strain, and the ability to perform as the basis for a strain gauge. Common commercial metal-wire and tape type strain gauges have GFs on the order of 0.5-5 [54].

Two factors contribute to the observed GF in CNT fibers. First, the individual CNTs exhibit the piezoresistive effect when strained, which is influenced by their chirality [56]. Secondly, as the network is deformed, the rearrangement of CNTs will change the alignment and packing density of the network and thus change the network resistance. Zhao, *et al*. [53] made many GF measurements on CNT fibers, observing GFs of only 0.5, which is several orders of magnitude less than the GFs observed for individual CNTs [56]. The primary limiting factor in Zhou's fibers may be the high charge transfer resistance between CNTs, which masks the strain response of the individual CNTs.

Space Environmental Effects on CNT Materials

The space environment affecting vehicles orbiting the Earth is split into three orbital regimes: Low Earth Orbit (LEO), Medium Earth Orbit (MEO), and Geosynchronous (including Geostationary) Orbit (GEO). LEO is defined as orbits with altitudes of 200-1000 km above Earth's surface. MEO is defined by orbits higher than

LEO and lower than GEO. GEO (Geostationary) is defined as orbits with altitudes of 36,000 km situated above the Earth's equator, which allow spacecraft in that orbit to stay in a relatively fixed position with respect to a point on the Earth's equator. Man-made satellites are operated in each of these orbits, therefore considering the unique environmental effects of each is important to assess the suitability of CNTs as replacement materials in spacecraft.

Environmental effects common to all orbits are: vacuum, ultraviolet (UV) radiation from the Sun, ionizing particle radiation, impacts from micrometeoroids and debris, and thermal cycling (extreme limits of approximately -175 to 160 deg C) [57]. In GEO, electrostatic discharge is a greater concern than at lower orbits. MEO orbits can experience higher particle radiation levels due to the Van Allen radiation belt which extends from 1,000 to 60,000 km above the earth. External spacecraft surfaces in LEO are also subject to atomic oxygen (AO) exposure due to the disassociation of diatomic oxygen by UV radiation in the upper atmosphere [58].

Solar UV radiation is a larger concern on orbit than terrestrially because the Earth's atmosphere absorbs all UV radiation with wavelengths less than 300 nanometers. Surfaces that are not exposed to direct Sunlight, such as thermal radiators, may still experience some UV exposure due to the Earth's Albedo, which is the Sun's reflected energy (~31%) from the Earth into space [58]. The UV energy experienced in Earth's orbit may be divided into two bands: Near UV, 200-400 nm range; and Vacuum UV, 100-200 nm range. The interactions between insulating materials and CNTs and bare CNTs only exposed to UV light in these wavelengths is not well characterized. Some

testing has been carried out but has utilized a mixed source of UV and AO. No research has been published on the effects of UV alone on CNTs.

Vacuum pressure will not affect CNTs aside from potential out-gassing of trapped atoms and molecules present from the synthesis or post-processing treatments. Satellites and constituent materials bound for space are subjected to out-gassing processes which remove such contaminants before reaching the space environment, therefore the study of effects of vacuum pressure is not as valuable.

Conducting material exposure experiments in the space environment and retrieving them for analysis is the most valuable but also the most expensive. So terrestrially conducted exposures in simulated space environments are conducted in lieu of direct environment exposures.

Several bare CNT fibers, synthesized by the dry-spinning method, were attached to the exterior of the International Space Station for 2 years and recovered for analysis [11]. It is the only experiment to date to expose CNT fibers in the space environment and recover them for lab analysis. Separate fibers were placed on the ram and wake sides of the International Space Station. The ram refers to the side of the spacecraft facing the direction of travel, while wake side faces opposite to the direction of travel.

Ram-exposed fibers showed a 25% decrease in tensile strength, while wake-exposed fibers showed very little change in tensile strength; however, the strain at failure was significantly reduced for both the ram and wake-exposed specimens compared to the unexposed control specimens. Hopkins, *et al.* [11] attributed the decrease in tensile strength to the oxidation of the outer layer of the fiber from AO exposure, which may have rendered the outer CNTs in the fiber unable to contribute equally in carrying the

applied tensile load. The reduction in strain at failure was thought to be caused by radiation-induced crosslinking of constituent CNTs in the fiber and an accompanying embrittlement. Both the ram and wake-exposed specimens showed similar increases of resistivity of 26.1% and 28.5%, respectively.

Hopkins, *et al.* [11] show that it is important to consider the effect of the space environment on CNT materials; however, CNT materials utilized as conductors in the space environment will likely be electrically insulated and shielded by protective space-hardened coatings. CNT fibers may find some application where it is desirable to leave them exposed, in which case it is useful to quantify the effects of space exposure on their performance. CNTs may be left exposed when incorporated into an antenna, sensor, or mechanical tether.

Misak, *et al.* [59] [60] have simulated different space environmental effects on the performance of CNT fibers. Their work focused primarily on thermal cycling of uninsulated CNT fibers in air; however, thermal cycling in air may not be representative of thermal cycling in vacuum. Carbon oxidizes when exposed to air and high temperatures, and changes in their results may be due to the presence of diatomic oxygen, which is not representative of vacuum exposed or insulated fibers. Their testing utilized two temperature profiles, cycling between two extremes for 5,000 cycles each. The first test cycled between -50 and 70 deg C and the second cycled between -70 and 150 deg C. Only a 2.5% decrease in electrical conductivity was observed for the first temperature regime and an 18% decrease was observed with the second temperature regime. 5,000 cycles were chosen to attempt to simulate approximately 300 days on board the International Space Station. The same number of thermal cycles on board a satellite in

MEO or GEO, with a single thermal cycle per day, would represent 27 years of service life.

Misak, *et al*.'s [59] [60] studies into the effects of AO exposure showed little to no change in the properties on the materials after exposure, which does not agree with the Hopkins' [11] findings. There may be shortcomings to the experimental set-up of Misak and efforts should be undertaken to make improvements to it to provide accurate terrestrial CNT characterization in the desired environment. The materials in the works of both Misak and Hopkins were exposed to UV and AO simultaneously due to the nature of the environment and the AO-exposure apparatus. Further testing was conducted in this research to isolate the effects of UV radiation and AO exposure sources to identify the largest contributor to the degradation observed in Hopkins' work.

Summary

The current state of the science of CNT fiber synthesis, as well as the understanding of their mechanical and electrical behavior, has been laid out. Effects of the space environment on their behavior was also discussed. This research will expand upon the limited research on statistical variability, strain at moderate to low rates, gage length effects, and effects of the space environment. Aerospace applications are a promising field for utilization of CNT fibers due to their exceptional weight normalized properties (specific weight and electrical conductivity), which warrants further understanding of their behavior under mechanical loading and their response to the space environment.

III. Methodology

Chapter Overview

The purpose of this chapter is to discuss the statistical methodology utilized in analysis of the experimental results obtained in this research as well as the experimental set-up used to collect measurements and images.

Statistical Methodology

The mechanical and electrical properties of CNT fibers vary significantly from fiber to fiber and along individual fibers. Statistical methods are necessary to characterize the degree of variation and how various samples differ from each other. These statistical methods are used throughout this research. In engineering practice, parametric distributions are found to describe sample material properties well with strong statistical evidence.

The Normal or Gaussian distribution is the most ubiquitous parametric distribution in science with many phenomena following the distribution. The Gaussian distribution is a two-parameter distribution, meaning only two values are required to describe the location and shape of the distribution. The probability density of the Gaussian distribution is represented by a bell-shape curve. The mean indicates the location of the center of the curve on the abscissa. The mean of the distribution, represented by the Greek letter μ, is calculated by summing all observed values of some measured property, x_i, and dividing by the total number of observations, N. The variance, represented by the Greek letter σ squared, describes the shape of the distribution. A small

variance will lead to a narrow distribution and a large variance leads to a wide distribution. The variance is calculated by the following equation

$$\sigma^2 = \frac{1}{N-1}\sum_{i=1}^{N}|x_i - \mu|\,. \tag{3.1}$$

The Gaussian distribution reasonably fits the strength data collected in this research with good statistical confidence. This behavior is likely a consequence of the central limit theorem given that CNT fiber fabrication is a combination of processes with inherent variability [61]. The following is a non-exhaustive list of factors with variability in the fabrication of CNT fibers: CNT length, diameter, defect density, and purity, temperature of the CNT solution prior to spinning, diameter of the extrusion spinneret, speed of fiber extrusion, and post-processing techniques. Given this Gaussian behavior, the two Gaussian parameters (mean and variance) are calculated for all properties to provide an initial assessment of the measured properties and their variability. The computer program, MATLAB, contains functions to calculate these parameters for a finite set of observations, which were used for all measurement sets conducted herein.

There are other two-parameter distributions used in engineering practice to describe the variation of material properties. The Gaussian distribution is symmetric about its mean, other distributions are more heavily weighted toward a single side or tail of the distribution. The Weibull distribution more accurately represents data which are heavily skewed towards a single side of the distribution, but the parameters of the Weibull distribution are less easily determined. The Maximum Likelihood (ML) method is a tool to calculate the parameters of statistical distributions. The values obtained by the ML method are called the Maximum Likelihood Estimators (MLE) of the statistical

distribution and are typically represented with a tilde over the regular symbols used for the parameters. The tilde indicates these values are the "most likely" values of the parameters for the statistical distribution. MATLAB also contains functions to calculate the MLEs for an array of values. The ML method is demonstrated below for the Weibull distribution to demonstrate the underlying methodology. The method allows the calculation of standard errors as well as enables formal hypothesis testing [38].

The MLEs were calculated for the Weibull distribution using the solution presented in the following section and compared to the results obtained from the *mle* function. Both routes led to the same values for all data sets obtained in this research.

The *mle* function in MATLAB does not work with modifications to statistical distributions like the weakest-link modification introduced in Chapter II.

It is necessary to evaluate whether a statistical distribution provides a good fit of a set of experimental data. The KS test, discussed in Chapter II, is a nonparametric test to evaluate goodness of fit [62]. The test is based upon the maximum difference between an empirical and speculated cumulative distribution. The test was used to evaluate whether a variety of common statistical distributions provided good fits of the data.

Statistical methods also provide tests to compare distributions obtained from empirical data to test whether they differ significantly. The two-tailed t-test compares two sets of data to test whether they are independent random samples from normal distributions with equal means and equal but unknown variances. The one shortfall of the test is that it assumes normality in the underlying distributions of the sampled data. This may not be true and could lead to incorrect results. The previously mentioned KS test may be used to compare two empirical cumulative distributions rather than an empirical

and speculated cumulative distribution using the same methodology. This test does not assume normality in the underlying distributions and is therefore more flexible. The KS test is also used for comparison of different data sets to examine whether they arise from the same underlying continuous distribution.

Finally, the previously mentioned tests do not provide a metric of comparison of goodness of fit of different distributions to the same set of data. The Akaike Information Criterion (AIC) test can make comparisons of goodness of fit to choose a best fit distribution [63]. The AIC test is chosen because of its ease-of-use and its compatibility with the ML method.

Statistical Distribution Parameter Estimation

The parameters of the Weibull distribution and the weakest-link Weibull distribution were determined by maximum likelihood estimation. The CDF of the Weibull distribution for the tensile strength of the fibers, Equation 2.2, is repeated here for convenience

$$F(\sigma; L) = 1 - \exp\left[\left(\frac{\sigma}{\alpha}\right)^{\beta}\right] \tag{3.2}$$

and the weakest-link modification to the CDF of the Weibull distribution, Equation 2.5, is repeated here as well

$$F(\sigma; L) = 1 - \exp\left[\left(\frac{\sigma}{\alpha_L}\right)^{\beta}\right] \tag{3.3}$$

with the modification of Equation 2.4 repeated here also

$$\alpha_L = L^{-\frac{1}{\beta}}\alpha. \tag{3.4}$$

Presented here is the ML method for the two-parameter Weibull distribution. The ML method begins by calculating the likelihood function from the probability density function (PDF) of a statistical distribution. The PDF, $f(\sigma)$, is related to the CDF, $F(\sigma)$, of a continuous random variable, σ, by the equation

$$F(\sigma) = \int_{-\infty}^{\sigma} f(u)du\,. \tag{3.5}$$

The integral of the PDF of some random variable in the interval $[a, b]$ yields the probability that the random variable is within the defined interval.

The PDF for the Weibull distribution is defined as:

$$f(\sigma{:}\,\alpha,\beta) = \frac{\beta}{\alpha}\left(\frac{\sigma}{\alpha}\right)^{\beta-1}\exp\left(-\left(\frac{\sigma}{\alpha}\right)^{\beta}\right) \tag{3.6}$$

where σ is a continuous, random variable for the tensile strength of a CNT fiber.

The likelihood function is defined as the product of the PDF, f, for all values of σ

$$L(\alpha,\beta) = \prod_{i=1}^{N} f(\sigma_i{:}\,\alpha,\beta)\,. \tag{3.7}$$

Here, the likelihood function is defined in terms of, σ_i, which is a sample from σ.

To find the maximum likelihood estimators for α and β, minimize the natural logarithm of the likelihood function, Equation 3.3. The result is called the log-likelihood function. The log-likelihood function, $l(\beta,\alpha)$ with rearrangement of terms is

$$l(\alpha,\beta) = \ln\big(L(\alpha,\beta)\big) = N\ln(\beta) - N\beta\ln(\alpha) - \textstyle\sum_{i=1}^{N}\left(\frac{\sigma_i}{\alpha}\right)^{\beta} + (\beta-1)\sum_{i=1}^{N}\ln(\sigma_i). \tag{3.8}$$

Next, solving for the minimum of the log-likelihood function by taking partial derivatives of the log-likelihood function with respect to the statistical parameters, α and β, and setting the derivatives equal to zero yields

$$\frac{\partial l}{\partial \alpha} = -\frac{N\beta}{\alpha} + \beta \sum_{i=1}^{N} \frac{\sigma_i^{\beta}}{\alpha^{\beta+1}} = 0 \tag{3.9}$$

and

$$\frac{\partial l}{\partial \beta} = \frac{N}{\beta} - N \ln(\alpha) - \sum_{i=1}^{N} \ln\left(\frac{\sigma_i}{\alpha}\right) \exp\left(\beta \ln\left(\frac{\sigma_i}{\alpha}\right)\right) + \sum_{i=1}^{N} \ln(\sigma_i) = 0. \tag{3.10}$$

The partial derivative with respect to the scale parameter, α, rearranged gives the solution for the MLE of $\tilde{\alpha}$, which is represented with a tilde to indicate that it is the MLE for α. The solution for the MLE is

$$\tilde{\alpha} = \left(\frac{1}{N} \sum_{i=1}^{N} \sigma_i^{\tilde{\beta}}\right)^{\frac{1}{\tilde{\beta}}}. \tag{3.11}$$

This result can be substituted into the partial derivative of the log-likelihood function with respect to the shape parameter, $\tilde{\beta}$, which yields,

$$\tilde{\beta} = \left[\frac{\sum_{i=1}^{N} \sigma_i^{\tilde{\beta}} \ln(\sigma_i)}{\sum_{i=1}^{N} \sigma_i^{\tilde{\beta}}} - \overline{\ln(\sigma_\iota)}\right]^{-1}. \tag{3.12}$$

Equation 3.12 is only solvable numerically. For the research herein, the Newton Raphson algorithm was chosen to solve for the shape parameter by the following process. An initial guess is made for $\tilde{\beta}$ based upon a common approximation for $\tilde{\beta}$, which is

$$\beta_0 = \frac{1.2}{CV} \tag{3.13}$$

where CV is the previously defined coefficient of variation of the data [64].

The iterative solution by the Newton-Raphson method for $\tilde{\beta}$ is then

$$\beta_{i+1} = \beta_i - \frac{f(\beta_i)}{\frac{df(\beta_i)}{d\beta}}. \tag{3.14}$$

Convergence criteria for the Newton-Raphson iterative method was defined as a change of less than 10^{-3} between iterations. The method converged in less than or equal to 3 iterations for all data sets conducted herein. For completeness, $f(\beta_i)$ and $df(\beta_i)/d\beta$ are

$$f(\beta) = \frac{\sum_{i=1}^{N} \sigma_i^{\beta} \ln(\sigma_i)}{\sum_{i=1}^{N} \sigma_i^{\beta}} - \frac{1}{\beta} - \frac{1}{\mathrm{N}} \sum_{i=1}^{N} \ln(\sigma_i) \tag{3.15}$$

and

$$\frac{\partial f(\beta)}{\partial \beta} = \frac{\sum_{i=1}^{N} \sigma_i^{\beta} \sum_{i=1}^{N} \sigma_i^{\beta} (\ln(\sigma_i))^2 - \sum_{i=1}^{N} \sigma_i^{\beta} \ln(\sigma_i) \sum_{i=1}^{N} \sigma_i^{\beta} \ln(\sigma_i)}{\left(\sum_{i=1}^{N} \sigma_i^{\beta}\right)^2} + \frac{1}{\beta^2}. \tag{3.16}$$

The preceding equations show the solution for the MLEs for the two-parameter Weibull distribution. The MLEs can now be used to calculate the standard error for each parameter estimate. The significance of the standards errors is that they represent an approximated 95% confidence intervals for the parameter estimates by ± 1.96 times the standard errors. The confidence interval represents where the parameters can reasonably be expected to lie [61].

The standard errors for the MLEs are computed by use of the Fisher information matrix [63]. The Fisher information matrix, $I(\alpha, \beta)$ of the two-parameter Weibull distribution, is a symmetrical matrix defined as

$$I(\alpha, \beta) = -\frac{\partial^2}{\partial \alpha \partial \beta} l(\alpha, \beta). \tag{3.17}$$

The Hessian matrix is simply the negative of the Fisher information matrix. The inverse of the Hessian matrix provides an estimate of the covariance matrix of the MLEs.

The square root of the diagonal components of the covariance matrix are the standard errors of the MLEs. The Hessian matrix for the two-parameter Weibull MLEs is:

$$H(\alpha,\beta)=\begin{bmatrix}\dfrac{\partial^2 l(\alpha,\beta)}{\partial\beta^2} & \dfrac{\partial^2 l(\alpha,\beta)}{\partial\beta\partial\alpha}\\ Sym. & \dfrac{\partial^2 l(\alpha,\beta)}{\partial\alpha^2}\end{bmatrix} \tag{3.18}$$

and with the fully developed equations the Hessian matrix yields

$$H(\alpha,\beta)=-\begin{bmatrix}-\dfrac{N}{\beta^2}-\beta\sum_{i=1}^{N}\ln\left(\dfrac{\sigma_i}{\alpha}\right)\exp\left(\beta\ln\left(\dfrac{\sigma_i}{\alpha}\right)\right) & -\dfrac{N}{\alpha}+\sum_{i=1}^{N}\dfrac{\sigma_i^{\beta}}{\alpha^{\beta+1}}(\beta\ln(\sigma_i)-\beta\ln(\alpha)+1)\\ Sym. & \dfrac{N\beta}{\alpha^2}-(\beta^2+1)\sum_{i=1}^{N}\dfrac{\sigma_i^{\beta}}{\alpha^{\beta+2}}\end{bmatrix}. \tag{3.19}$$

The MLEs, $\tilde{\alpha}$ and $\tilde{\beta}$, and strength data, σ_i, are plugged into the negative Hessian matrix, the matrix is inverted, and square roots of the diagonal elements are extracted, which are the standard errors of $\tilde{\alpha}$ and $\tilde{\beta}$.

Kolmogorov-Smirnov Test

The Kolmogorov-Smirnov test compares the maximum difference of two cumulative distributions against a critical value based upon the criteria set by the statistician [62]. The cumulative distribution of a random variable, σ, is the probability that σ will take on a value less than or equal to some value. The test begins with an assumption that the property of the material under examination follows a specified cumulative distribution function, $F(\sigma)$. The cumulative step function or empirical cumulative distribution function of a random sample of N observations should closely resemble the specified CDF. If the specified CDF does not resemble the experimentally

obtained data, then it may not be the correct underlying distribution. Let the cumulative step-function of the sample be defined as

$$S_N(\sigma) = \frac{k}{N} \tag{3.20}$$

where k is the number of observations less than or equal to x. Then a new distribution can be constructed from the specified and empirical CDFs defined by

$$d = maximum\,|F(\sigma) - S_N(\sigma)|. \tag{3.21}$$

The value obtained for a specified distribution and a random sample of experimental data are compared against the critical value of the d distribution. The critical value is computed based upon the level of significance, α, and the sample size, N. Massey [62] has collected tables from previous researchers to determine the appropriate critical value for a KS test. The critical point corresponds to the meaning that in $\alpha \times 100\%$ of random samples of size N, the maximum absolute deviation between the sample CDF and the population CDF will be at least equal to the critical point value.

To test whether two empirical distributions are drawn from the same underlying distribution, the specified distribution, $F(\sigma)$, is replaced with a second empirical CDF, $S_N^0(\sigma)$ and carried out in the same way. The KS test is available as a function in MATLAB. The functions *kstest* and *kstest2* were used to perform the tests discussed here.

Akaike Information Criterion

The Akaike Information Criterion is a general criterion for model selection. The test computes the AIC value based upon the negative log-likelihood value, L, evaluated at the MLEs, $\tilde{\theta}$, and the number of parameters, p, defining the model. The equation to calculate the AIC for any model is [63]

$$AIC = 2L(\tilde{\theta}) + 2p. \quad (3.22)$$

The statistical model with the lowest AIC score is judged to be the best fit by the test. The number of parameters is included in the calculation to penalize models for increasing complexity to make for fair comparisons between models of different dimensions. The log-likelihood values are computed by the maximum likelihood method discussed previously which simplifies the implementation of this test.

Experimental Methodology

The section will cover the methodology used for the experimentally testing laid out in the Methodology section of Chapter I. First, the tensile testing apparatus used for single fiber testing will be described and the adjustments to account for sources of error are also explained. Next, the single fiber static loading testing set-up is explained along with the data smoothing and fitting algorithms used for strain rate data analysis. Finally, the UV and AO exposures are described along with the material characterization techniques used on the unexposed (or pristine) and exposed specimens to quantify the effects of the exposures.

Single Fiber Tensile Testing

Single fiber tensile testing was conducted on a TexTechno Favimat. The Favimat is a specialized machine for testing single textile fibers. The machine utilizes a 12 N load cell and specialized control software to reduce error in its force and displacement measurement systems. The MTS Tytron 250 tensile testing apparatus was used for tensile testing of the UV and AO exposed yarns. The breaking loads observed for the yarn specimens were 10-20 times larger than the breaking loads used for the single fibers. The

MTS Tytron 250 was initially used to conduct some tensile tests on single fibers, but the amount of noise in the signal was too high and prevented the collection of accurate breaking load results for single fibers. For comparison, the signal-to-noise ratio from a yarn test was approximately 261, but 14 from a single fiber test for both tests run on the MTS Tytron 250 with the same loadcell.

Single fiber tensile tests were conducted on CNT fibers with gage lengths of 10, 40, and 60 mm, at a strain rate of 0.1% of the nominal gage length per second, which resulted in a fiber fracture time on the same order of magnitude recommended by ASTM D3379. Tests were also conducted on 40 mm specimens with strain rates of 1% and 0.01% of the nominal gage length per second. Extension of the specimen was measured relative to the movement of the lower gripping mechanism. The upper gripping mechanism was static.

The Favimat produced a data file for each tensile test which contained the percent strain at failure, breaking load in Newtons, the linear density in units of tex, and the time to failure in seconds. The linear density units, tex, is a textile industry standard unit for linear density and corresponds directly to g/km in SI units. Each data file also included incremental load-strain data for each test.

Several tests were discarded because one aspect of the test was flawed by an abnormally high or low measurement of strain, breaking load, or fiber linear density. These flaws were attributed to sample preparation errors. Separation of some fibers from the initial yarn resulted in bunching or snarling, which may be the cause of the abnormal measurements.

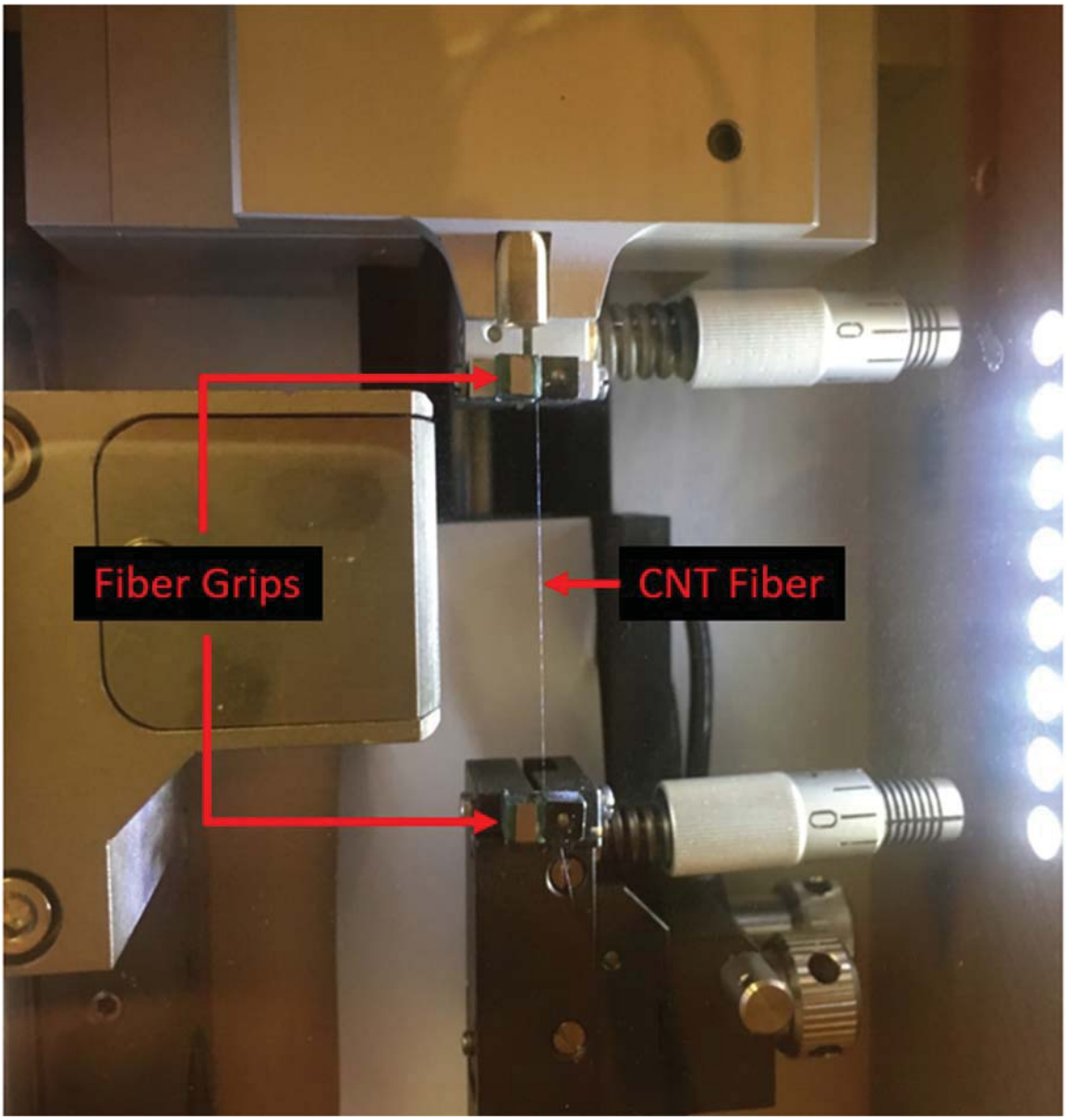

Figure 2: Favimat gripping a 40 mm gage length CNT fiber specimen

The Favimat directly gripped the specimen with rubber grips. Figure 2 shows the Favimat holding a 40 mm gage length CNT fiber prior to testing. Only tests which failed within the gage length were recorded. Fewer than 5% of the total number of tests failed in the grips so the direct gripping method was deemed acceptable. The tests which failed in the grips would last much longer than similar tests because the broken end would slowly

pull out from the machine grips. This feature of longer duration made it simple to program the data reduction script to discard any tests whose duration was more than two times the mean sample duration.

The direct gripping method can introduce clamp error because the stresses are not completely confined within the grips. The presence of clamp error means the effective gage length is longer than the nominal gage length. The additional length comes from small lengths of the fiber within the grips. For simplicity, this additional length is called clamp error in the calculations. ASTM D3822 was followed to determine the clamp error for the Favimat tester and used to calculate the effective gage length by the formula

$$\text{Effective Length} = \text{Nominal Length} + \text{Clamp Error}. \tag{3.23}$$

The clamp error is found by breaking at least ten fibers of three different gage lengths with the same rate of strain for all gage lengths. The variation in breaking strength must be no greater than +/- 3%. Then the apparent elongation at break versus the inverse of the nominal gage length are plotted. The intercept of this line with the inverse nominal gage length axis is the inverse of the clamp error value. The data from the CNT fibers tested in this research is plotted in Figure 3 which shows an inverse clamp error value of $-0.17602\ \frac{1}{mm}$. This value corresponds to a clamp error of 5.68 mm. The process was iterated with the clamp error of 5.68 mm factored into the elongation at break of the data used in the determination. The second run produced a clamp error of 5.5×10^{-3} mm, which was summed with the first step clamp error and rounded to the final value used in all length-based calculations, 5.69 mm. The Favimat machine would output data in units of percent strain, so the calculations in the data reduction scripts

convert strain at the nominal length to the correct value of strain at the effective length by multiply by the ratio of the nominal length and the effective length.

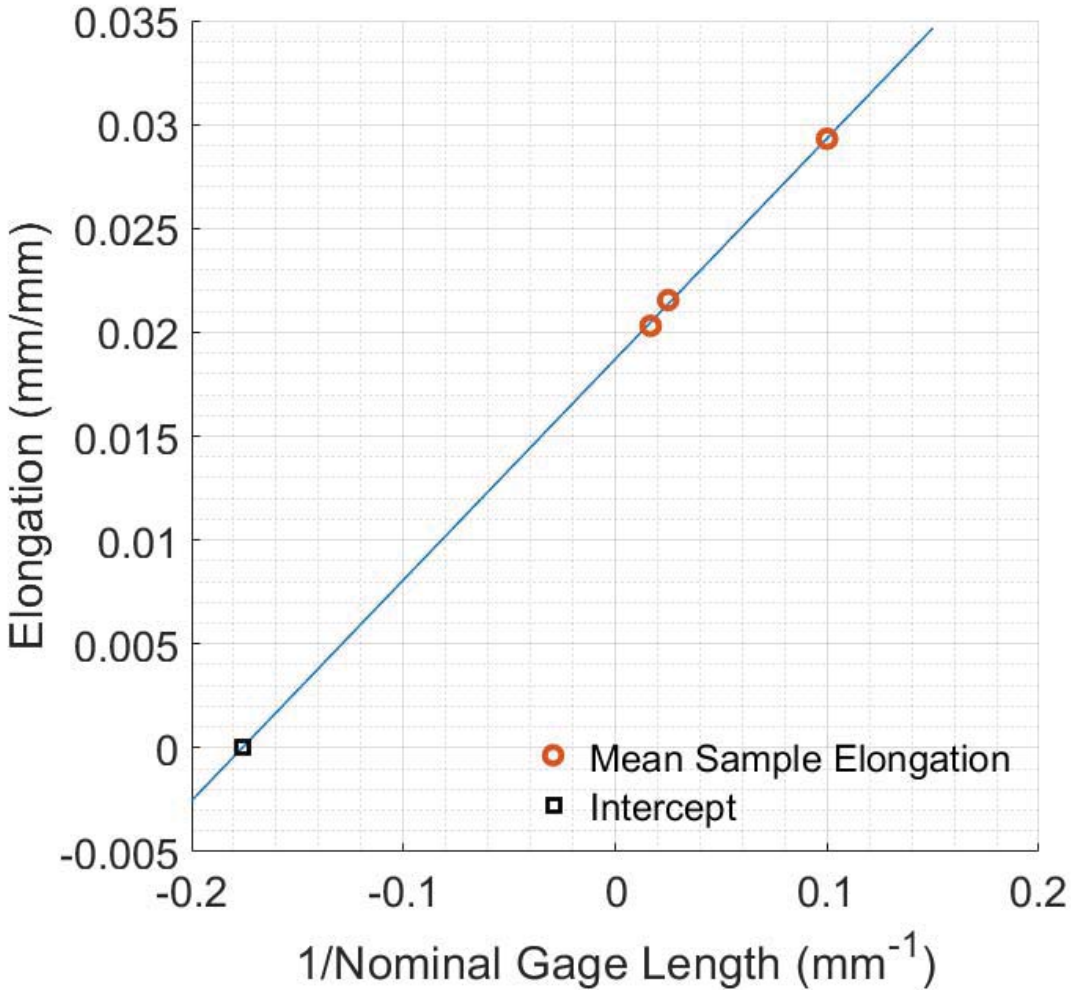

Figure 3: Clamp Error Determination Plot for Single Fiber Tensile Testing

For the sake of convenience and its wide acceptance in the textile industry, linear density determination by the vibroscope method was used to calculate the effective filament cross sectional area. The Favimat tester automatically measured linear density by the vibroscope method prior to each tensile test. The Favimat recommended speed and tension parameters for the linear density measurements were followed for each gage

length. The linear density of each filament was divided by the volumetric mass density to calculate the cross-sectional area of each test specimen. A circular cross-section was assumed and 1.3 g/cm^3 was chosen for the volumetric mass density based upon the manufacturer's data sheet. The actual CNT fibers were not circular, so exact validation of the volumetric density assumption value was not possible. Visual examination of fiber diameters yielded diameter measurements within the correct order of magnitude to give some confidence to the volumetric density assumption.

To verify the accuracy of the linear density measurements, the same length of fiber was measured 5 times. This procedure was repeated 5 times at three different applied tension values within the recommended range. The CVs of the linear density for all measurements generated by this procedure was 0.11%, which suggests the vibroscope method used is sufficiently accurate even with a variation in applied tension. This procedure was repeated several times throughout the course of testing on different fibers to ensure consistency in the method.

The linear density measurement was unable to yield measurements on the 10 mm gage length fibers. Instead, a 60 mm gage length fiber was placed in the machine for a linear density measurement, then the measured fiber was tensile tested in 10 mm increments using the single 60 mm gage length linear density measurement for all increments. Given the presence of clamp error, the material in the grips could not be considered untested and so the incremental steps did not include material that had been in the clamp from previous increments.

Additionally, it was observed during testing that the mean linear density measurements on the 40 mm and 60 mm samples were approximately 4-5% different.

This magnitude of difference was unexpected because the samples were all randomly sampled from the same group of fibers. Three long fibers that were untested from the original population of fibers were measured by the vibroscope method at nominal gage lengths of 60 mm and then at 40 mm, 5 times on each fiber at each gage length. It appeared that there was a difference in the linear density measurements of the same fibers but taken at different lengths. These samples were used to construct a linear relationship between the linear densities measured at 40 mm versus the linear density measured on the same fiber at 60 mm. Fortuitously, these three fibers spanned the range of observed linear density measurements and so could reasonably be expected to sufficiently describe the relationship between the linear density measurements of different gage lengths. This relationship was used to scale the 60 mm linear density measurements to the same size as the 40 mm linear density measurements.

Calculation of the elastic modulus is difficult in dealing with CNT fibers as compared to metals. The presence of slack at the beginning of the test and nonlinear material stress-strain behavior after the elastic region make it difficult to select the proper region of the curve for determination of the elastic modulus. No two tests were identical, and the data reduction script needed to process over 200 tensile tests. So, a method was devised to step through increments of the stress-strain curve and find the most linear portion. This portion was then used to calculate the elastic modulus.

Single Fiber Static Loading Testing

Static loading was performed on a custom testing rig with a hanging mass design as show in Figure 4. This rig is capable of testing five CNT fibers at a time and was developed for this research at the Air Force Institute of Technology (AFIT). Control

mechanisms used for tensile testing machines are adequate for short tests like tensile tests, but static loading can lead to instability in control systems. The applied loads for single fiber testing are very small. The load cell signal-to-noise ratio is low for single fiber tests on traditional tensile testing machines available at AFIT, which leads to instability in the control mechanisms. The more sensitive Favimat machine used for the single fiber tensile tests was not available for this testing because the machine does not currently have a static loading testing capability.

The custom-built static loading rig incorporates a hanging mass design, where individual masses are suspended from single fibers. The use of a hanging weight design ensures a consistent applied load for the duration of the test with zero variation. The hanging mass incorporated the core of a Linear Variable Differential Transducer (LVDT), which measured the elongation of the CNT fibers during static loading. The core of the LVDT is connected to the hanging mass and the specimen grip by small threaded rods. Only one amount of mass was used for all tests. The mass was approximately 36.51 ± 0.50 grams, which is the sum of a small 20g brass mass, the LVDT core, and the connecting rods. The mass corresponds to a force of 35.82 ± 0.49 cN.

The LVDT produces a voltage based upon the location of the core within the shaft of the LVDT housing. The voltage output of the LVDT ranges from $\pm 10.5\ V$, which corresponds to a measurement range of approximately $\pm 6.35\ mm$, which translates to a scaling relationship of $1.61\ V/mm$. The initial LVDT voltage was in the range of $\pm 10\ V$ at the beginning of each test and at test failure would register at $+10.5\ V$. A National Instruments Data Acquisition device was used to collect the voltage output of each LVDT. The LVDTs required a bipolar input voltage of $\pm 15\ V$ and $50\ mA$ current per

device. The bipolar input voltage was supplied by a dual output power supply in voltage control mode. The power supply fed 5 LVDTs arranged in parallel to minimize circuit complexity. The LVDTs used were TE Connectivity DC-EC 250 LVDTs.

The process of hanging weights on individual CNT fibers, which hold less than 0.5 N, is a delicate process. A special method was developed to delicately apply the weights without overloading the CNT fibers at the beginning of the test. The process began with creating individual, 3D printed plastic fiber holders for each fiber. The holders incorporated an epoxy well at each end where two-part epoxy was placed to anchor the fiber to the holder. The wells had channels on both ends through which the fiber entered and exited the wells. The holder incorporated a 20 mm gap between the wells, which was spanned by the anchored CNT fiber. This gap is called the gage length of the fiber. The gap was also spanned by plastic on the edges to hold the two well areas together until the beginning of the test. The epoxy was applied and allowed to cure at room temperature overnight, according to the epoxy manufacturer's instructions. The fiber holder also had 3 mm holes at each end. One hole was used to hang the holder to the static loading rig with a small metal pin. The other hole was used to connect the fiber holder to the hanging mass. Figure 5 shows a single plastic fiber holder with a single CNT fiber anchored across its length.

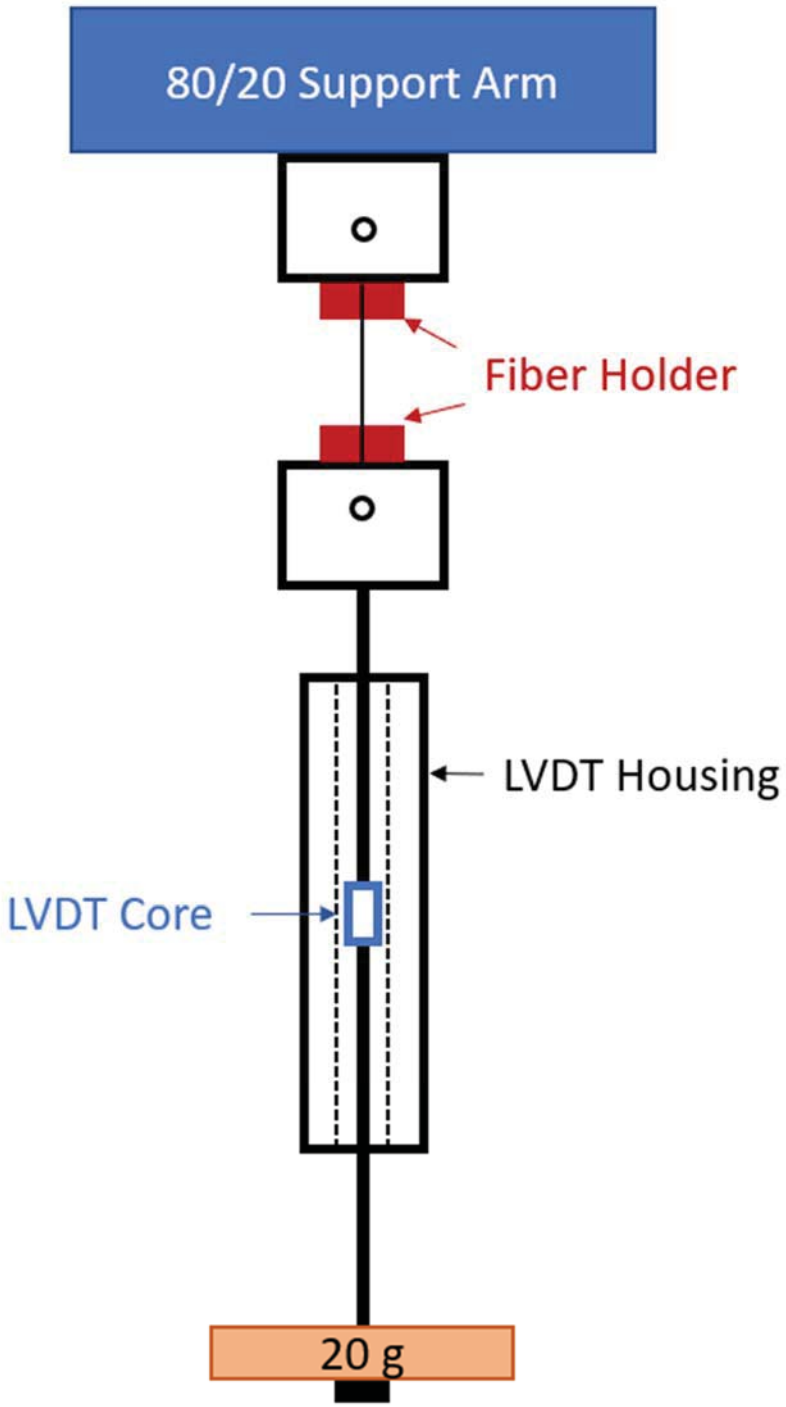

Figure 4: Notional diagram of creep testing apparatus

Once the fiber holder was hung from the test rig, then the hanging mass was attached to the fiber holder. Next, a mechanical stage was raised to remove loading from the fiber holder. Then, a soldering iron, heated to 500 deg F, was used to melt the plastic away in the gage length. At this point, the two ends of the fiber holder are no longer connected, and the fiber is carrying very little load. Figure 6 shows a fiber suspended in the testing rig with the plastic support arms melted away. The plastic fiber holder carried all mass up to this point and so prevented premature loading of the fiber. The mechanical stage, which was previously carrying the hanging masses, was slowly lowered, allowing the fiber to carry the hanging mass and begin the static loading experiment.

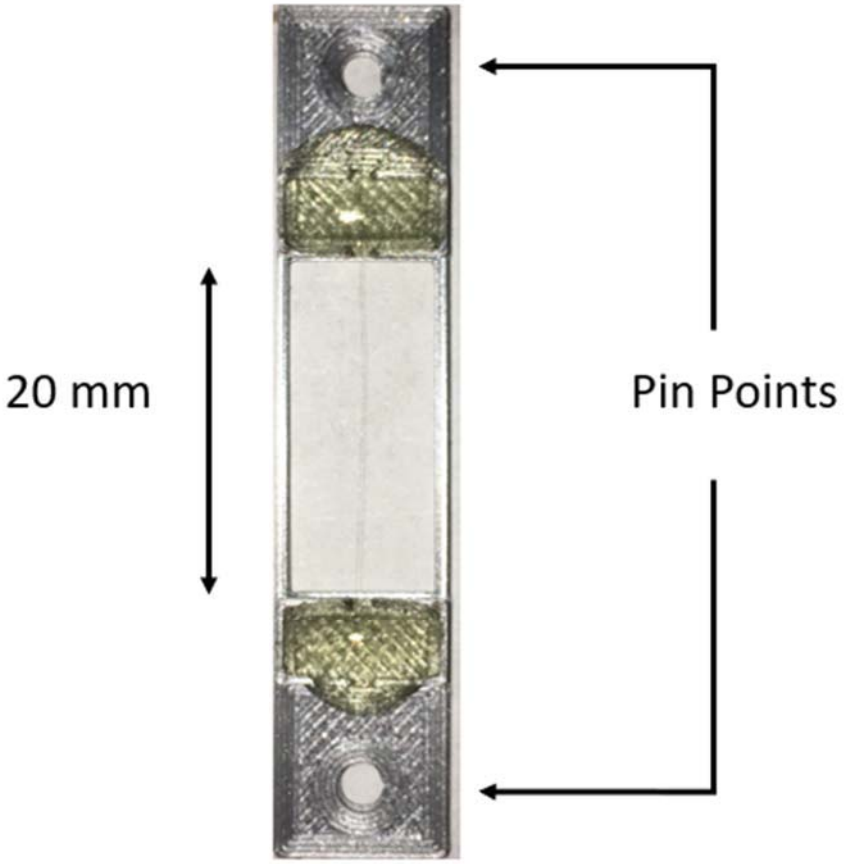

Figure 5: Fiber anchored in 3D printed plastic holder with two-part epoxy

Figure 6: Fiber holder with connector arms melted away by soldering iron

A simple LabVIEW program was made to record the LVDT readings during the static loading experiments. The sampling rate was set to 2 Hz for all tests. Data collection was initiated prior to the lowering of the mechanical stage. The program ran until all five specimens failed. The mechanical stage was kept close to the hanging masses to minimize shock to the LVDT sensors from impact after failure. After testing, the collected data was processed with a MATLAB script, which is discussed in the following section.

Sensor Data Reduction

The static loading voltage data recorded the voltage change of the LVDT as the fiber stretched. At fiber failure, the LVDT core fell and the voltage increased rapidly to $+10.5\ V$. The MATLAB data reduction script found the point of the high voltage and created a new pair of lists of data comprised of the time and voltage values prior to fiber failure. Figure 7 shows a plot of the LVDT data of one static loading test which is representative of all static loading tests. Figure 8 displays the static loading data after removal of the data after fiber failure.

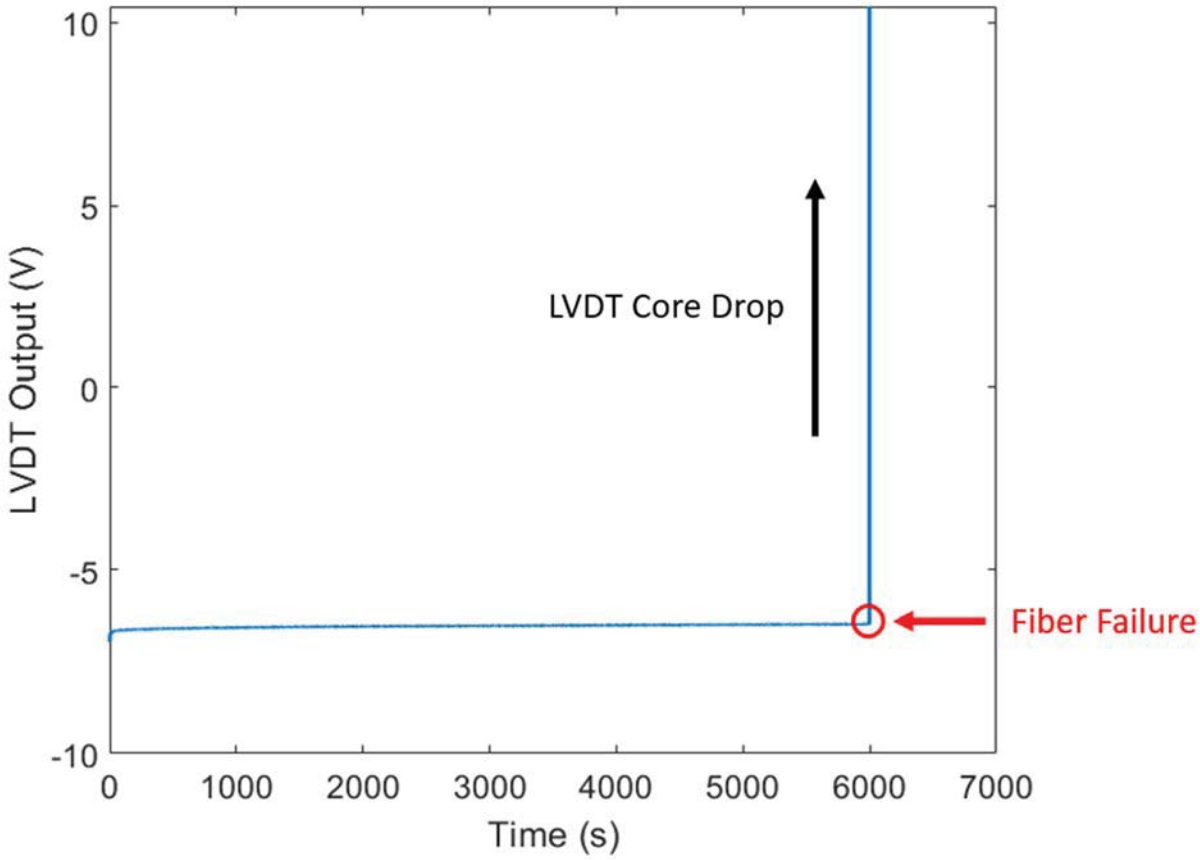

Figure 7: Raw static loading data

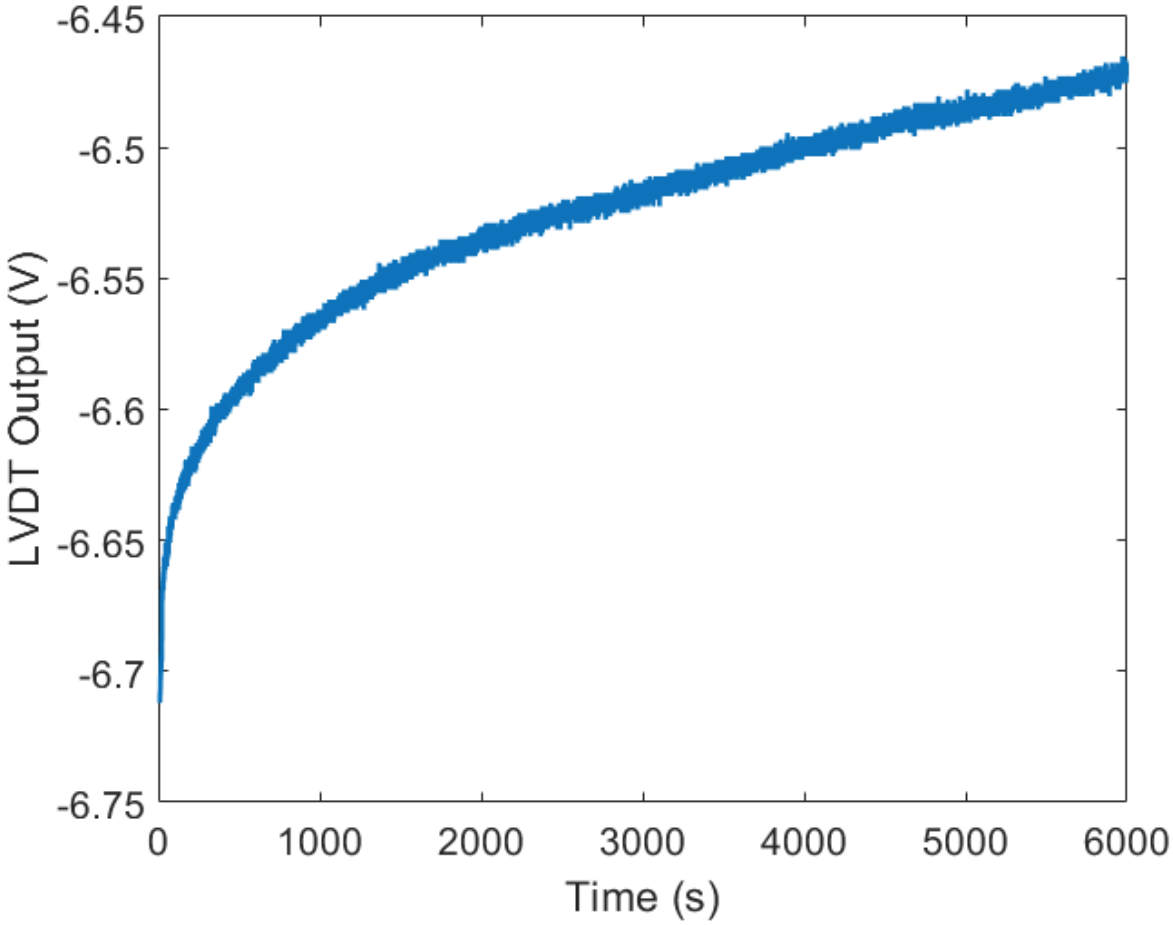

Figure 8: Plot of static loading data after removal of data after fiber failure

Next, the initial value of the voltage data values was subtracted from the entire list to obtain the change in voltage relative to the beginning of the test. The voltage values were converted to strain in this step by dividing by the LVDT conversion factor ($1.61\ V/mm$) and the gage length ($20\ mm$). Figure 9 displays the strain data after conversion. Notably, the strain at fiber failure is less than the average strain at failure values recorded in the single fiber tensile tests. This discrepancy is likely due to a shortcoming in the static loading apparatus design. When the fiber holder is pinned into the testing rig, the hanging mass is supported by the mechanical stage but the mass of the

LVDT core and connecting rods are being supported by the fiber after melting away the plastic posts. This occurs prior to data collection so there is unrecorded strain, which likely accounts for the reduced strain observed during the static loading tests. After data reduction, the strain at failure and time at failure are recorded for each fiber test.

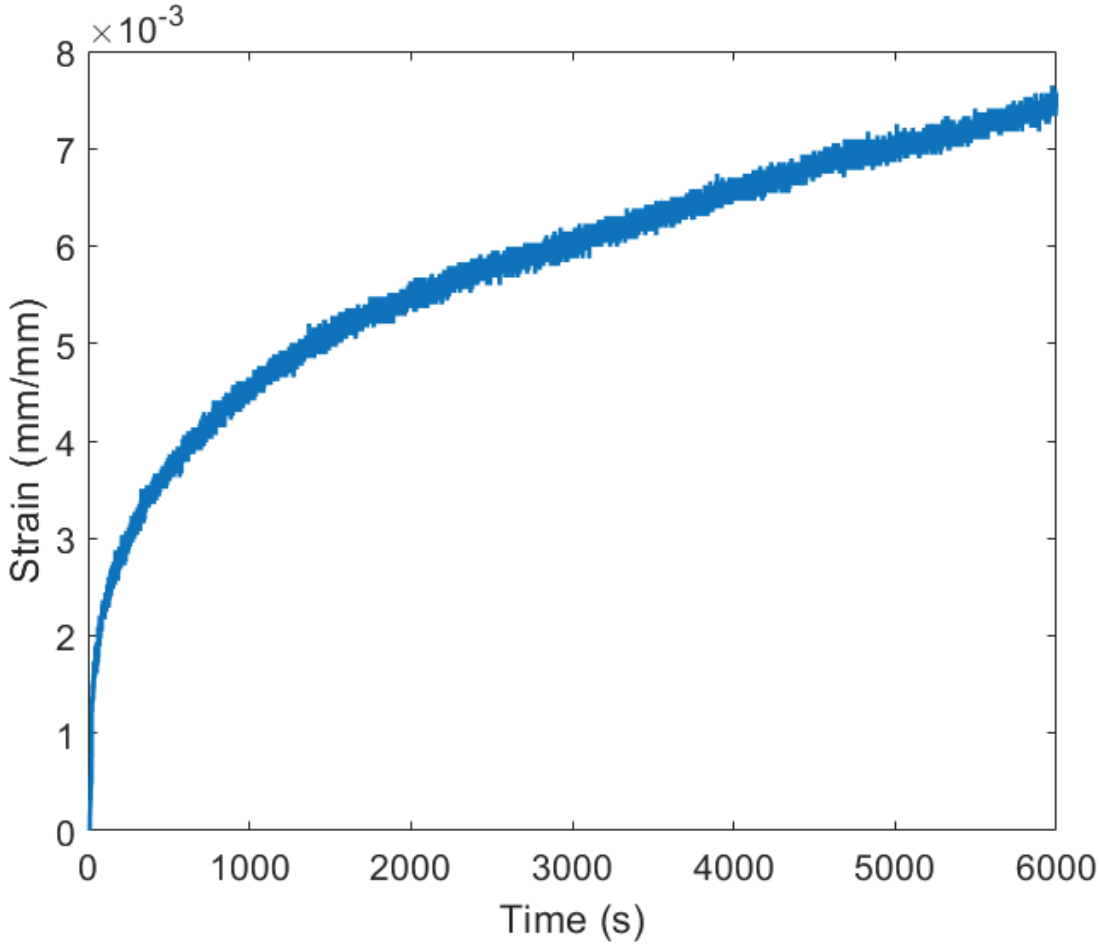

Figure 9: Plot of strain data

Atomic Oxygen and Ultraviolet Light Exposure

The AO exposure was conducted inside of a vacuum chamber, which was pumped down overnight before beginning exposure. Base pressure in the chamber before exposure began was on the order of 10^{-7} Torr. The AO beam was pulsed at 2 Hz. During

each pulse, the pressure rose almost to 10^{-3} Torr for a fraction of a second. The specimens were exposed to 150,000 pulses for a total exposure time of 21 hours. UV light was present in the beam source, which the AO exposure operators estimated to be of the same magnitude of the solar vacuum UV flux present in LEO. The AO flux, to which the samples were exposed, was equivalent to approximately one year of AO exposure in LEO.

The UV exposure was carried out at the Air Force Institute of Technology and lasted 1000 hours. The exposure was accomplished inside a vacuum chamber that was pumped down overnight prior to beginning the exposure. The chamber maintained a vacuum pressure on the order of 10^{-7} Torr for the duration of the test. The UV lamps used in this research had a peak intensity wavelength at 254 nm. The intensity of the bulbs was measured before and after the exposure by placing a UV light meter in the place of the yarn holder. The degradation in bulb intensity over time was unknown and was not measurable during the test. It was therefore assumed that the UV bulbs intensity degraded linearly. An exponential degradation of intensity yields approximately the same total intensity as the linear assumption. The linear degradation of bulb intensity yielded an average intensity of $0.75\ mW/cm^2$ over the 1000-hour exposure. NASA orbital environment design guidance estimates the intensity of UV light with wavelength of 254 nm in LEO to be $2.27 \times 10^{-2}\ mW/cm^2$ [12]. The average intensity of the bulbs used in this research was approximately 33 times the UV radiation experienced in this wavelength in LEO. Multiplying this intensity ratio by the test duration, leads to an approximate 3.77 years of equivalent constant LEO UV exposure. While exposing the samples to UV light, the electrical conductivity of two specimens was monitored. This

was done using the four-probe electrical conductivity technique sampled at 2 Hz for the entire exposure. One of the specimens was directly exposed to the light while the other was covered with a shroud to serve as a control specimen. The control specimen was incorporated to account for changes in yarn electrical conductivity due to diffusion of acid, which is promoted by application of high vacuum and elevated temperature. After exposure, electrical conductivity, mechanical properties, and piezoresitivity were evaluated to examine the effects of AO and VUV on the samples. Measuring mass erosion due to the AO flux is common in AO exposure tests, but the mass of the exposed yarns was too small to provide accurate measurements with available microbalances.

Electrical Measurements

All electrical measurements for the space environment exposure characterization utilized the four-probe resistance measurement method to accurately measure the electrical resistance, which was used in the electrical conductivity calculation for the CNT yarns. A short review of electrical properties and measurements is presented to explain the differences in measurement types and their use in this research.

Four-Probe Measurement Method

The electrical resistivity of a material is the property which dictates how that material resists the flow of electricity. The Greek letter used here for resistivity is ρ, unrelated in any sense to the parameter, ρ, discussed in Coleman's molecular kinetics model. Electrical conductivity is defined as the inverse of resistivity

$$\sigma = \frac{1}{\rho}. \tag{3.24}$$

Conductivity is calculated based upon the electrical resistance of a material along with its geometry by the equation

$$\sigma = \frac{l}{RA}, \tag{3.25}$$

where l is the length of the specimen, R is the resistance in Ohms, and A is the area of the material's cross section. The resistance of the sample, R, is a geometric property. It will change based on the length and shape of the material under test. Resistance is commonly expressed by Ohm's Law as:

$$R = V/I, \tag{3.26}$$

where V is the voltage differential across the material, and I is the current, defined in Volts (V) and Amperes (A), respectively.

Conductivity and resistivity are defined irrespective of length and shape. The resistivity of materials can be influenced by factors such as temperature and applied magnetic fields. Typically, the resistivity of metals increases as temperature increases and the resistivity of semiconductors decreases as temperature increases.

There are a few different techniques for measuring the resistance of a material. The simplest technique is the two-point, two-wire or two-probe technique. The most common example of the two-point technique is the familiar one of using a handheld multimeter to measure the resistance of a material by placing the multimeter's probes at different ends or terminals of the material. The technique is accomplished by attaching an electrically conductive wire, made of copper or gold, to each end of the material and applying a source current. Then a voltmeter, internal to the device supplying the source current, will measure the induced voltage across the material. The process may also make

use of a source voltage and an ammeter to measure the induced current. In either case, Ohm's Law as represented in Equation 3.28 is used to calculate the resistance of the material. Once the resistance is known, the cross-sectional area of the specimen and its length are measured which then are used together to calculate the electrical conductivity of the material with Equation 3.27.

The two-point technique is not an accurate measurement technique for materials with very low resistance. Contact resistance between the probes and the material under test can be much larger than the resistance of the material itself. Use of the four-probe technique is the solution to the contact resistance problem of the two-probe technique. The four-probe technique eliminates the contact resistance problem of two-probe resistance measurements. The four-probe technique involves supplying a source current through the length of a material via two probes at the edges of the material, called the outer probes. Then two different probes, referred to as the inner probes, with a voltmeter measures the induced voltage across a section of the material between the outer current supply probes. The inner probes carry a very small current because of a large resistor incorporated in the voltmeter design between the inner probes, allowing them to minimize contact resistance. The supplied current and measured voltage are used to calculate the resistance of the material. Only the distance between the probes where the inner probes contact the material matters for the electrical conductivity measurement. As in the two-probe technique, the cross-sectional area, the length of the inner part and the resistance are used with Equation 3.27 to calculate the electrical conductivity of the material under examination.

CNT Yarn Mechanical and Electromechanical Measurements

Pristine, AO, and UV exposed yarns were tensile tested with continuous in-situ four-probe electrical conductivity measurements to quantify the piezoresistive effect. This procedure combined the electrical conductivity, mechanical property, and piezoresistance measurements into one test.

Tensile testing was accomplished using an MTS Tytron 250 pneumatic tensile testing machine (Figure 10) with a 100 Newton load cell. Each specimen was approximately 50 mm long with 20 mm gage length. The excess material outside of the gage length was anchored with epoxy into a plastic holder (Figure 11). The yarn holders incorporated four wire channels where wires were laid to make electrical contact with the CNT yarn and act as the four probes of the electrical conductivity measurement. Small drops of silver paste were used to improve electrical contact and ensured that the probes and yarn did not move during testing.

Tensile testing was conducted by displacement control, utilizing a strain rate of 0.1% per second, which corresponds to 0.02 mm/s based upon the 20 mm gage length. The tensile testing data was sampled at approximately 1024 Hz. The in-situ resistance measurements were accomplished by supplying a 100-mA current through the outer wire pair with a lab power supply. The inner wire voltage measurements were collected with a NI USB-6009 module and custom LabVIEW program. The voltage measurement was sampled at a rate of 10 kHz. The voltage range of the voltage measurement module was $\pm$10V and the amplitude of the variation or noise of the voltage signal was approximately 10 mV, which yields a signal-to-noise ratio of 2000.

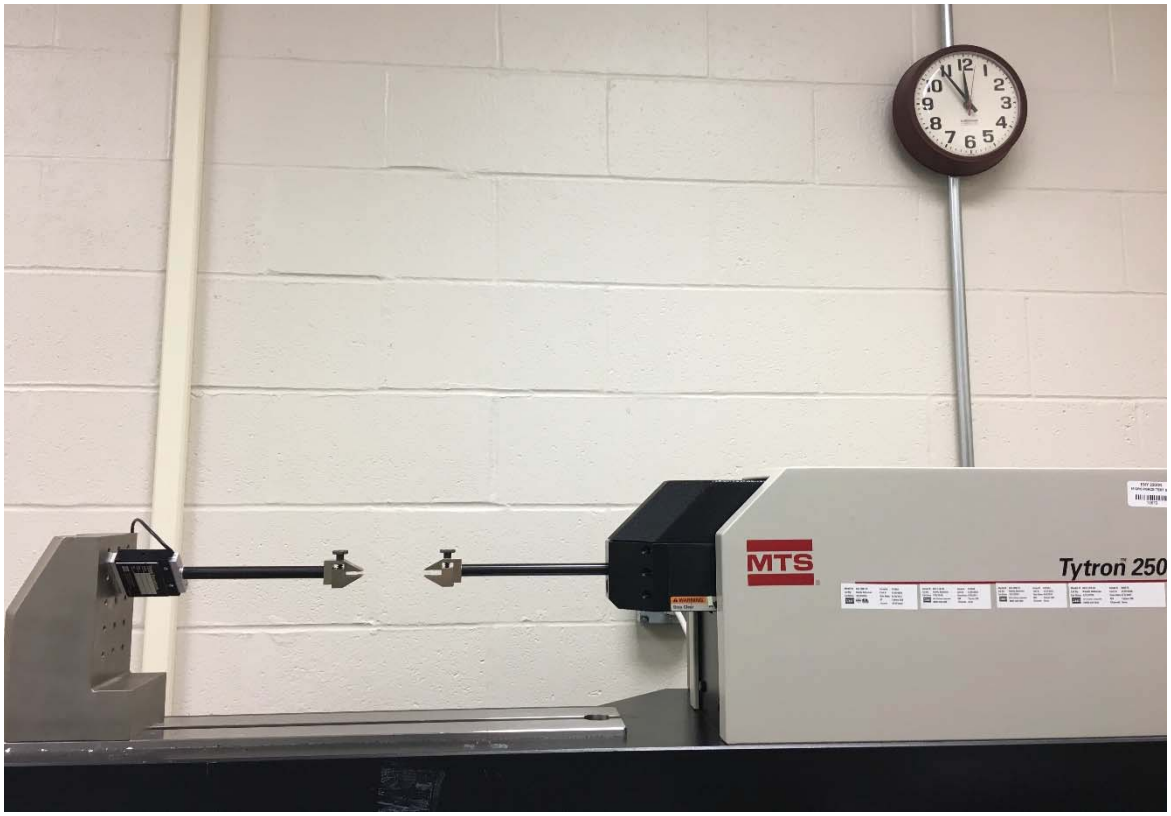

Figure 10: MTS Tytron 250 Tensile Testing Machine

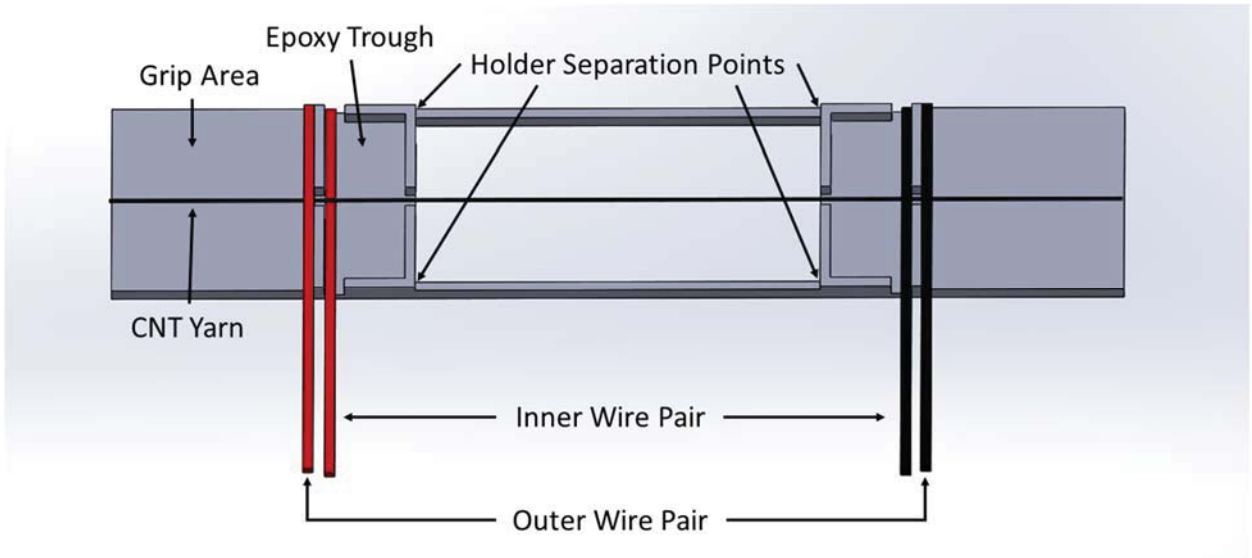

Figure 11: Plastic specimen holder design

The MATLAB *smooth* function was used to smooth out the signal noise in the list of vector values. The *smooth* function is a moving average filtering algorithm. The function was applied to the voltage values twice to arrive at the final signal used to compute the piezoresistive effect. Figure 12 is an example of one smoothed voltage signal. The successive smoothing steps are plotted on top of each other, showing the increased fineness achieved with each iteration.

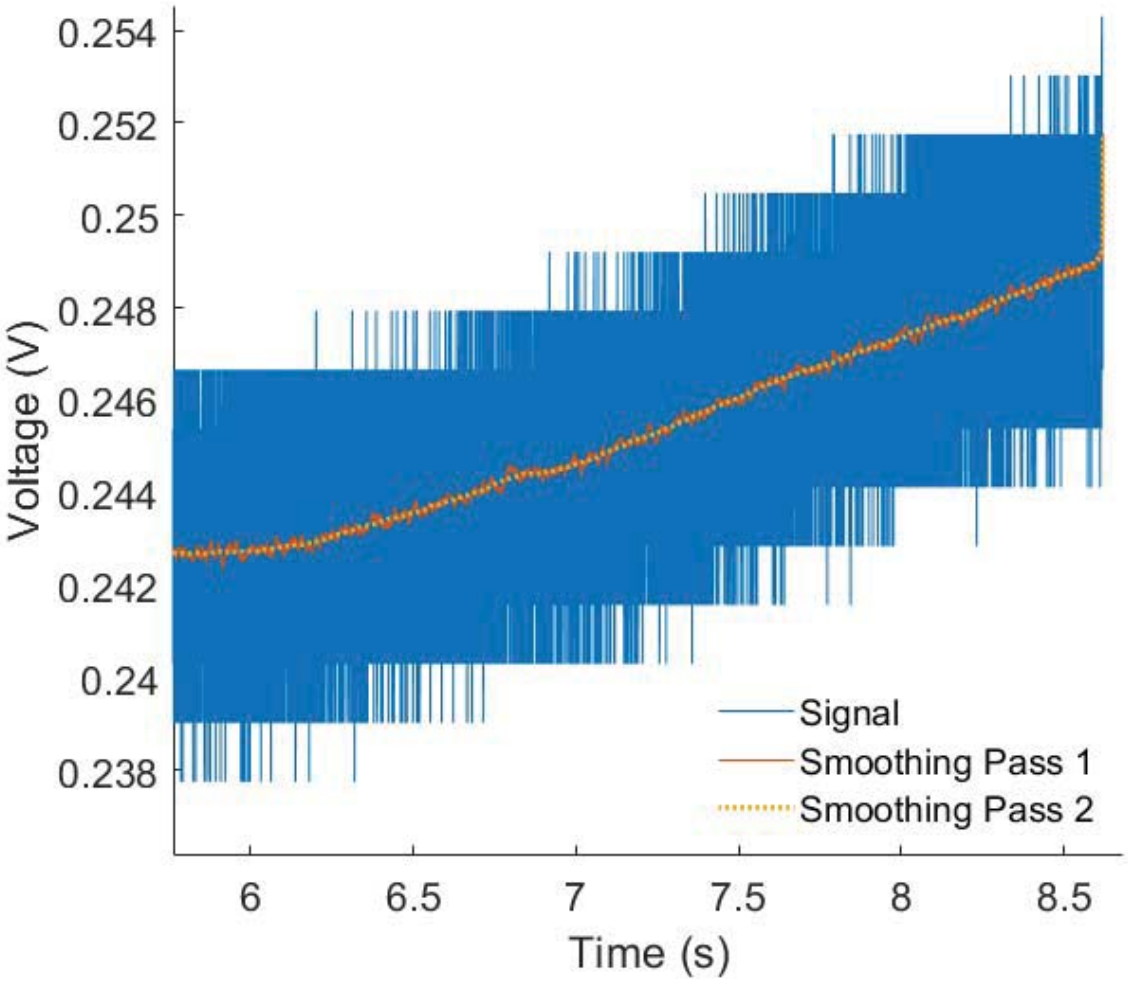

Figure 12: Signal Smoothing Example

The data collection scheme was not synchronized between the tensile testing machine and the voltage measurement module. The sampling frequency of the voltage module was approximately 10 times that of the tensile testing machine. To synchronize the data, the time of mechanical failure was matched to the time of the maximum voltage measurement before an open circuit (mechanical fiber failure) occurred. The time and voltage data lists from the voltage module were sampled at the corresponding times from the tensile testing data, which resulted in discarding approximately 90% of the voltage measurement data. The voltage values were used to compute the yarn resistance by Ohm's Law and the synchronized resistance and strain values were used to calculate the GF values to quantify the piezoresistive effect The synchronized strain and voltage data were then used to calculate the piezoresistive effect. This method was used to generate resistance values for the yarn at zero strain up to the strain at failure. Figure 13 displays an example of the strain and conditioned resistance data used to calculate the GF by the following equation

$$\mathrm{GF} = \frac{\Delta R/R_0}{\varepsilon}, \tag{3.27}$$

where ε is the mechanical strain of the yarn, ΔR is the change in resistance as the material experiences strain, defined as

$$\Delta R(t) = R(t) - R_{initial}. \tag{3.28}$$

$R_{initial}$ is the unstrained resistance of the yarn between the inner probes. The distance between the inner probes was 46 mm while only 20 mm of that distance experienced straining during the tensile test which necessitates scaling the initial resistance $R_{initial}$ by

the ratio of the strained to unstrained lengths of yarn to properly account for the limited material contributing to the piezoresistive effect which gives the reference resistance:

$$R_0 = R_{initial} \times \left(\frac{20}{46}\right). \tag{3.29}$$

Maximum GFs were computed at yarn failure. These GFs were averaged for all specimens of each exposure type to calculate the average GF.

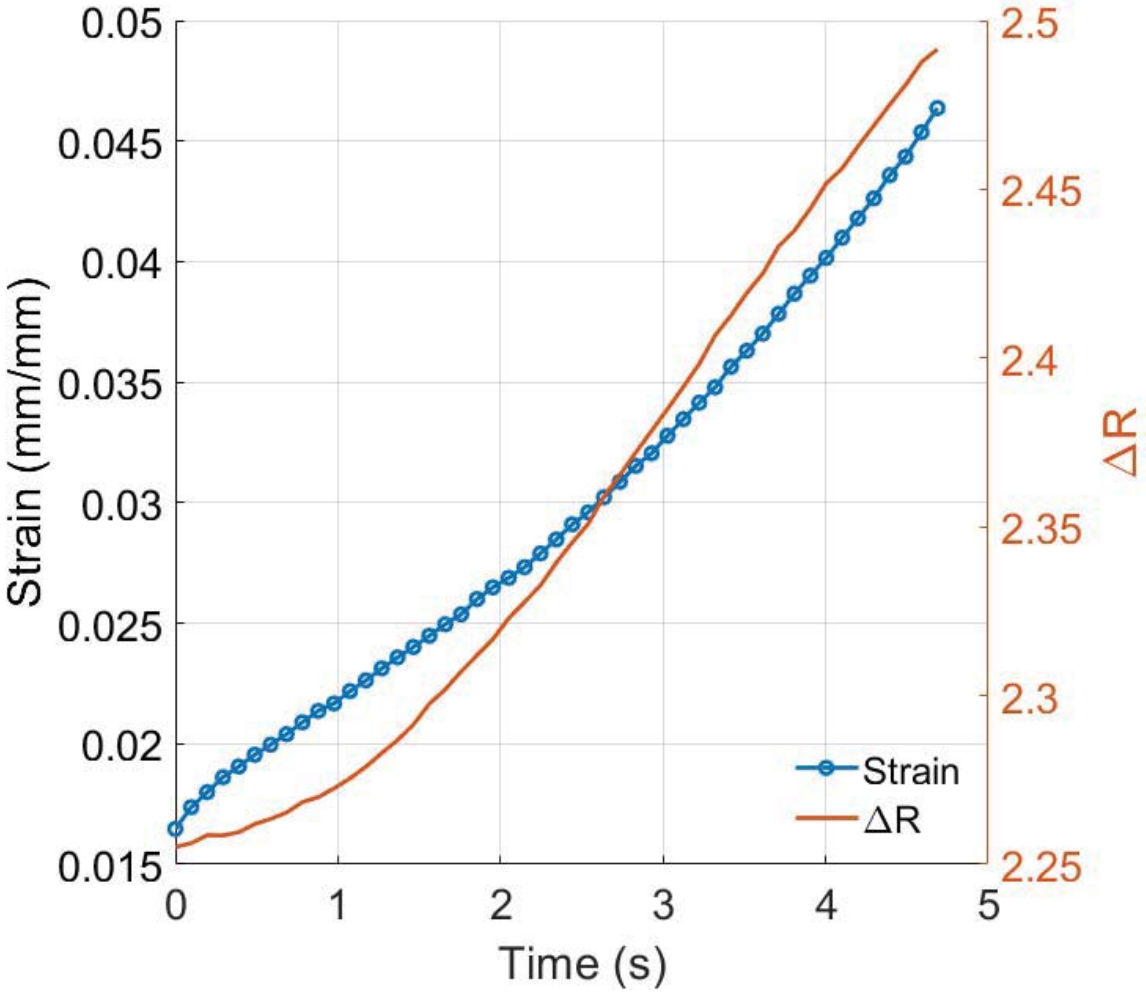

Figure 13: Strain and Resistance Data Synchronized for GF Calculation

The measured resistance at zero strain, $R_{initial}$, plugged into the electrical conductivity equation

$$\sigma = \frac{l}{RA} \tag{3.30}$$

was taken as the electrical conductivity measurement of each yarn. The fiber sat at rest for several seconds, and the several thousand measurements were averaged to yield the resistance value used for the electrical conductivity measurement.

Raman Spectroscopy

Sections of yarn were examined by Raman Spectroscopy before and after the UV and AO exposures to analyze possible induced defects and other morphological changes in the CNT yarn microstructure. A Renishaw inVia Raman Spectrometer with a 514 nm laser was used for the spectroscopy. SWNTs exhibit a peak in their Raman spectrum centered on a Raman shift of 1585 cm^{-1} (referred to as the G band or peak). This peak's name is derived from a similar Raman peak detected in samples with graphitic character.

The yarn samples also exhibit a less intense peak for a Raman shift around 1350 cm^{-1} which is referred to as the D peak or band. The ratio of the maximum intensity of the D and G peaks, or the D/G ratio, is frequently used to quantify the severity of induced disorder in CNT samples [11]. The D and G peaks were determined for the unexposed, AO and UV exposed samples using Raman Spectroscopy and the D/G ratios were determined to assess the extent of induced microstructural disorder in the CNT yarn surface.

Microstructural Characterization

Specimens from each exposure type were characterized visually by scanning electron microscopy (SEM) using the Tescan Maia-3 High-Resolution microscope located at AFIT. The microstructural characterization will also make use of a focused ion beam (FIB) microscope coupled with a SEM on the Tescan Lyra-3 system located at AFRL/RX. The FIB uses gallium ions to mill material away with microscopic precision. The FIB allowed viewing of the internal microstructure of the CNT yarns and fibers, where the SEM alone can only see the outer surface of the CNT yarns and fibers. Viewing the internal microstructure allows the investigation of the presence of voids and inclusions which may affect failure mechanisms. These microstructural analyses were important in analyzing the effects of the UV and AO exposures as well failure mechanisms taking place within the fibers subjected to various loading types. The microscopy investigation focused on identifying the defects which may affect fiber strength and contribute to gage length and strain effects.

Focused Ion Beam Milling Procedure

The specimens studied with the FIB are affixed to an aluminum stub with carbon tape or silver paste. The specimens were securely anchored to prevent being pushed around by the high energy gallium beam. The FIB is controlled by defining the area to be milled, the beam intensity, and the approximate depth. Beam intensity is defined in units of amperes and higher intensity beams mill material more quickly. The trade-off of using high beam intensity is that the beam will shoot more and higher energy ions outside of the defined beam area, causing unwanted damage to surrounding material. This overshoot area is called the beam tail.

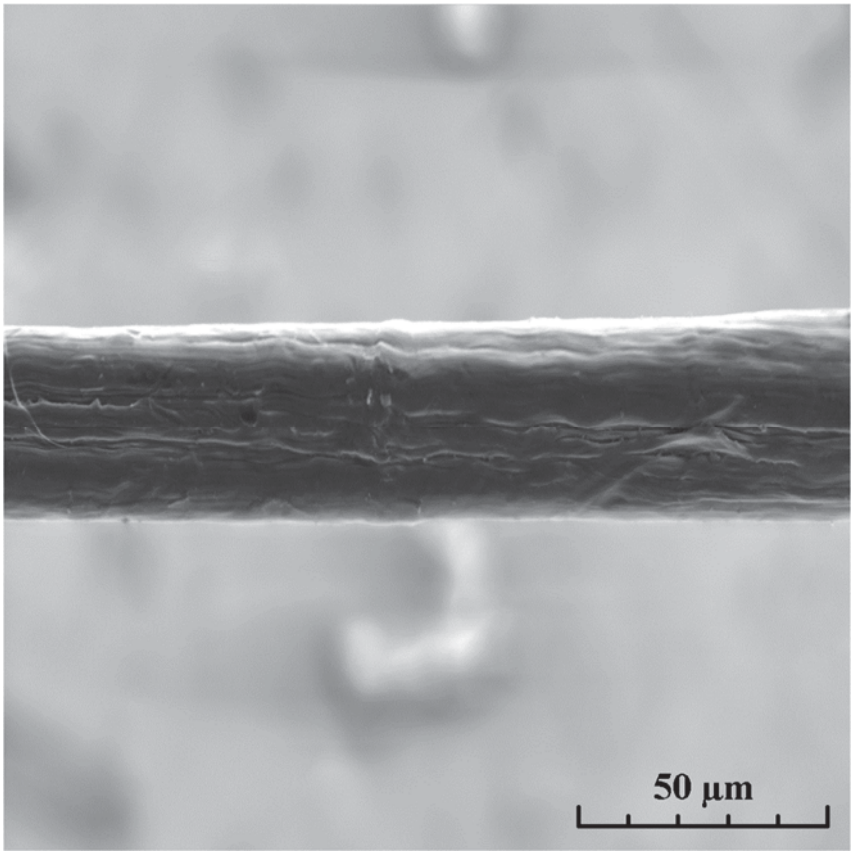

Figure 14: Pristine Fiber

Generally, a high intensity FIB current is used first to clear away large amounts of material to reach an area of interest. Then, successively lower intensity beam currents are used to smooth out the area to be studied. Figure 15 shows the fiber surface after the first FIB pass with a high beam current and depth of 5 μm. There appear to be steps in the material which is due to the non-uniform depth of the circular cross-section of the fiber. The final surface after cleaning up with smaller beam currents is presented in Figure 16. The vertical pits and curtains are artifacts of the FIB milling process and not indicative of

anything about the fiber itself. The horizontally oriented cracks in the fiber are pointed out to show the types of defects under investigation.

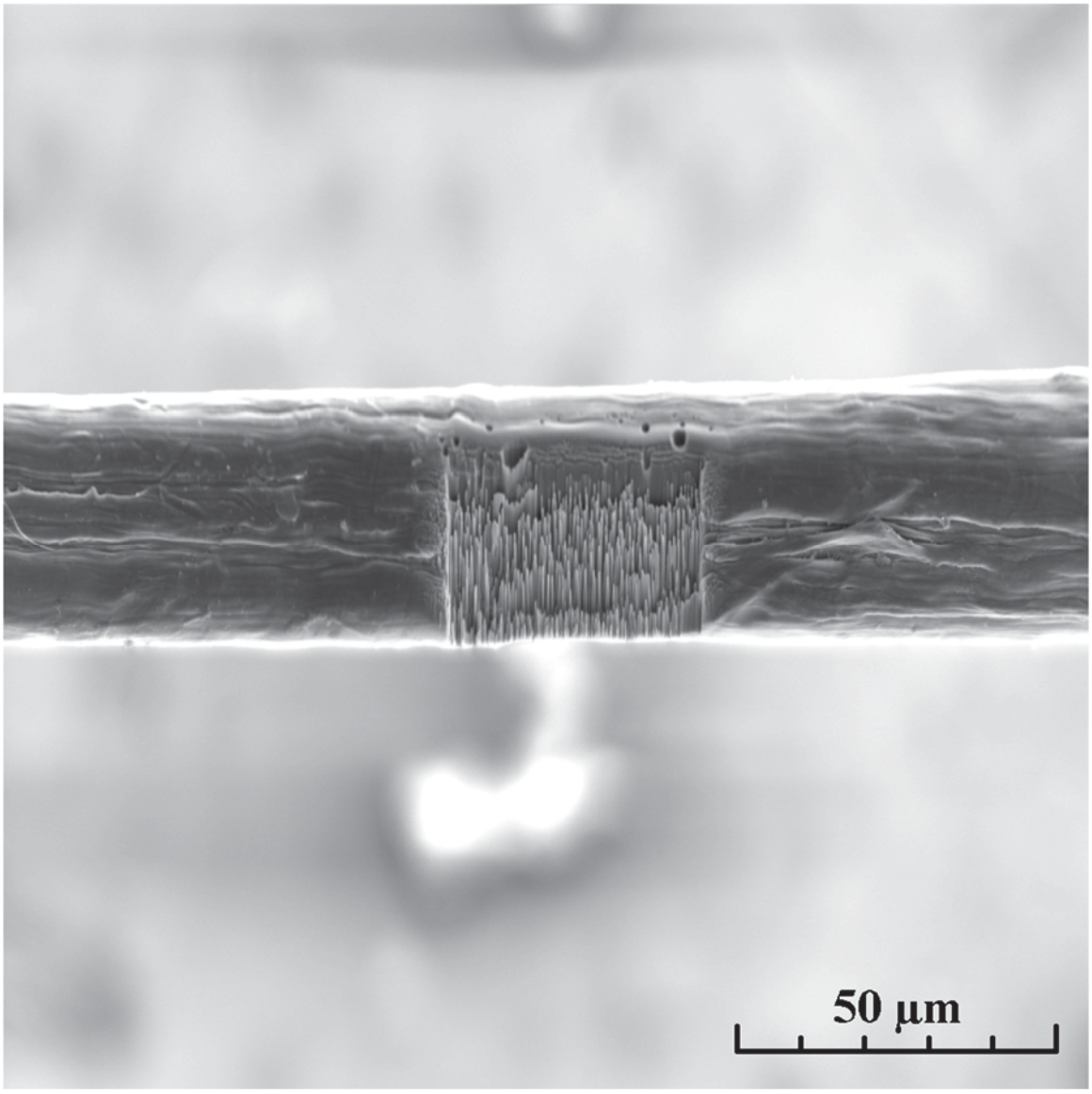

Figure 15: Fiber after first FIB pass

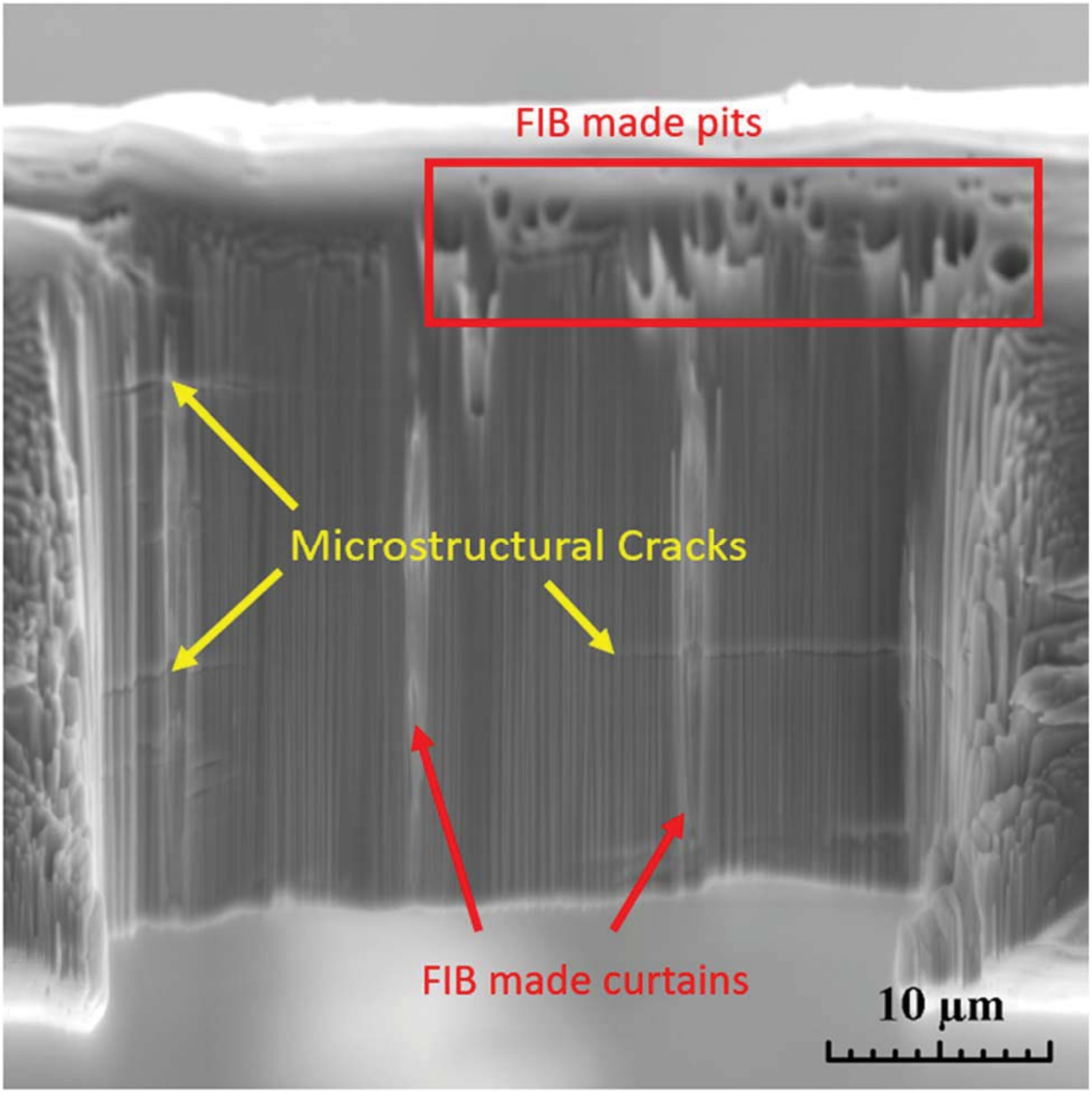

Figure 16: FIB surface with FIB process artifacts and microstructure

Summary

Statistical and experimental methods used in this research were outlined in this chapter. The statistical methods included discussion of parameter estimation by the ML method and model selection by the KS and AIC tests. Experimental methods included tensile testing of single fibers, static loading of single fibers, and mechanical, electrical and electromechanical characterization of CNT yarns. Space environment exposure set-ups utilized for this research were also described.

IV. Analysis and Results

Chapter Overview

This chapter covers all results conducted in this research which includes the results obtained for the single fiber tensile testing, the single fiber static loading testing, and characterization of the effects of the space environment on the mechanical, electrical and electromechanical properties of CNT yarns.

Results of Single Fiber Tensile Testing

This section discusses the results of the single fiber tensile testing. The first sub-section discusses the results of the tensile testing fibers of different gage lengths to characterize the length versus tensile strength relationship of these CNT fibers. The second sub-section discusses the results of tensile testing fibers of different strain rates to characterize the strain rate versus tensile strength relationship, which gives insight into the role of molecular bonding in the failure mechanism of these fibers.

Individual CNT fibers were separated from a 10 meter yarn and separated into 5 distinct samples. The 5 samples were chosen to examine the effects of gage length and strain rate on the CNT fiber's mechanical properties. The strain rates and gage lengths chosen were constrained by the limits of the single fiber tensile testing machine. The gage lengths tested were 10, 40, and 60 mm. Three samples of 40 mm gage length fibers were tested at the three different strain rates. The strain rates tested correspond to three orders of magnitude, $10^{-2}, 10^{-3}$, and 10^{-4} s^{-1}. The 10 and 60 mm gage length fiber samples were tested at a strain rate of $10^{-3}s^{-1}$.

The number of CNT fibers in each sample along with test parameters of each sample are summarized in Table 2. The results of all mechanical properties are summarized in Table 3. In the sample column, the number in parentheses is the strain rate of tensile testing used for that sample. The mean linear density is represented in the table as LD. The mean tensile stress measured at the point of fiber failure is represented by σ. The mean Young's or elastic modulus is represented by the letter E. Finally, the mean fiber strain at failure is represented by ϵ_F.

Table 2: Number of CNT fibers tested in each sample

$\dot{\epsilon}/L$	10 mm	40 mm	60 mm
$10^{-4}\ s^{-1}$		58	
$10^{-3}\ s^{-1}$	118	69	66
$10^{-2}\ s^{-1}$		62	

Table 3: Summary of mechanical properties of all single fiber tensile testing samples, standard deviations in parentheses

Sample	LD (tex)	diameter (μm)	σ (MPa)	E (GPa)	ϵ_F (%)
40 mm (10^{-4} s^{-1})	0.50 (0.05)	22.14 (1.17)	977.3 (86.34)	108.07 (14.70)	1.79 (0.28)
40 mm (10^{-3} s^{-1})	0.50 (0.05)	22.03 (1.14)	1043.8 (92.80)	114.19 (17.74)	1.83 (0.25)
40 mm (10^{-2} s^{-1})	0.50 (0.04)	22.14 (0.76)	1092.1 (87.45)	117.36 (17.04)	1.80 (0.23)
10 mm (10^{-3} s^{-1})	0.49 (0.03)	21.80 (0.90)	1090.1 (78.46)	117.15 (14.08)	1.92 (0.21)
60 mm (10^{-3} s^{-1})	0.52 (0.04)	22.66 (0.89)	1007.8 (112.57)	104.25 (14.90)	1.71 (0.28)

Gage Length Effects

The effects of gage length on the mechanical properties are examined first. As discussed in Chapter III, the direct gripping method used in the tensile testing machine can induce clamp error. This error causes the effective gage length to include portions of the fiber inside the grips because the clamps cannot completely immobilize the fiber at the edge of the gage length. To account for this source of error, the nominal gage lengths were adjusted to include the clamp error which yielded the effective gage length. The total additional length due to clamp error was found to be 5.69 mm. The following calculations and plots will use the effective gage length in lieu of the nominal gage lengths; however, the samples will be referenced by their nominal lengths.

The effect of increasing gage length on the tensile strength, the strain at failure and the elastic modulus are shown by the plots of the empirical CDFs of these properties in Figure 17, Figure 18 and Figure 19, respectively. All mechanical properties show

significant variation within each sample. The CDFs show that the properties all decrease with increasing gage length.

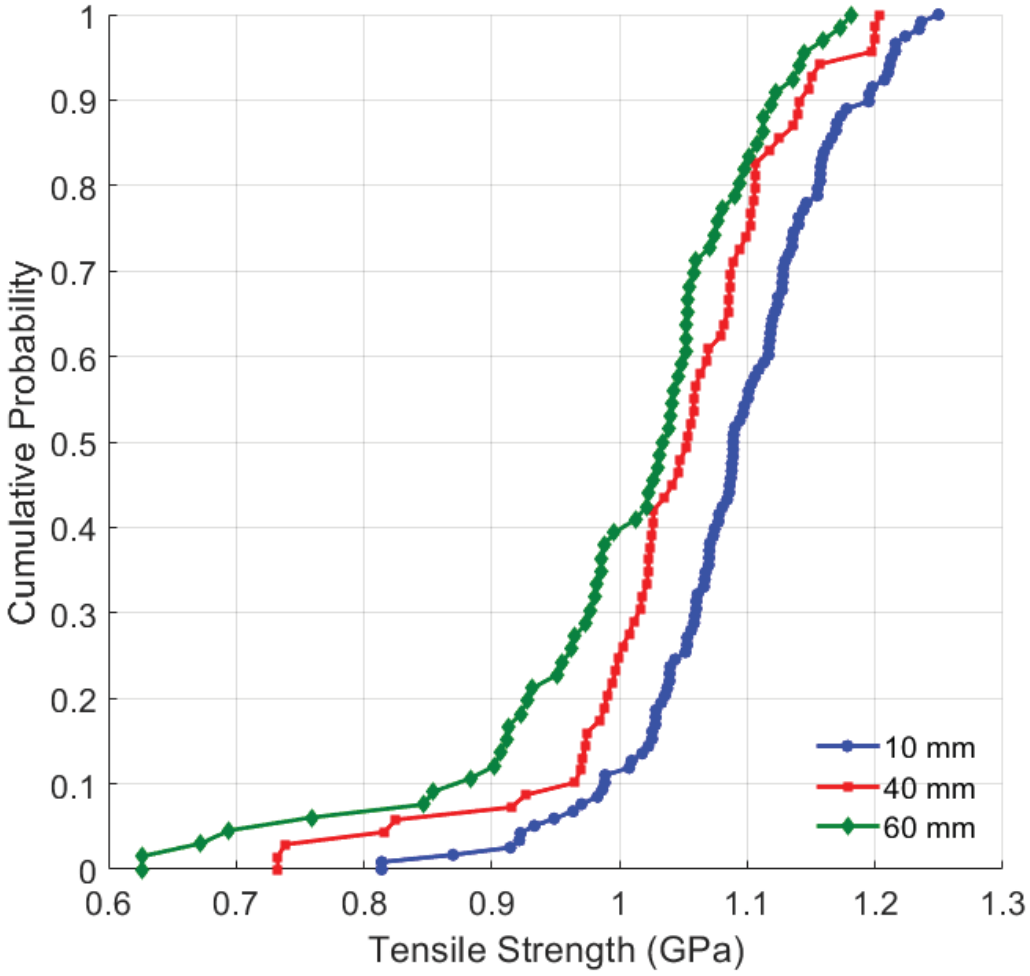

Figure 17: Empirical CDFs of tensile strength of variant gage lengths

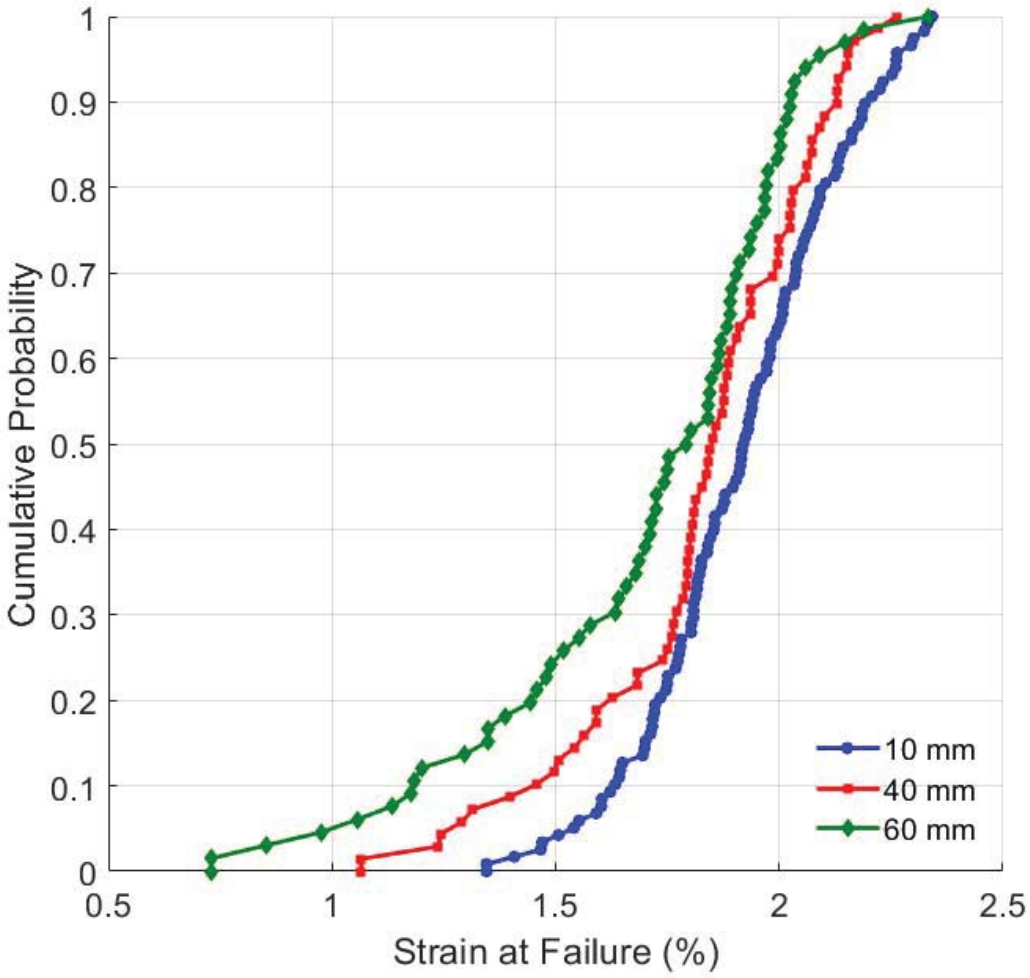

Figure 18: Empirical CDFs of strain at failure of variant gage lengths

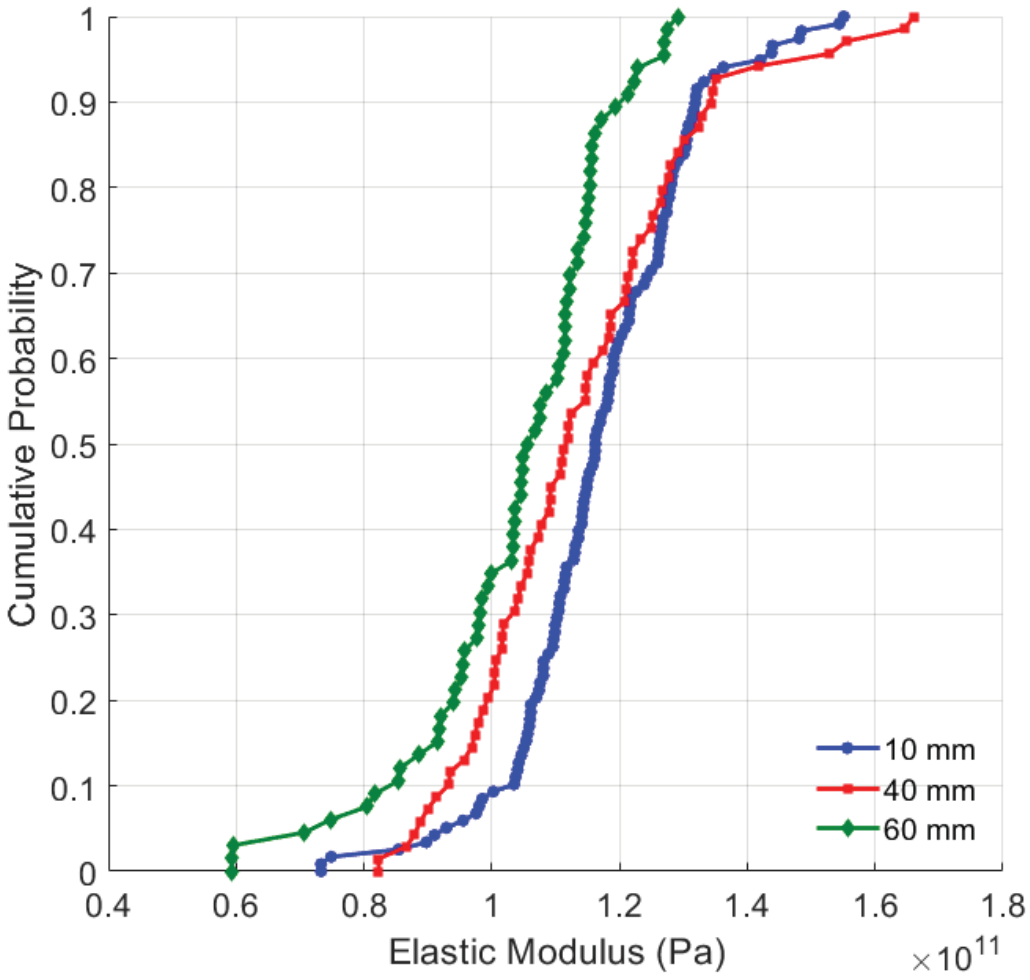

Figure 19: Empirical CDFs of elastic modulus of variant gage lengths

Table 3 shows that the mean value of each sample's properties decreases while their standard variation increases. This relationship is shown in plot of the tensile strength versus gage length with error bars representing the standard deviation in Figure 20. The R^2 value of 0.998 indicates strong correlation between tensile strength and gage length. The following plot, Figure 21, shows the empirical relationship between the mean and standard deviation of the tensile strength and gage length. This relationship yields a

tensile strength of 1.12±0.066 GPa at a gage length of 80 µm, typical for fiber loading length scales in composites [49].

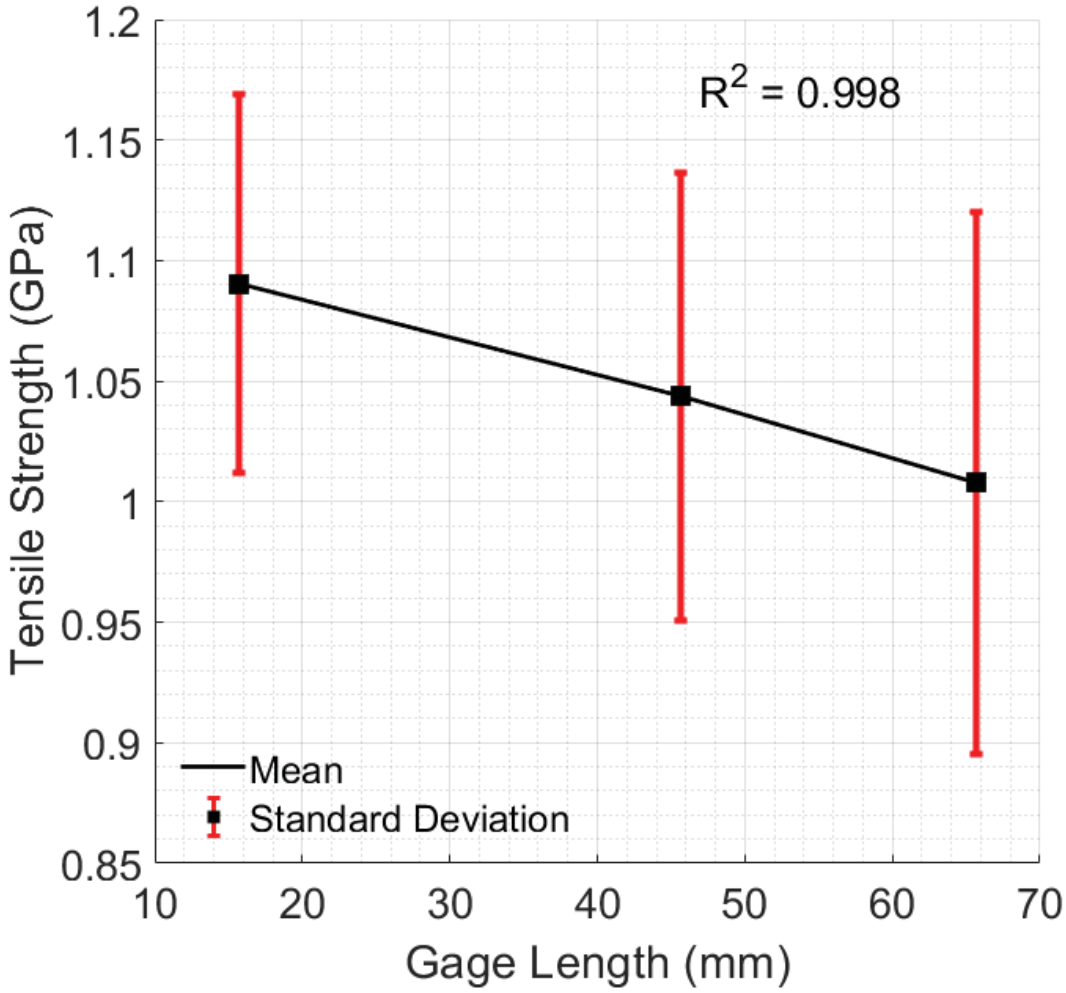

Figure 20: Plot of the mean and standard deviation of the variable gage length samples

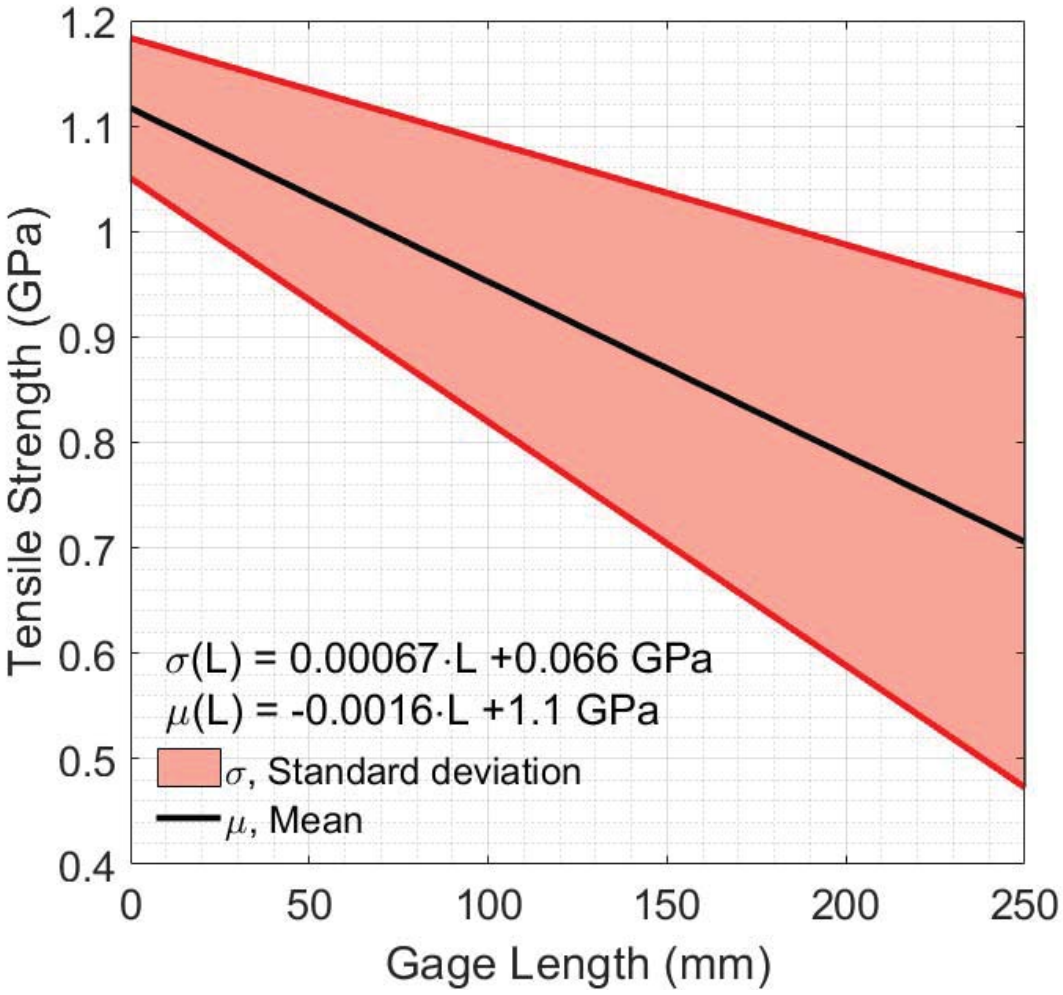

Figure 21: Empirical relationship between tensile strength and gage length, *L*

The decreasing tensile strength with increasing length relationship is an expected result of weakest-link theory, but the increasing standard deviation with length is not. In a classic work on the application of extreme value statistics to mechanical fracture problems, Epstein [65] shows for a variety of parent distributions combined with weakest-link theory that increasing length will result in constant or decreasing standard deviation of tensile strength. The observed divergence from the weakest-link model is a documented problem with the model in its application to real engineering materials.

Knoff [66] notes that for many materials, the weakest-link model underestimates the strength of very long specimens and does not account for increases in the CV. Possible causes for these departures stem from inhomogeneity of strength distributions from fiber to fiber, and the presence and influence of random defects [66].

The preceding analysis shows underlying complexity in the mechanical behavior of CNT fibers. This complexity is due in part to the structure of CNT fibers, which are composed of only micrometer long CNTs held together by weak van der Waals forces. This complex structure may require sophisticated micromechanical models to accurately describe the behavior of CNT fibers; however, the basic treatment of the fiber as a chain of links may provide some utility in describing the mechanical behavior of CNT fibers.

The weakest-link model and Weibull distribution, separately and together, are two common statistical models used to describe the tensile strength of fibers. The combined weakest-link Weibull model, described in Chapter III, has been used to assess whether fibers can be treated as a chain of links for strength modeling [38]. The relationship used to test this hypothesis is the CDF of the two-parameter Weibull distribution with a modification to the scale parameter, α, to incorporate weakest-link behavior to the model. The equation, Equation 2.5, and its modification, Equation 2.4, repeated here for convenience are

$$F(\sigma; L) = 1 - \exp\left[\left(\frac{\sigma}{\alpha_L}\right)^{\beta}\right]; \sigma \geq 0 \tag{4.1}$$

with the following relationship for the scale parameter, α, with dependence on length, L,

$$\alpha_L = L^{-\frac{1}{\beta}}\alpha. \tag{4.2}$$

Watson and Smith [38] tested the weakest-link hypothesis by determining the parameters of the Weibull distribution, Equation 4.1, for each gage length independent of Equation 4.2, and then for the case that the parameters are related by Equation 4.2 and comparing the resulting distributions.

The ML method was used to determine the statistical parameters. The MLEs of the Weibull distributions for the independent and dependent cases are presented in Table 4. The AIC test was used to judge which model provides a better fit to the data. The statistical model with the lowest AIC score between competing models provides a better fit of the data. The equation for the AIC score in this case is

$$AIC = -2 \ln L\left(\tilde{\alpha}, \tilde{\beta}\right) + 2p \tag{4.3}$$

where p is the number of parameters defining the model. The Weibull scale and shape parameters, $\tilde{\alpha}$ and $\tilde{\beta}$, are represented here with tildes because they are the MLEs determined for each model. In the independent case, where $\tilde{\alpha}$ and $\tilde{\beta}$ can vary for each distribution, $p = 6$. In the dependent case or weakest-link model, where $\tilde{\alpha}$ and $\tilde{\beta}$ are fixed and the three unique lengths are treated as parameters, $p = 5$. In the independent case, the log-likelihoods are summed giving, $AIC = 277.61$, and the dependent case yields, $AIC = 263.45$. Because the weakest-link relationship yields a lower AIC value, this provides statistical evidence that the weakest-link relationship provides a good mathematical model to describe the gage length effect on the tensile strength of CNT fibers. This result is significant because the range of lengths studied is relatively small and the statistical test provided clear evidence supporting the weakest-link hypothesis.

Table 4: Weibull parameters determined by ML estimation, standard errors in parentheses

Sample	α (GPa)	β	Log-likelihood
10 mm	1.12 (6.6×10^{-3})	16.19 (0.14)	-135.33
40 mm	1.08 (9.5×10^{-3})	14.23 (0.18)	-71.73
60 mm	1.05 (11.0×10^{-3})	12.28 (0.20)	-58.54
Weakest Link	1.15 (6.8×10^{-3})	15.17 (0.23)	-253.45

The preceding statistical examination of these fibers suggests that there are microstructural defects present in the fibers which give rise to the observed weakest-link behavior. Such behavior may be caused by several random distributions of flaws of varying sizes, severity, and frequency within the microstructure.

The microstructure of the CNT fibers was examined to attempt to identify the types of defects present within the fibers. This examination was carried out by making FIB cuts of several unstressed CNT fibers. Several FIB cuts were made laterally and longitudinally along the fiber axis. Figure 22 and Figure 23 show fiber cross-sections after making lateral FIB cuts of unstressed fibers. Figure 22 shows a cross-section with numerous large cracks through the microstructure, whereas the cross-section in Figure 23 exhibits no cracking. Figure 24 and Figure 25 show cracks and defects running down the length of the fiber. These views of the fiber were exposed by making cuts along the length of the CNT fibers with the FIB. These images show that the types and sizes of flaws can vary significantly along the length of a fiber within its center.

Headrick, *et al.* [23] has suggested that these defects are a primary factor in the strength of CNT fibers. The weakest-link analysis conducted in this research provides additional evidence that the frequency and severity of these defects are a limiting factor in the strength of CNT fibers. CNT fiber strength will not only benefit from the use of

longer CNTs as Tsentalovich, *et al.* [1] suggest, but also from process improvements which reduce the frequency and severity of microstructural defects.

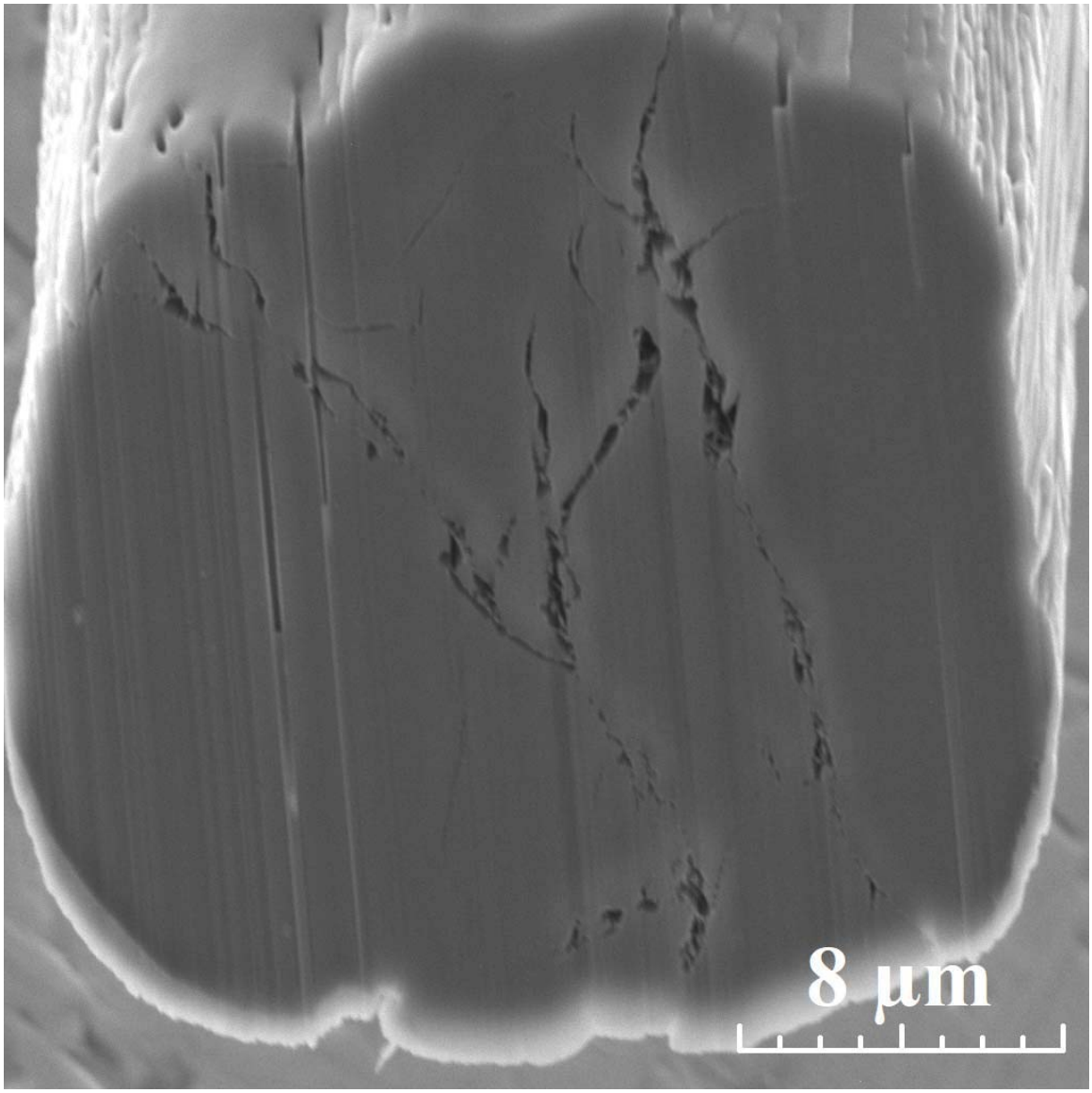

Figure 22: Lateral cut of an unstressed fiber

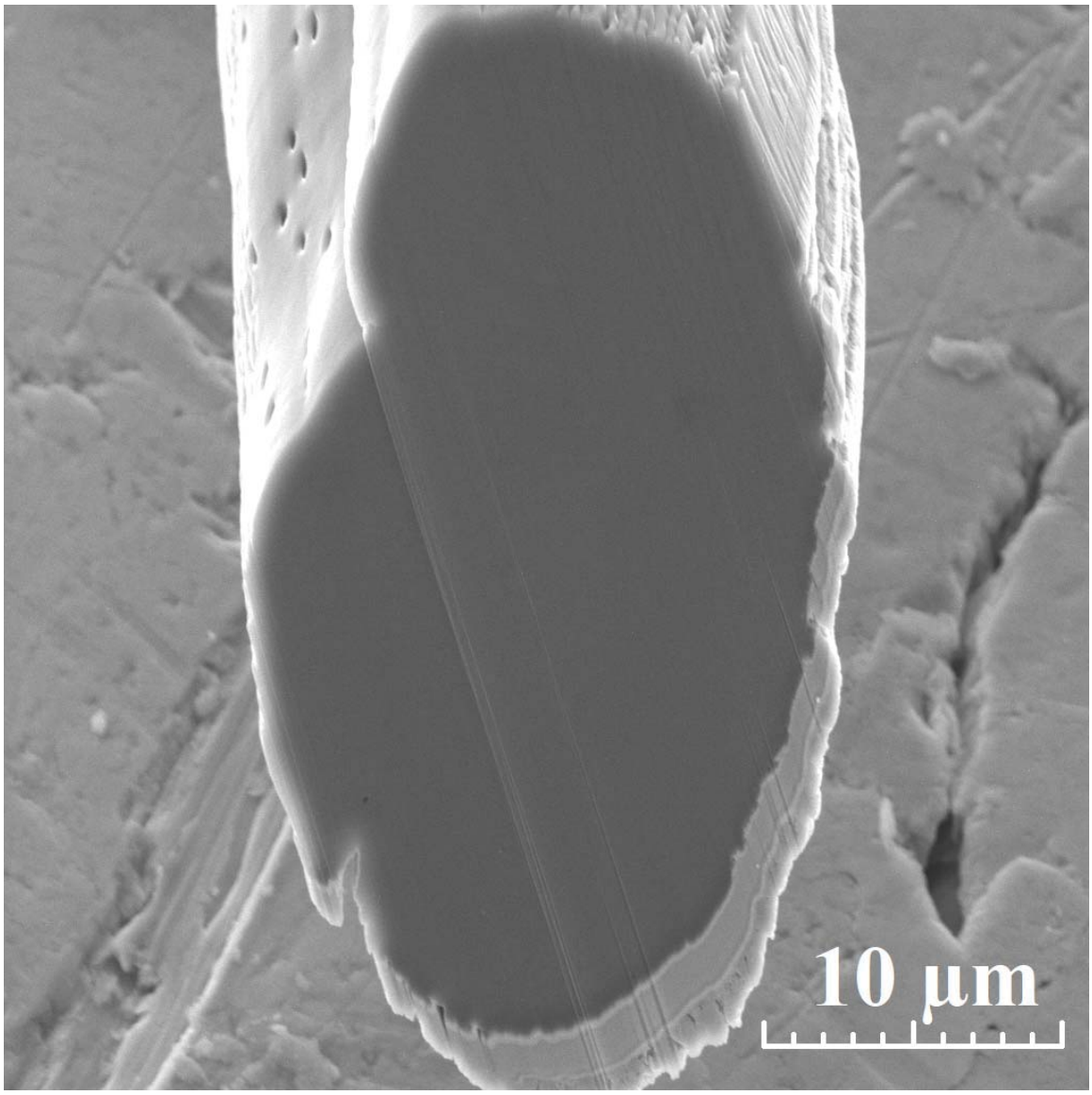

Figure 23: Second lateral cut on unstressed fiber

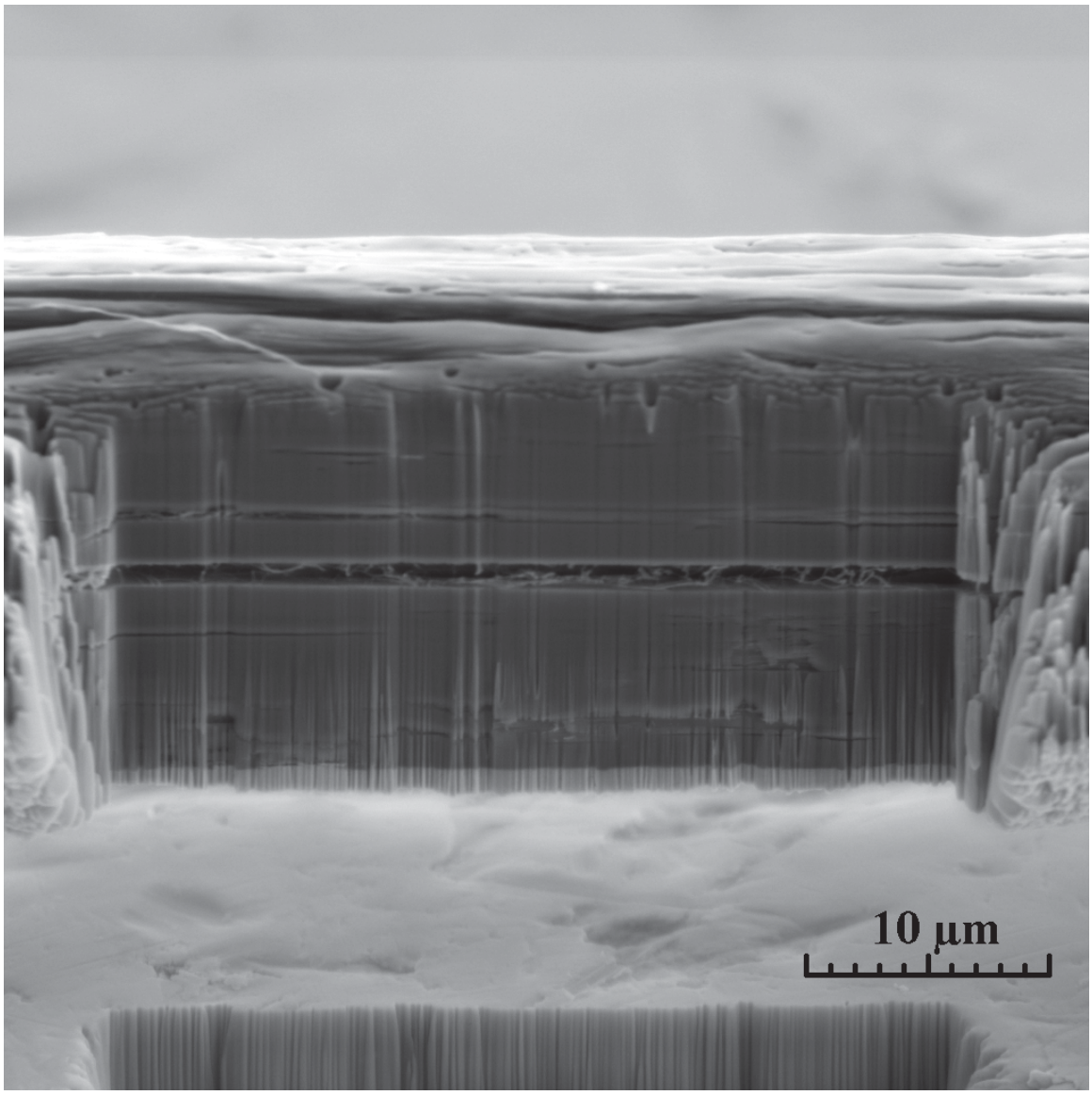

Figure 24: Lateral FIB Exposed Section of Unstressed Fiber

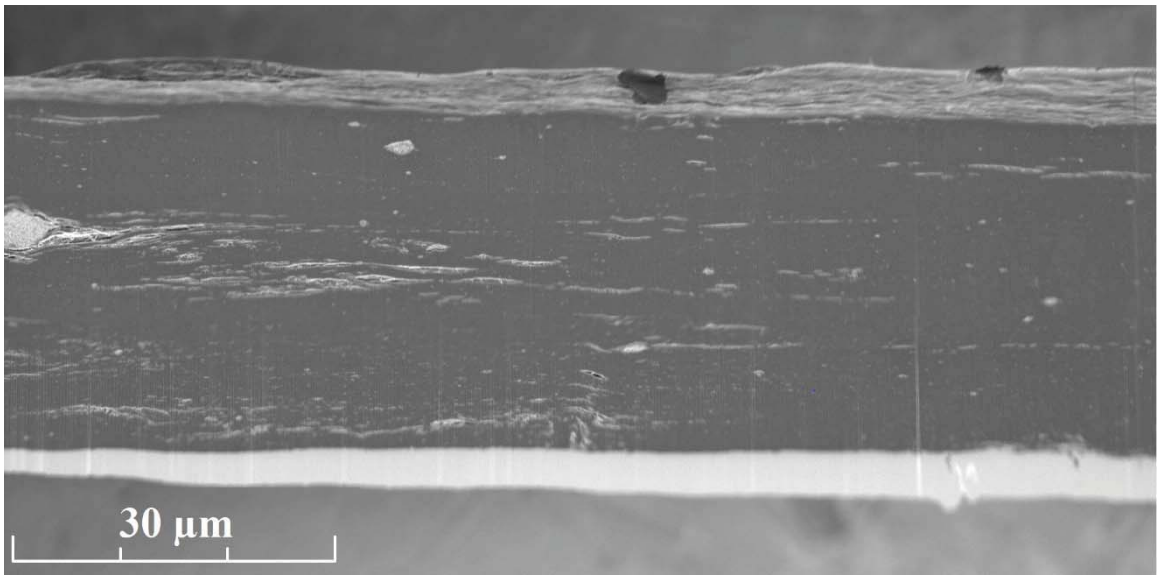

Figure 25: Lateral FIB Exposed Section of Unstressed Fiber

Strain Rate Effects

The effect of strain rate was studied by testing 40 mm samples at nominal strain rates of 10^{-4}, 10^{-3}, and $10^{-2}\ s^{-1}$. Representative stress-strain curves for each strain rate are shown in Figure 26. The representative curves chosen most closely adhere to both the mean stress and strain at failure for the sample represented. All curves exhibit elastic behavior up to approximately 3×10^{-3} strain and inelastic or plastic behavior beyond that point. Similar behavior has been observed for dry-spun yarns with comparable strength [67]. The similarity in shape between curves indicates the failure mechanism is similar between strain rates.

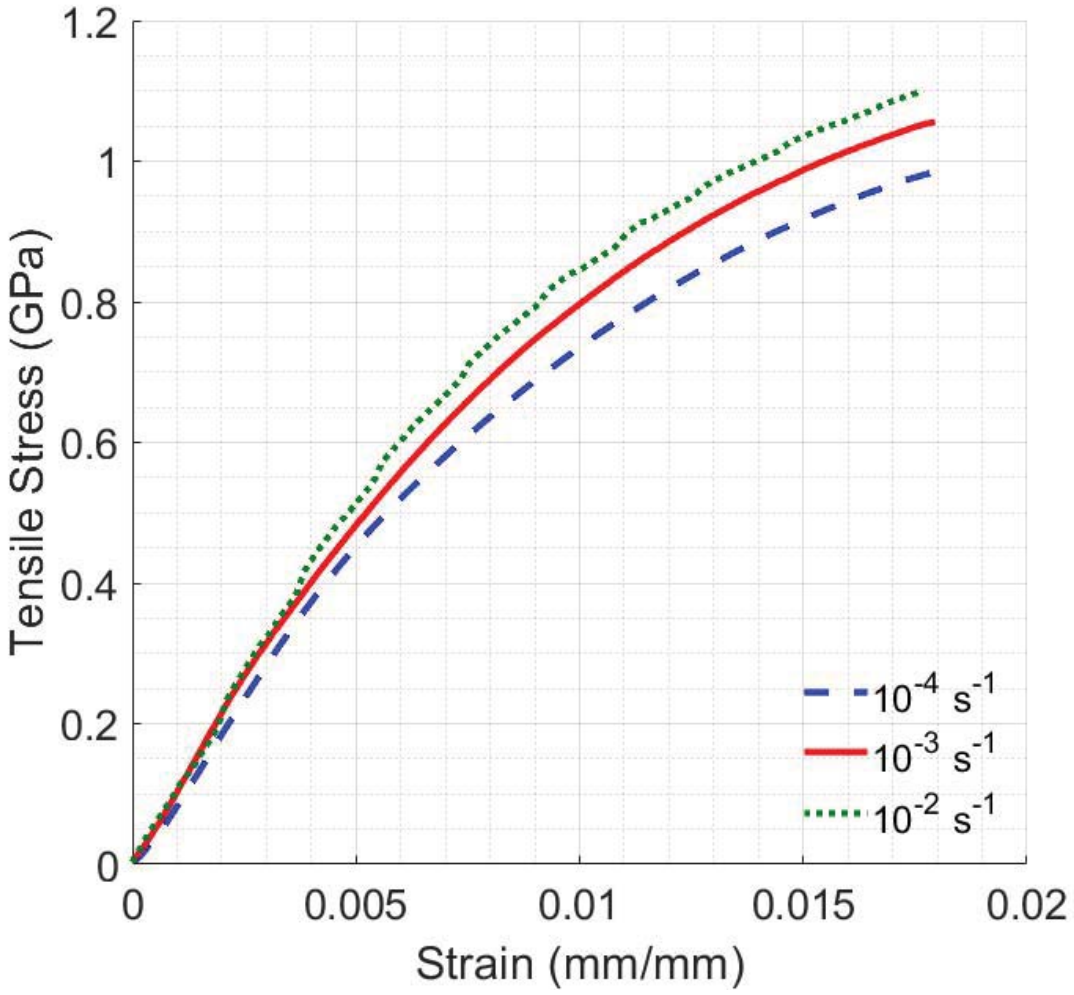

Figure 26: Representative stress-strain diagrams of each strain rate sample

The empirical CDFs for the tensile strength, strain at failure, and elastic moduli of the different strain rate samples are presented in Figure 27, Figure 28, and Figure 29. The tensile strength CDFs show a clear relationship between increasing strain rate and increasing tensile strength. The strain at failure CDFs appear to be unchanging and this is confirmed by KS testing, which does not reject the hypothesis that all three sets of strain data are drawn from the same continuous distribution at the 5% significance level. The change in elastic modulus is small between samples, the KS test is not able to distinguish

between the modulus CDFs produced by the lowest and moderate strain rate or the moderate and highest strain rates.

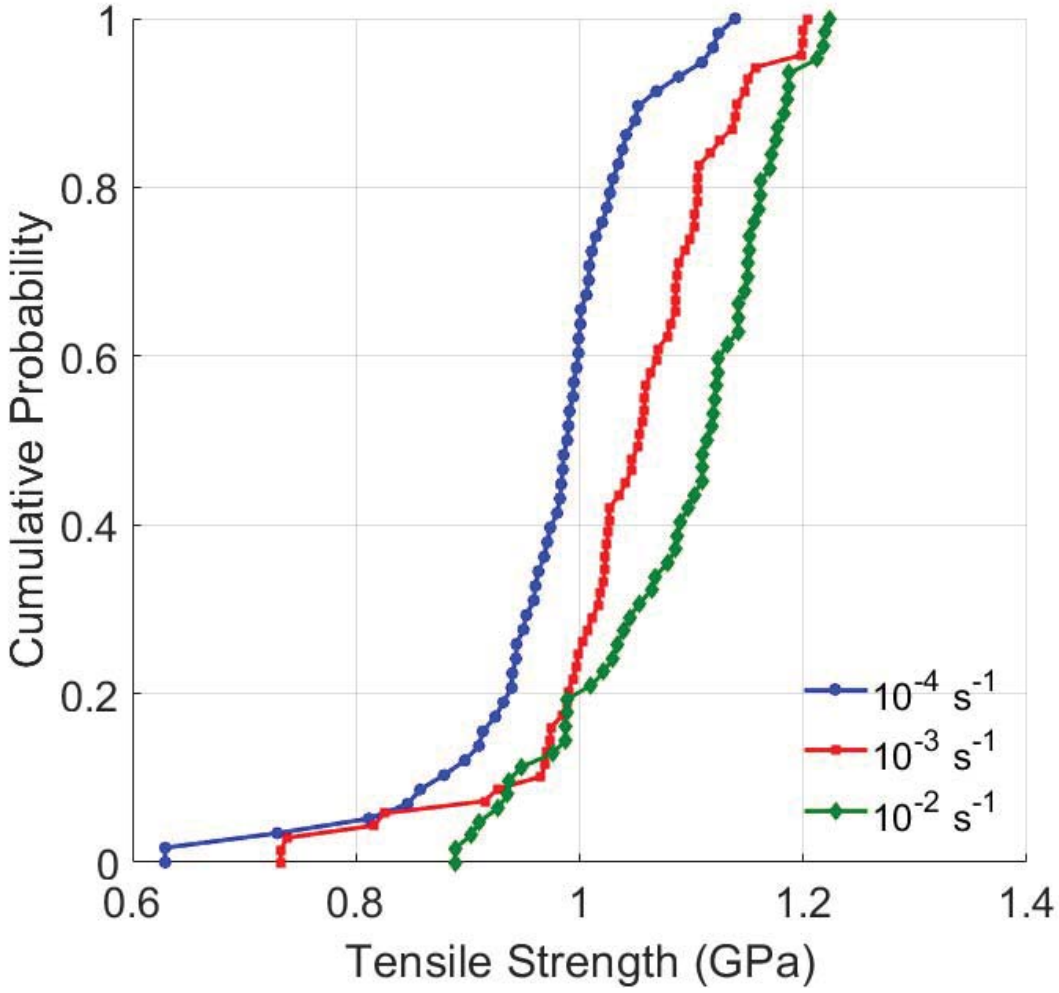

Figure 27: Empirical CDFs of tensile strength of variant strain rates

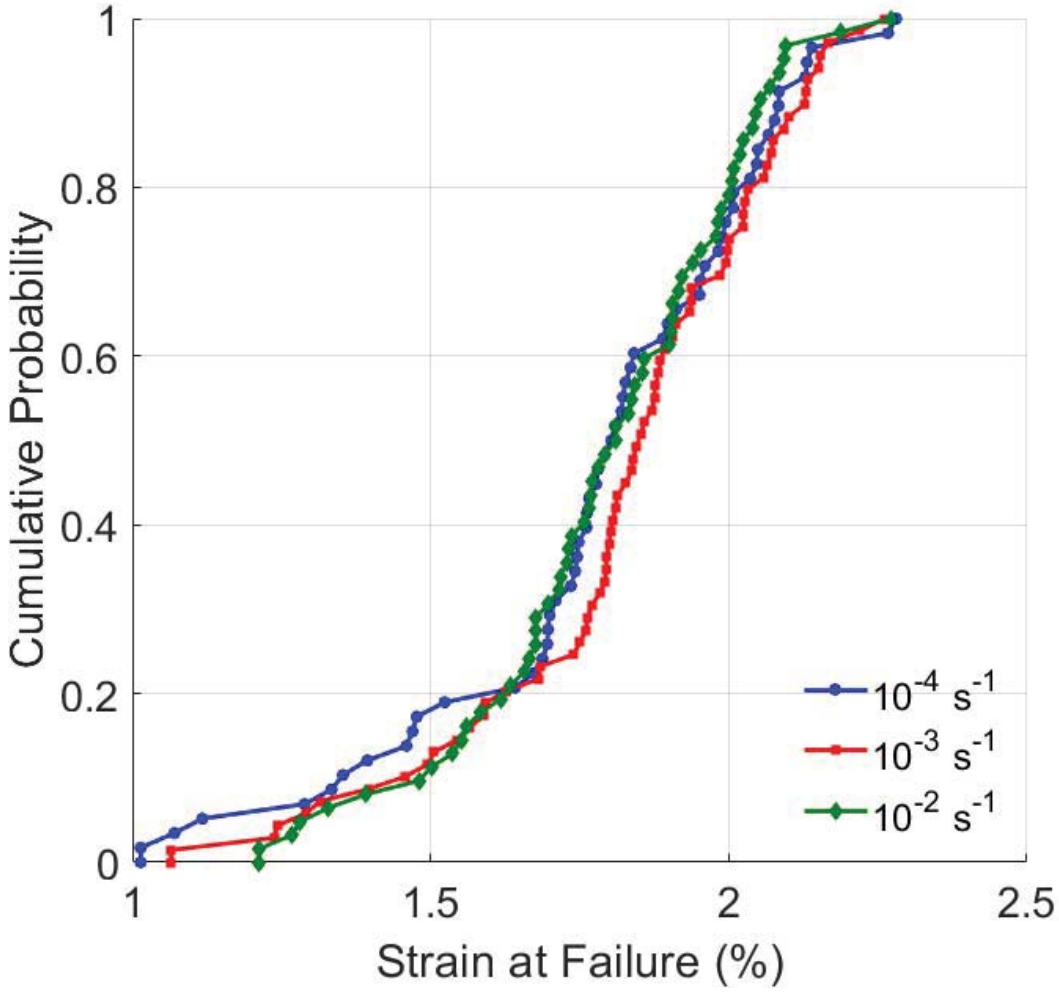

Figure 28: Empirical CDFs of strain at failure of variant strain rates

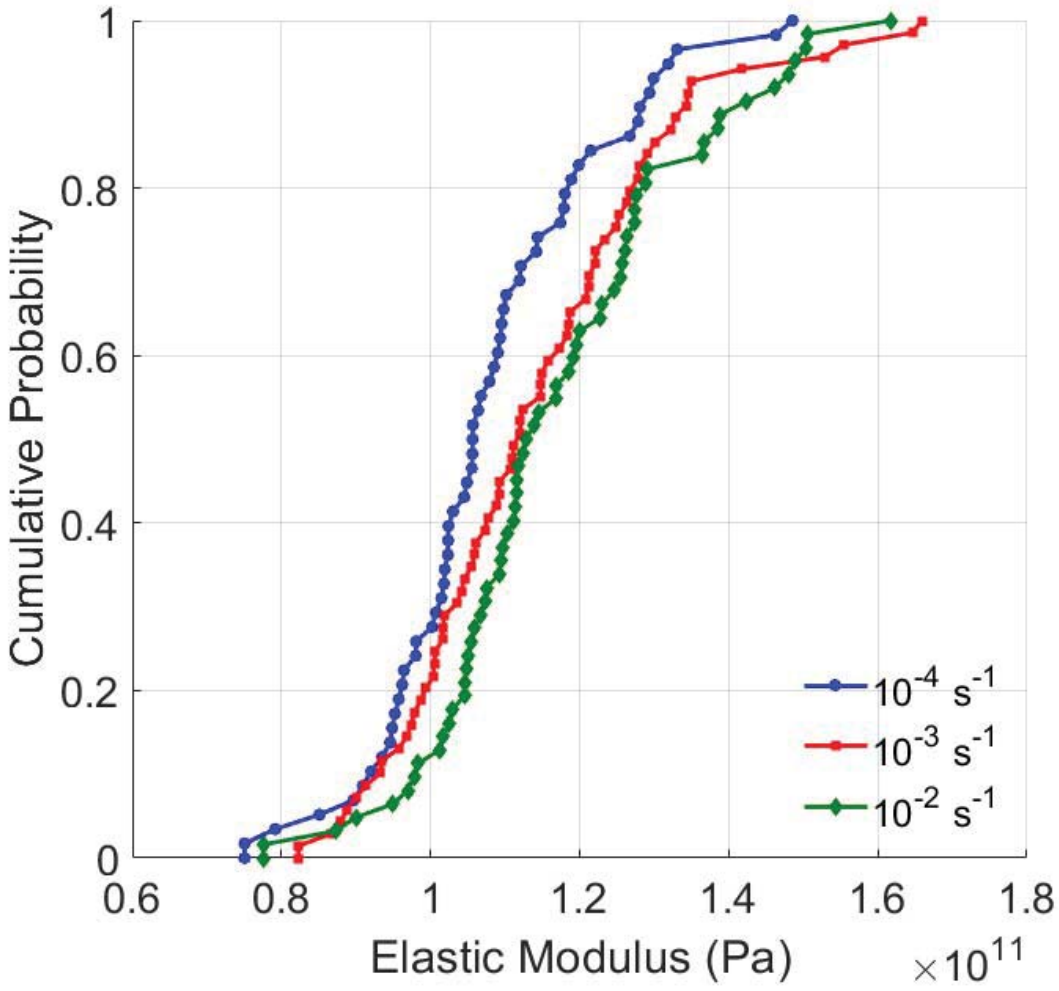

Figure 29: Empirical pdfs of elastic modulus of variant strain rates

The mean tensile strength decreases approximately 10.5% across two decades of strain rates, or 4-6% per decade. This contrasts with dry-spun yarns, which Zhang, *et al*. [67] found decrease in strength about 15% per decade. Zhang, *et al*. [67] do not report the density of their yarns but it is likely that the density is much less than the density of the fibers studied in this research given the properties of similarly produced fibers [26]. Therefore, the CNT density in fibers may play a role in the magnitude of the strain rate effect on tensile strength. As CNT fiber synthesis improves, the density of CNT fibers

will likely increase, which may lead to further decrease in the observed strain rate effects [1].

The CNT fiber failure mechanism most likely follows the theory of Zhang, *et al.* [68], who propose that the mechanism is a combination of sliding between CNTs and rupture of CNTs and bundles of CNTs which have achieved greater alignment along the fiber loading axis than surrounding CNTs and bundles of CNTs. More highly aligned CNTs carry a larger proportion of load until they fail and then the load they carried is redistributed to surrounding tubes. The overall fiber load increases, and surrounding tubes slide until another bundle of nanotubes reaches a critical degree of alignment and thus loading and fails. Increasing strain rate allows less time for tube and bundle slippage and therefore the failure mechanism will emphasize CNT rupture more heavily with increasing strain rate. The energy required to rupture covalent bonds between carbon atoms is greater than the energy required for breaking the weak intermolecular van der Waals forces between CNTs which gives rise the higher tensile strength at higher strain rates.

Results of Static Loading Testing

The static loading experiments were all conducted with the same mass of approximately 36.51$\pm$0.50 g, which corresponds to a constant, uniaxial tensile load of 35.82$\pm$0.49 cN. The static load corresponds to approximately 90.31% of the mean breaking load of the 40 mm fiber specimens tested at the moderate strain rate. Thirty-five specimens were prepared for testing by the procedure laid out in Chapter III. A total of 7

rounds of testing yielded 34 static loading tests. One fiber was accidentally broken prior to testing. 0

Three fibers failed upon load up and their time to failure was recorded as 1 second. The mean time to fiber failure was 8.45×10^3 s with a standard deviation of $1.64 \times 10^4\ s$. These values yield a CV of 194%. The CVs of tensile strength of single fibers in this research ranged between 7-11%. The small variations in diameters from fiber to fiber resulted in small differences in tensile strength and the applied stress during the static loading tests; however, those small variations in applied stress resulted in significant variations in the time to failure.

The large dispersion in time to failure is visualized in the plot of the empirical pdf of time to failure data in Figure 30. The Weibull distribution was fit to the time to failure data, the goodness-of-fit was evaluated with the KS test, and the KS test failed to reject the fit of the Weibull distribution at the 5% significance level indicating a good fit. The Weibull scale and shape parameters were $3.45 \times 10^3\ s$ and 0.46, respectively. The Coleman breaking kinetics model relates the shape parameter of time to failure data, s, from static loading tests and the shape parameter of tensile strengths, β, by Equation 2.7 which is repeated here for convenience:

$$\beta = s(\rho + 1). \tag{4.4}$$

The shape parameter obtained from tensile testing results of the nominal gage length 10 mm sample was 16.19$\pm$1.49. The $\pm$ after the reported values signify the standard deviation, SD, of the parameter estimates which was computed from the standard error, SE, and the sample size, n, by the equation:

$$SD = SE * \sqrt{n}. \tag{4.5}$$

The effective gage length of the 10 mm sample was approximately 16 mm which is the closest to the gage length of the creep specimens, 20 mm. The Weibull tensile strength shape parameter and the time to failure shape parameter values coupled with Equation 4.4 yield a value of ρ of 33.95±3.22.

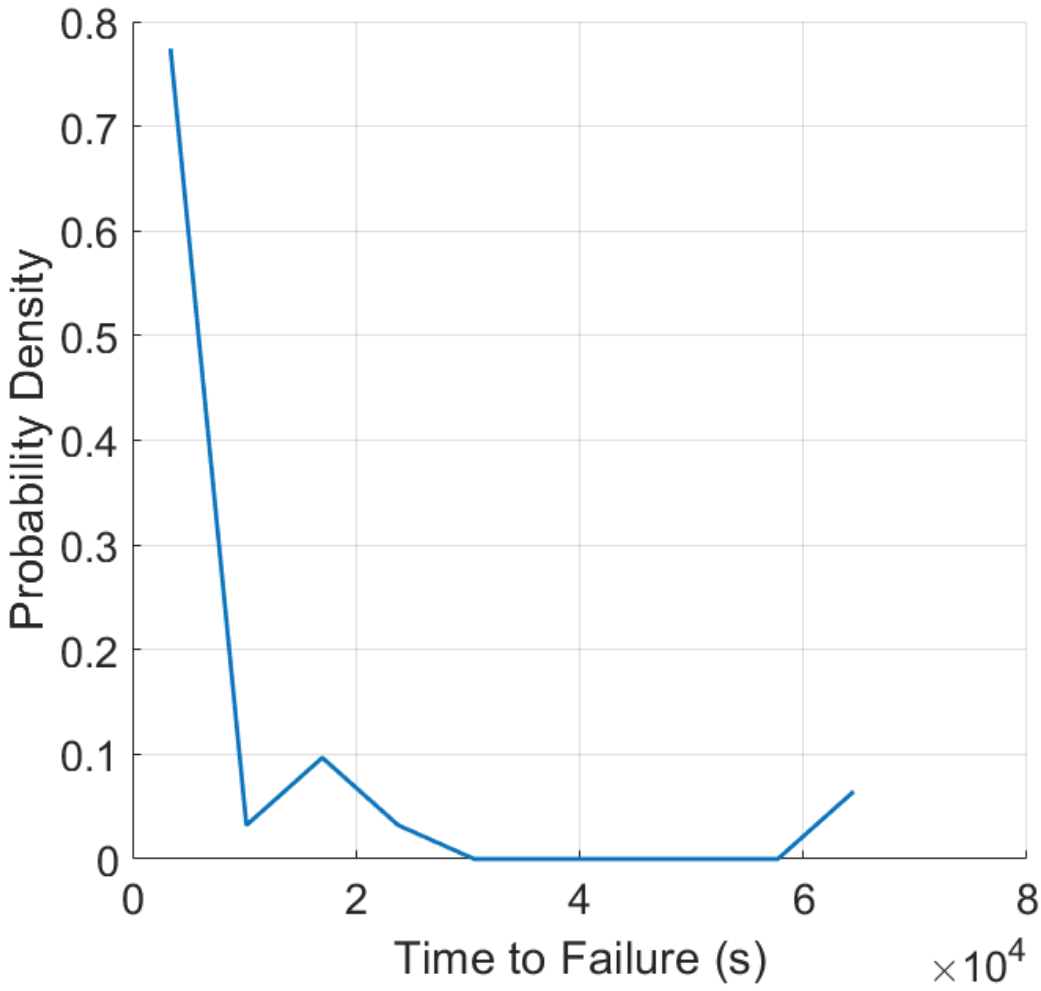

Figure 30: Empirical PDF of time to failure data for single fiber static loading tests

According to Coleman's [36] breaking kinetics model, variable strain rate tensile strength results can be used to predict ρ without accomplishing static loading testing.

This is valuable because it enables the prediction of the creep behavior of single fibers without needing to accomplish time and equipment intensive testing.

Wagner, *et al.* [69] and Schwartz, *et al.* [49] worked with the power-law form of Coleman's [36] model to study the loading rate dependent behavior of Kevlar and polyethylene fibers, respectively. They showed that the scale parameter, α, from the Weibull distribution fit to tensile strength data is related to the rate of applied stress, R, by the relationship

$$\alpha = \left[R(\rho+1)\left(\gamma^{-1}\mu^{-\frac{1}{s}}\right)\right]^{\frac{1}{\rho+1}} \tag{4.6}$$

where ρ, γ, μ, and s are positive constants. This relationship shows that $\ln \alpha \; vs. \ln R$ will have a slope of $1/(\rho+1)$. The strain rate data, discussed in the previous section, was used to calculate ρ based upon the slope of the plot of $\ln \alpha \; vs. \ln R$. A semilogarithmic plot of the data is shown in Figure 31. The $\ln \alpha \; vs. \ln R$ relationship yielded a value of 34.85 ± 0.77 for ρ corresponding to the slope between the smallest and moderate strain rate samples. The slope between the moderate and highest strain rate samples yielded 54.02 ± 1.21 for ρ.

The similarity in ρ values obtained between the slower strain rate tensile tests and the static loading tests suggests that the Coleman [36] model may be valid for relating the statistical distributions of tensile test and static loading results. This behavior is likely a further extension of the implications of the variable strain rate tensile testing results. The stress-strain behavior was shown to be very similar in character despite a change in strain rate. The same mechanism which governed failure under tensile testing is likely governing the failure of the CNT fibers under the static loading condition.

The discrepancy of a higher value for ρ due to the slope between the moderate and high strain rate may be explained by a changing dependence of tensile strength on the strain rate occurring at higher strain rates. Zhang, *et al.* [67] did not provide sufficient detail in their research on the strain rate behavior of CNT fibers to determine a change in the behavior of dry-spun CNT fibers, but Schwartz, *et al.* [49] provide helpful information from their strain rate study of ultra-high strength polyethylene fibers (UHSPE). The molecules in UHSPE fibers and CNTs are held together by van der Waals forces, so the two fibers will share some similarities in their response to changing strain rate. Schwartz, *et al.* [49] discovered that increasing strain rate from approximately $10^{-3} - 10^{-2}\ s^{-1}$ caused the value of ρ to double for UHSPE fibers, lending credence to a real change in ρ in these CNT fibers. This result also implies that as strain rates are increased above $10^{-2}\ s^{-1}$, the strength increases observed will be very small. Also, the large value of ρ at higher strain rates lends further evidence that breakage of covalent bonds between carbon atoms plays a larger role in determining strength in that regime, with a smaller contribution from weaker intermolecular van der Waals forces.

Microstructural analysis was conducted on tensile tested and statically loaded specimens to look for evidence supporting the hypothesis presented here on the fiber failure mechanism.

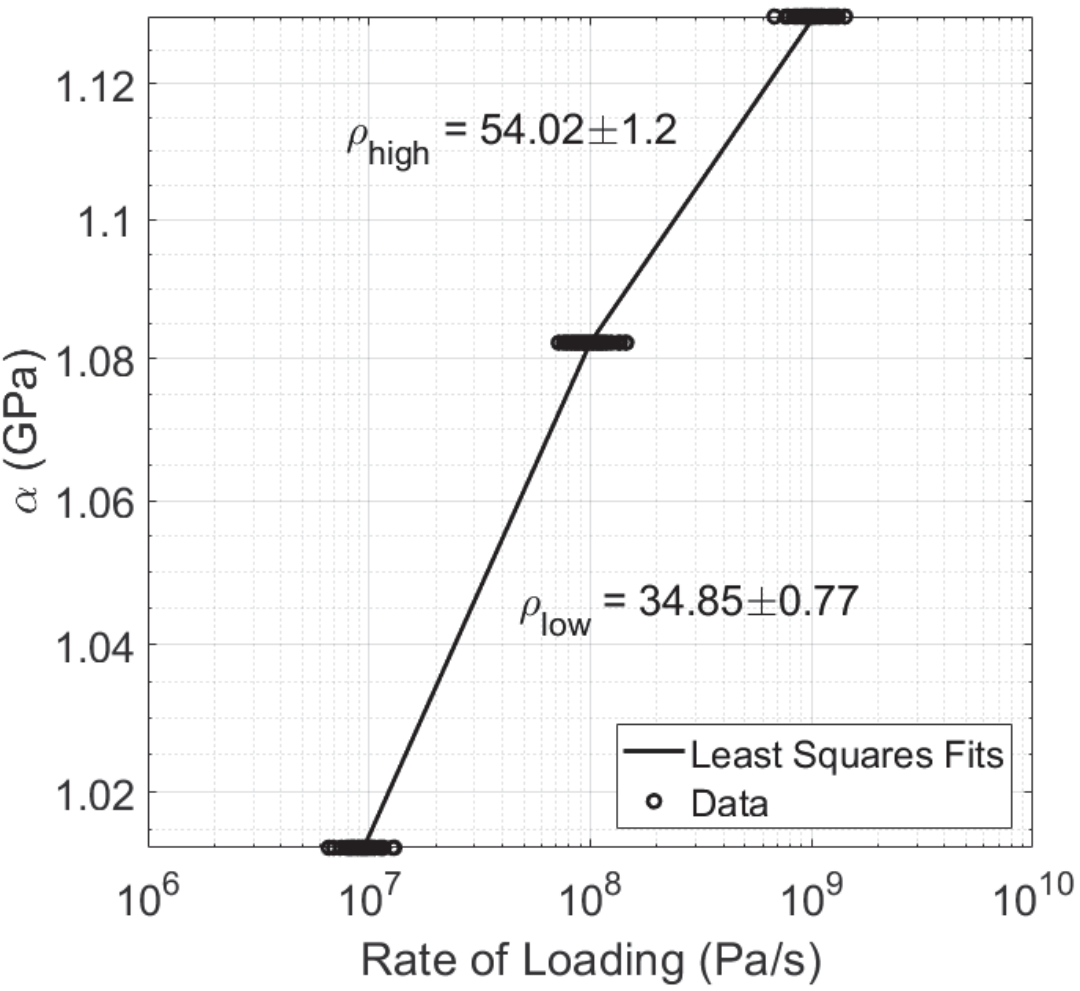

Figure 31: Weibull scale parameter versus the rate of loading from tensile testing results

Analysis of FIB Milled Mechanically Tested Fibers

A creep specimen was chosen for further microstructural examination by FIB milling. The creep specimen survived for 5940 seconds, or 1.65 hours, before catastrophic failure. Three FIB cuts were made along the length of the creep specimen. The first milling location was approximately one millimeter from the tip of the fiber fracture and the successive two cuts were made at one millimeter increments from the first cut. Figure 32 shows the fiber chosen for analysis. The opposing fracture surface

which was not cut for this analysis is shown in Figure 33. The small cut out on the left upper side of the fiber is the first FIB milling location.

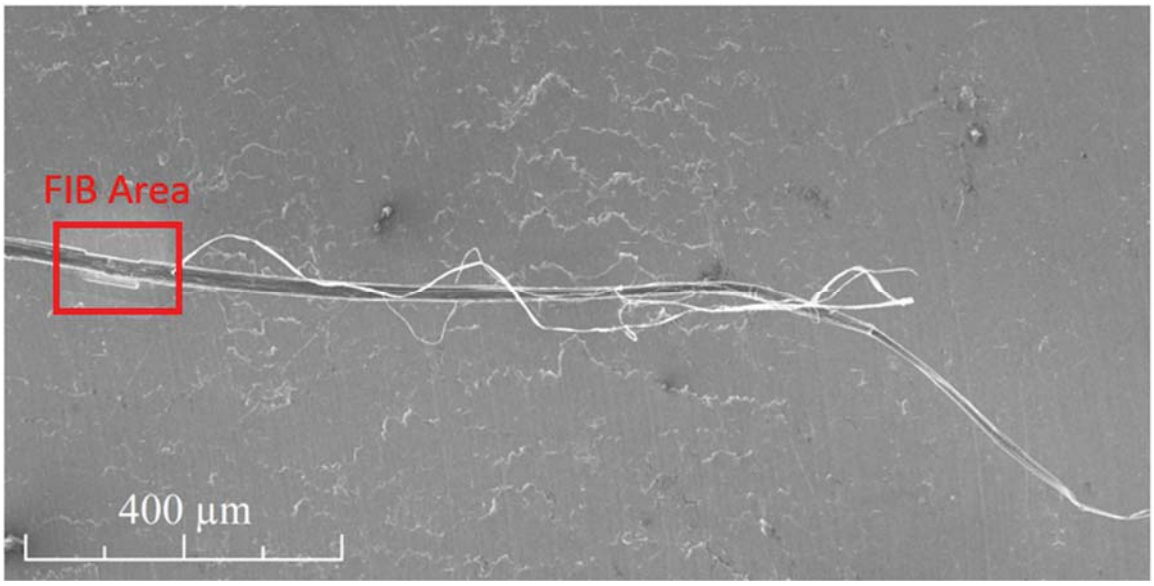

Figure 32: Moderate life creep specimen used for FIB microstructural analysis

Examining the external surface of the fiber shows a relatively smooth surface. The fiber is thinner approaching the fracture surface tip which indicates the expected failure mechanism of thinning fibrils by nanotube slippage until the fibril reaches a critical stress and fractures by tube rupture. Figure 34 shows the smooth surface of the opposing fracture surface due to the creep rupture of the fiber.

The fiber was approximately 20 µm in diameter. The three FIB cuts were made approximately 5 µm deep into the fiber thickness. The milled surface was cleaned up with low beam current passes and then imaged by SEM. The fibers were milled a second time at the same locations another 5 µm in thickness. After clean up, the second set of surfaces were imaged by SEM. The fibers were milled twice to show the extent of the observed damage. The observed damage in the images is widespread and not limited to

the small cross-sections examined. The FIB cuts were made along the length of the fiber rather than laterally to show how extensive the damage was.

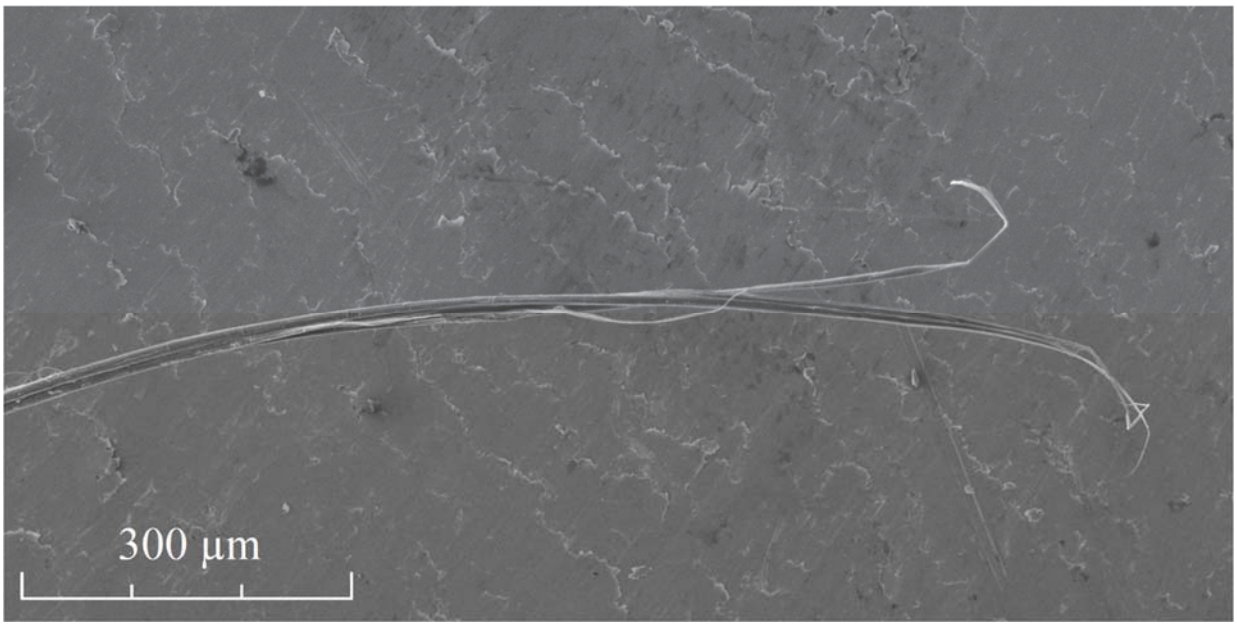

Figure 33: Opposing fracture surface of long-life static loading specimen

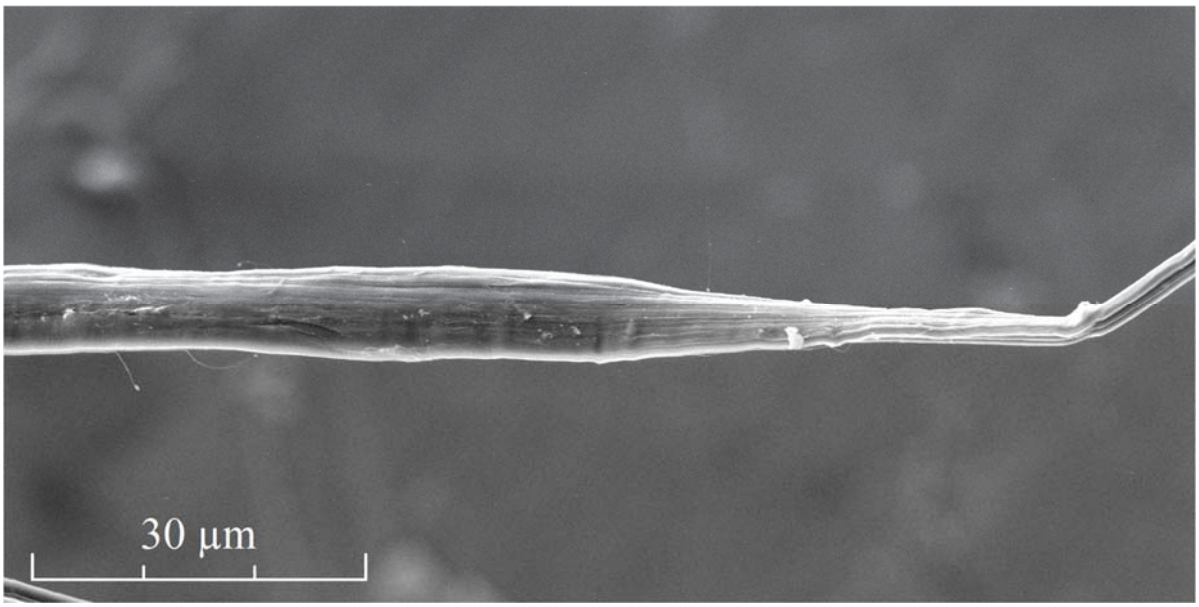

Figure 34: Closer image of upper fracture tip of Figure 33

The following FIB cut fiber images are arranged in order of their distance from the fracture tip. Figure 35 shows the FIB surface closest to the fracture tip. Large cracks are visible in the microstructure and appear everywhere in the exposed surface. The exposed surface is approximately 50 μm wide. Visible cracks appear to span the entire length of the exposed surface. These cracks show how small cracks and voids, visible in the images of unstressed fibers, create much larger cracks when exposed to tensile stress.

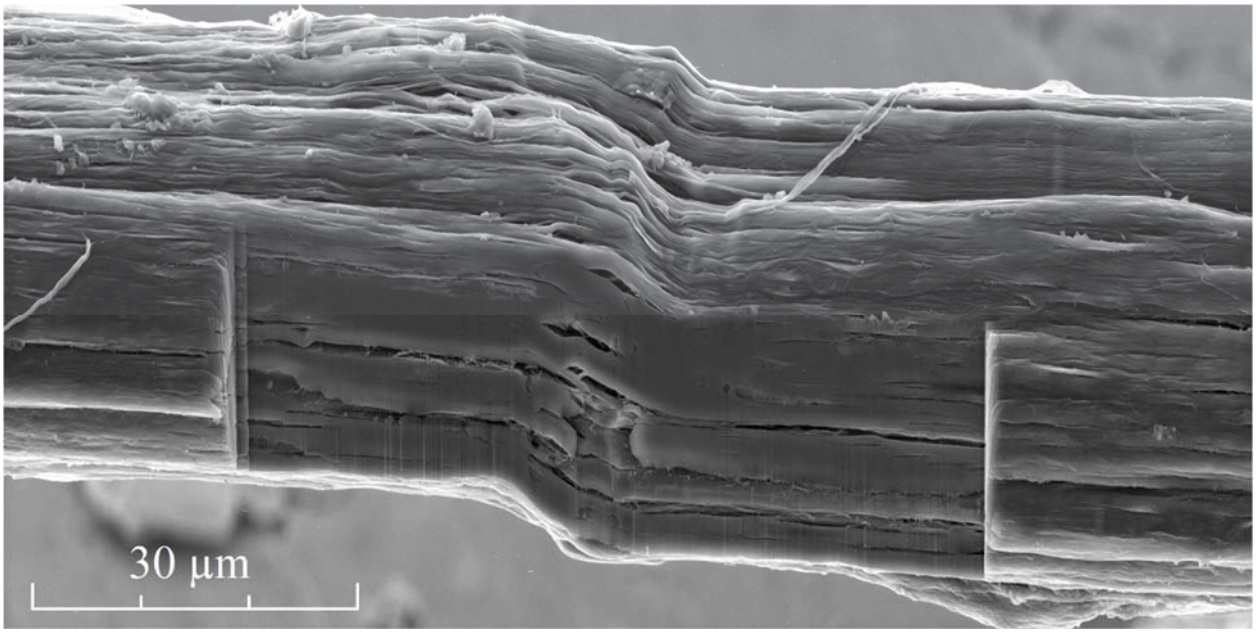

Figure 35: FIB surface approximately 1 mm from the fracture tip

The second image, Figure 36, is approximately 1 mm from the previous image. There appear to be long cracks which span the entire exposed surface. The cracks do not appear everywhere in the exposed microstructure. The top half of the surface appears completely free of cracks. The final image, Figure 37, shows the farthest FIB cut surface. There is only one large crack which is similar in size to cracks observed in unstressed fibers. These final two images appear to show that internal crack development is

somewhat based upon location with respect to the fracture surface. Internal cracking is more highly developed nearer to the crack tip. The distance with which crack development is observed with respect to the fracture tip is significant. Cracks are observed to be opening further than 2 millimeters from the initial fracture tip. Cracks at 3 mm away however appear to be unaffected. The cracks observed in Figure 37 may have developed from much smaller voids which clouds the understanding of how large a factor length from the fracture tip plays in the development of cracks.

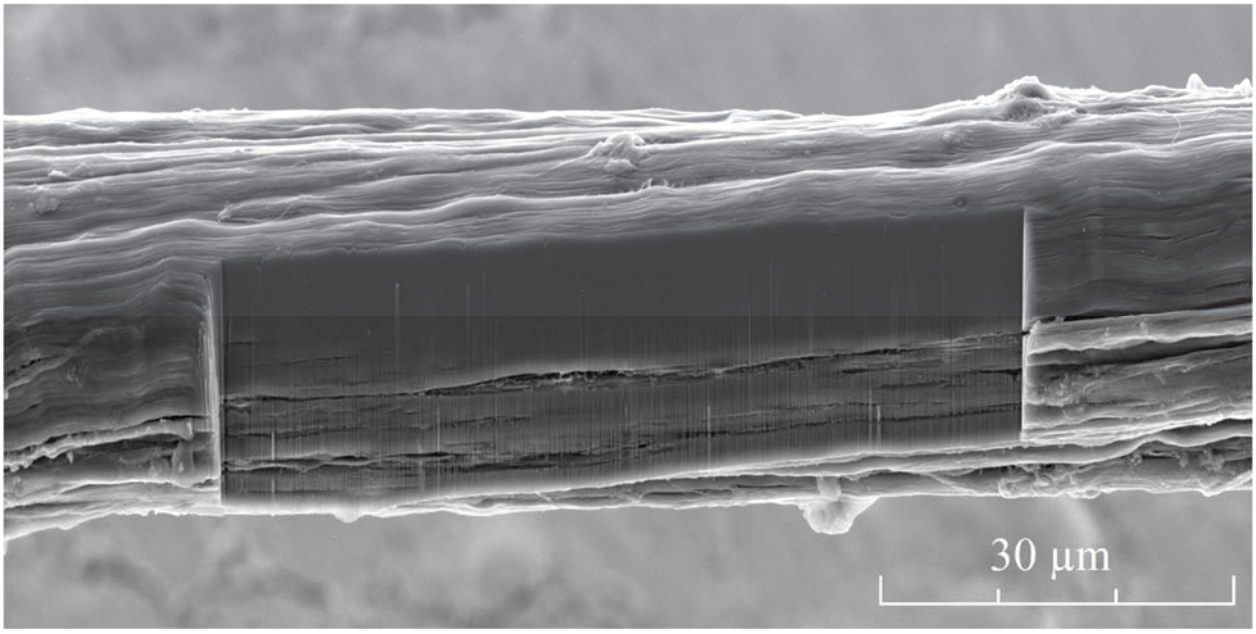

Figure 36: FIB surface approximately 2 mm from the fracture tip

The second set of FIB surface images help to develop the understanding of the crack development process. The second pass milled away an additional 5 µm of depth into the fiber surface. The same cracks appear in both the first and second pass surfaces. The extent of growth appears to be the same in both sets of images as well. This indicates

the cracks not only extend lengthwise along the fiber, but also radially outwards towards the outer surface of the fiber.

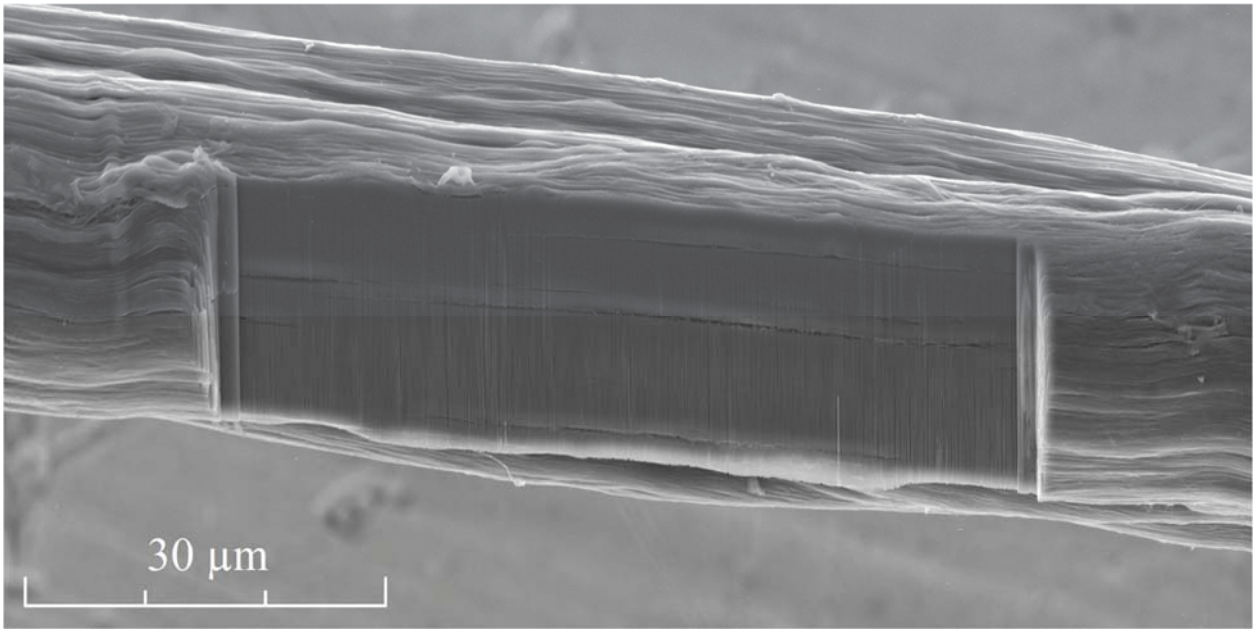

Figure 37: FIB surface approximately 3 mm from the fracture tip

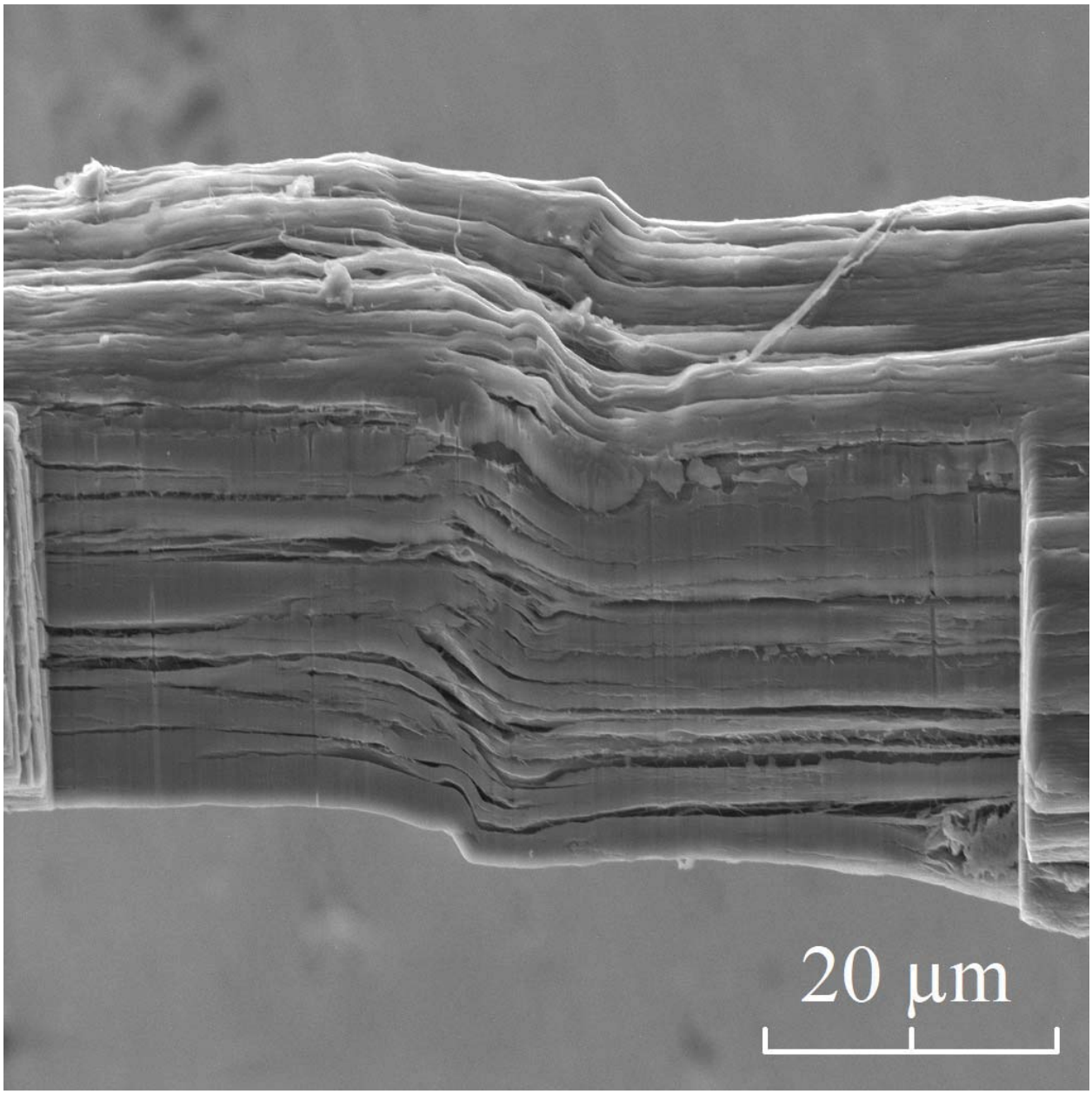

Figure 38: FIB surface 1 mm from fracture tip, second pass

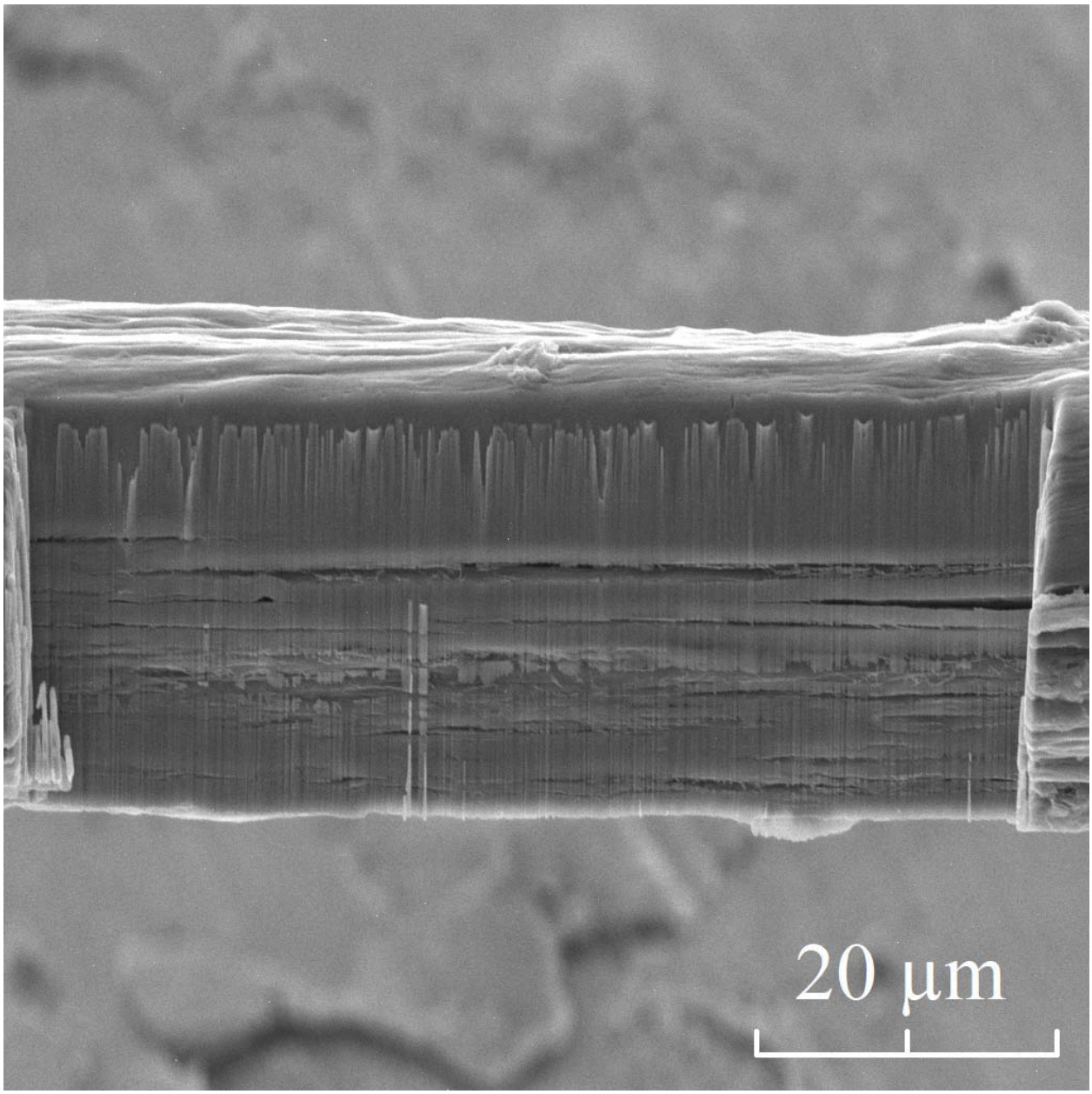

Figure 39: FIB surface 2 mm from fracture tip, second pass

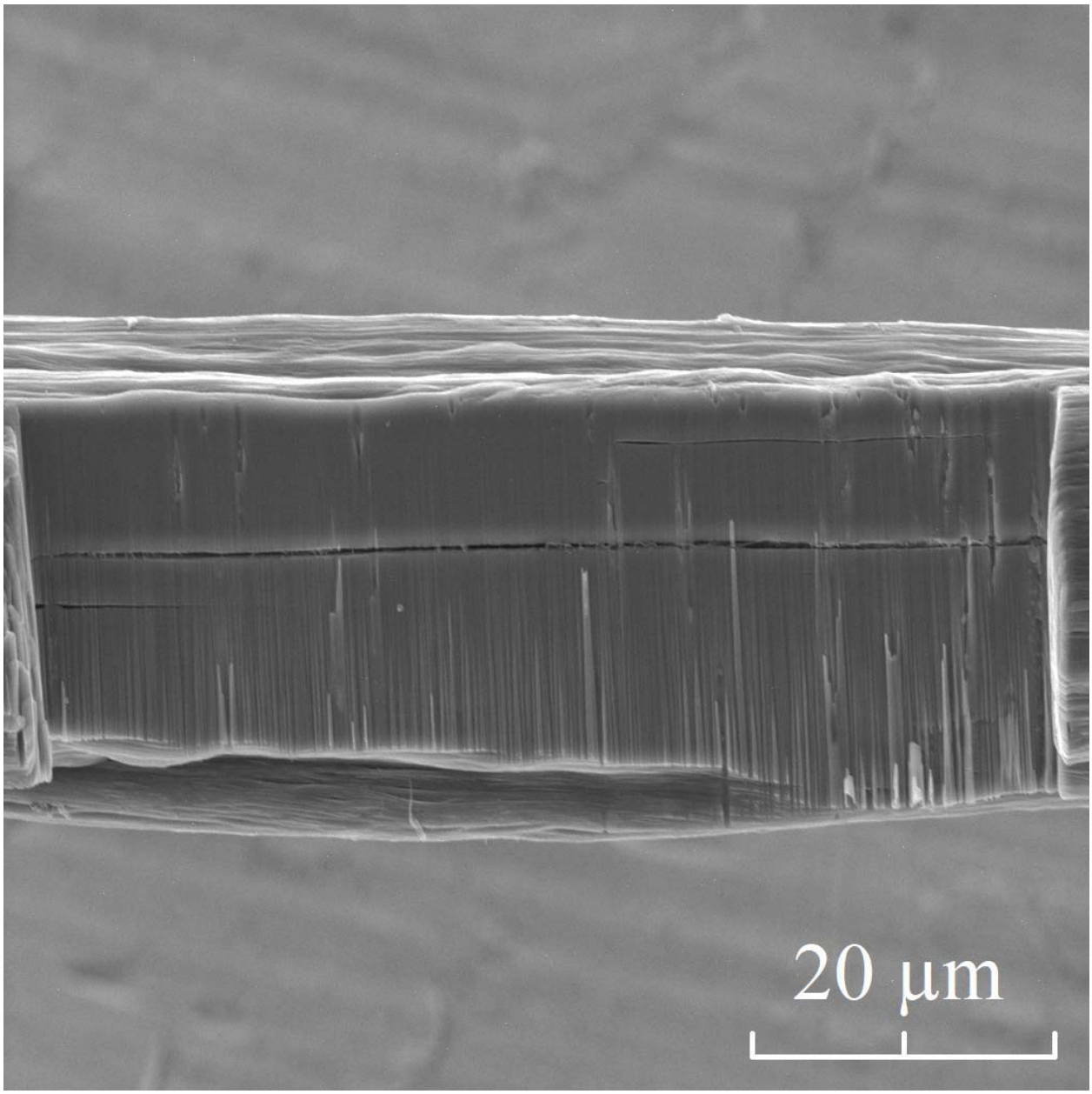

Figure 40: FIB surface 3 mm from fracture surface, second pass

A fiber which was tensile tested at the highest elongation rate of $10^{-2}\ s^{-1}$ was also examined by FIB milling. A single location was milled approximately 1 mm from the tip of the fractured fiber. The revealed microstructure appeared similar to the surfaces exposed on the creep specimen and so secondary and tertiary cuts further from the

fracture tip were foregone. The image of the first pass, Figure 41, shows minimal cracking to an extent which was observed in some unstressed fibers. The second pass, Figure 42, showed larger cracking, but not as long and connected as in the creep tested specimen. These images indicate that the high elongation rate does not allow sufficient time for cross-sections of the fiber further from the failure cross-section to develop voids and existing cracks into longer and wider cracks.

The observed phenomenon may indicate that the cross-section where failure occurs, the failure mechanism proceeds the same way as at other testing speeds. Pre-existing voids or a smaller cross section due may result in a lower stress needed to open the voids to a critical size for failure. The small cross-section scenario would result in a higher stress observed in that cross-section relative to the other locations along the fiber. Voids in that small cross-section would develop more quickly into critical sized cracks and result in failure. Both scenarios are plausible, and it is difficult if not impossible to narrow down the exact cause without extensive tedious in-situ non-destructive measurements of fiber cross-sections and voids sizes prior to and during mechanical testing.

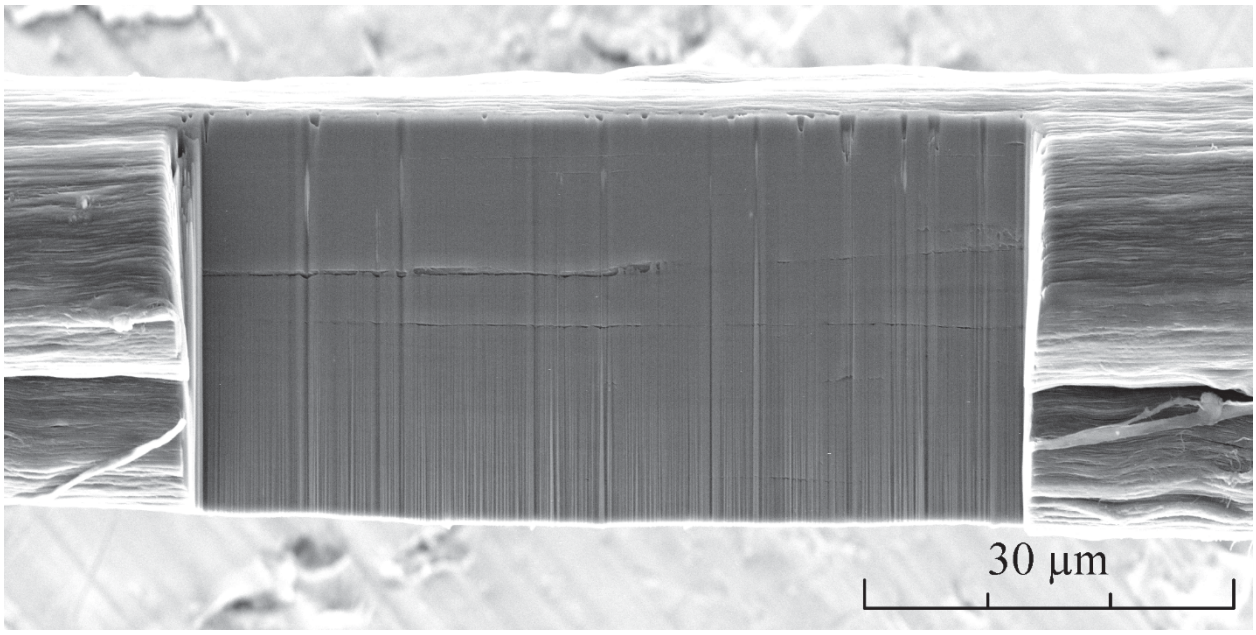

Figure 41: FIB surface of tensile test specimen 1 mm from failure tip, first pass

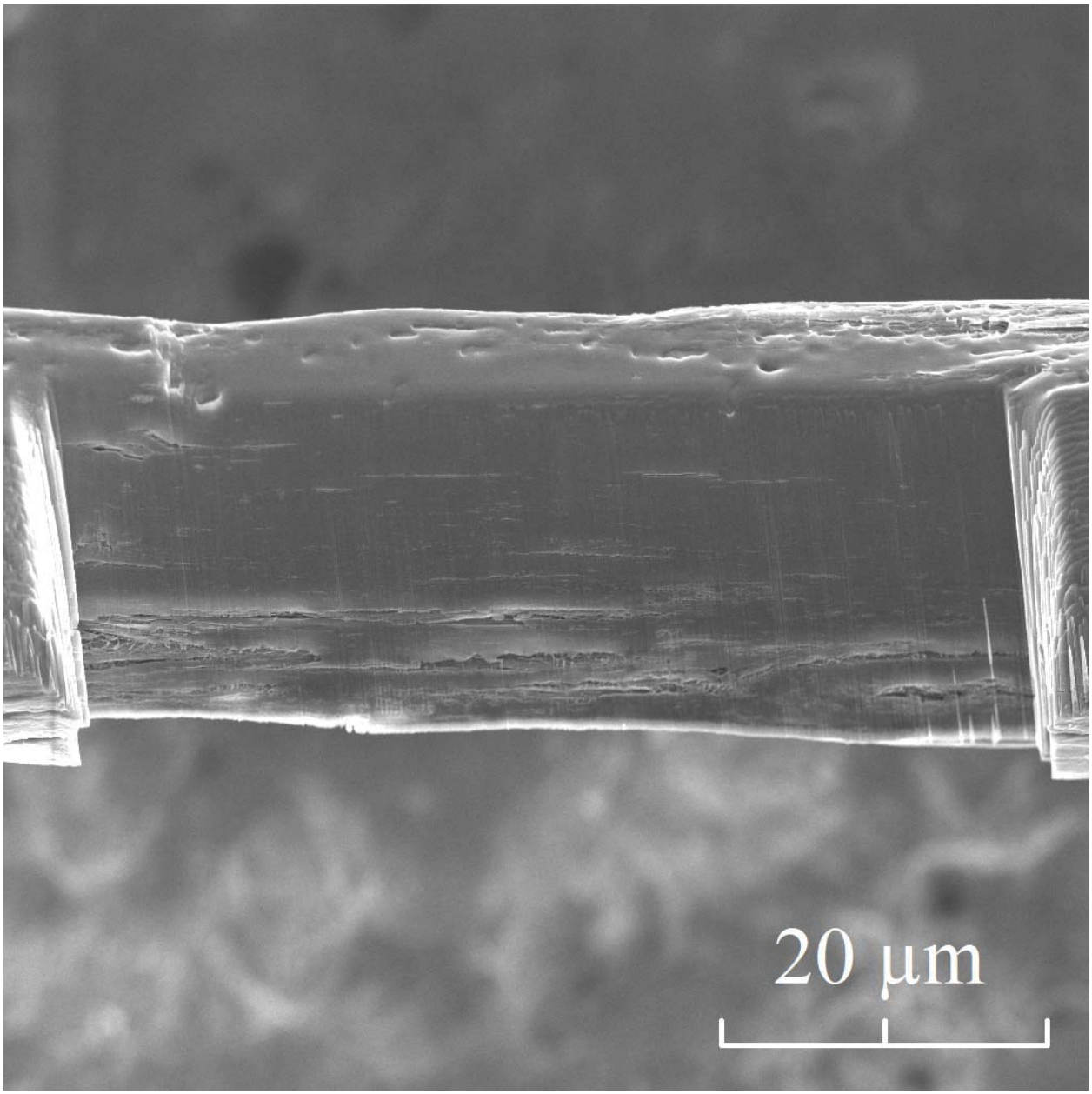

Figure 42: FIB surface of tensile test specimen 1 mm from failure tip, second pass

Results of AO and UV Exposure Characterization

This section discusses the results of the mechanical, electrical, electromechanical, and microstructural analyses. The mechanical analysis was conducted by tensile testing

pristine, AO, and UV exposed CNT yarn specimens. The electrical and electromechanical analyses were integrated into the tensile testing with in-situ electrical measurements of the CNT yarn resistance. Microstructural analysis was conducted by Raman spectroscopy and SEM analysis of the pristine and exposed CNT yarns.

Results of Mechanical Characterization

The pristine, AO and UV exposed fibers were mechanically tested by uniaxial tension until failure. A total of 5 pristine specimens, 6 AO specimens, and 7 UV specimens were tested. The tensile strength, strain at failure, and elastic modulus of all samples are reported in Table 5 and comparative plots of the stress-strain diagrams are included in Figure 43 and Figure 44. Summarized results in Table 5 and subsequent result summary tables include the mean, the standard deviation (SD) and the CV for each reported measure.

The UV exposure resulted in a 1% increase in the tensile strength of the yarn and a 17.4% increase in the strain at failure. The KS test was used to test whether the pristine and UV tensile strengths were drawn from the same continuous distribution. The KS test failed to reject the null hypothesis at the 5% significance level, which lends statistical evidence to the hypothesis that the observed increase in tensile strength was due to statistical variation.

The AO exposure had a significant deleterious effect, causing a 63.9% decrease in the yarn tensile strength and 56.3% decrease in the strain at failure. The AO exposure results show a more dramatic degradation of the tensile strength than the decrease of 25% that Hopkins, *et al.* [11] observed with dry-spun CNT yarns directly exposed to the LEO space environment. The difference may be due to the proprietary post-processing

techniques used on their yarns or the multi-wall character of the CNTs assembled to create those yarns. The CNT yarns tested by Misak, *et al.* [59] and Hopkins, *et al.* [11] had significantly larger diameters and given that only the surface of the yarn is exposed, the detrimental effects can be expected to be less severe in comparison to the much smaller CNT yarns exposed in this research.

The elastic moduli were calculated from the slope of the initial linear region of each stress-strain curve. The average elastic moduli values were 24.69, 17.87, and 20.52 GPa for the unexposed, AO, and UV exposed specimens, respectively. In Figure 43 and Figure 44, the difference in elastic moduli values is apparent by comparing the two groupings of stress-strain curves. The decrease in moduli of the AO specimens was attributed to increased, localized yielding because of the pits observed in the microstructural analysis, in the concluding section of this chapter. The unexposed and UV stress-strain curves (Figure 44) show very similar mechanical behavior of these two specimen types in their maximum stress, but the lower elastic moduli of the UV exposed samples contributes to the greater strain at failure of the UV specimens as compared to the unexposed specimens. This difference may be explained by the generation of amorphous carbon on the yarn surface which acts as a lubricant, allowing the fibers in the yarn to more easily slide past each another. This theory is explored further in the Raman spectroscopy results.

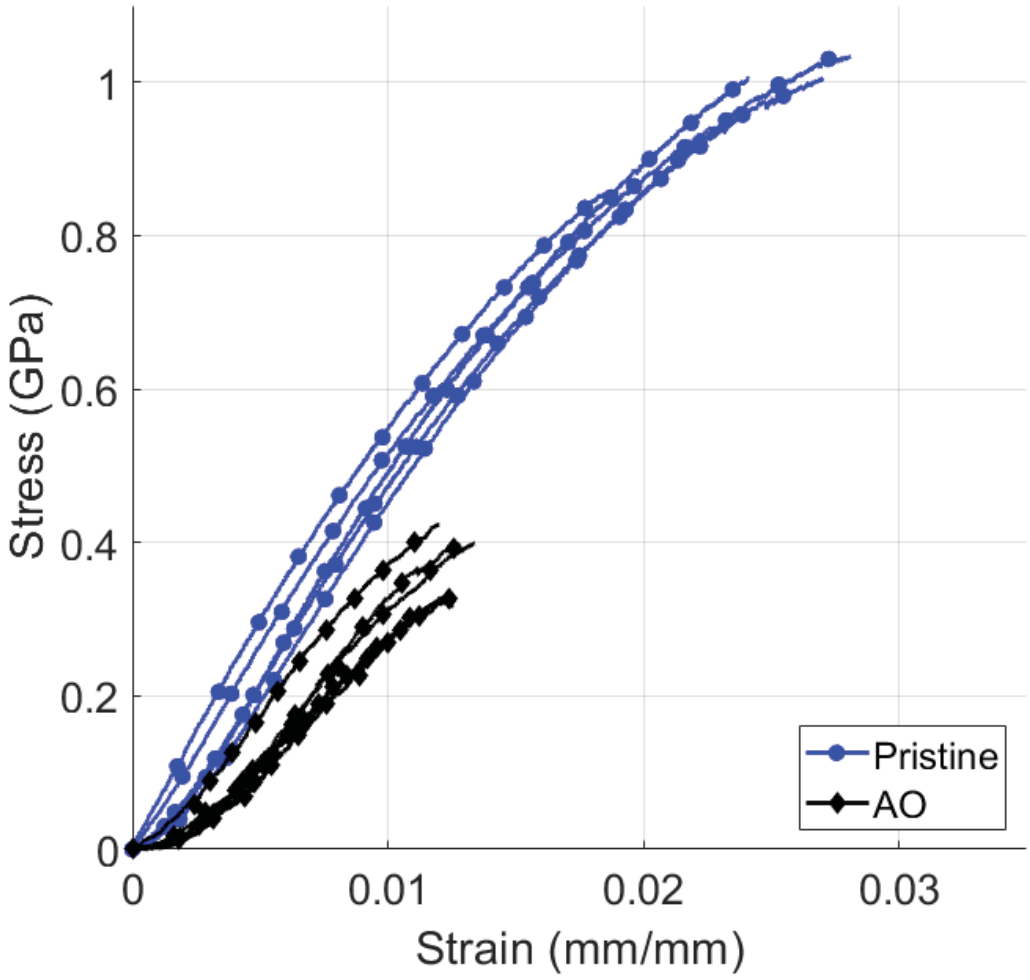

Figure 43: Stress-Strain Curve of Unexposed and AO Exposed Specimens

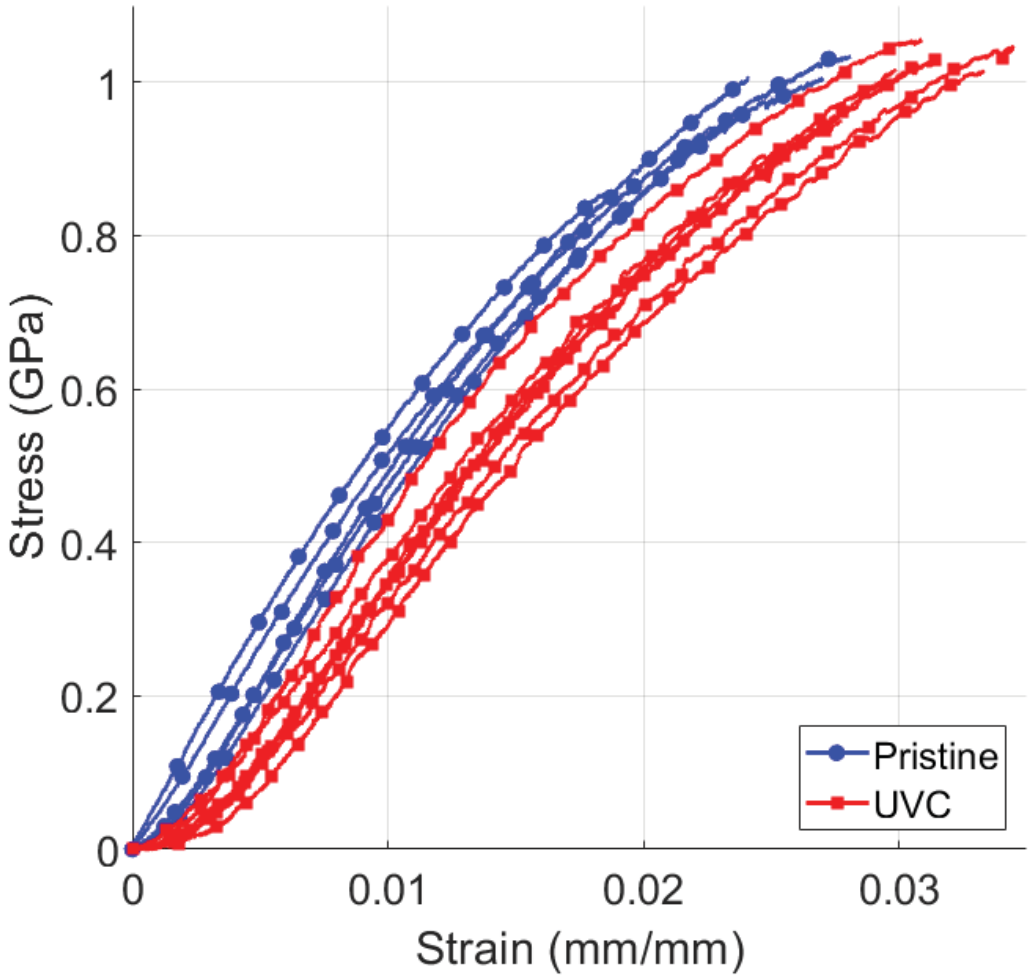

Figure 44: Stress-Strain Curve of UV Exposed and Unexposed Specimens

Table 5: Summary of Mechanical Properties of Pristine, AO, and UV Exposed Yarns

Specimen Type	Property	Mean	SD	CV (%)
Pristine	Tensile Strength (GPa)	1004	32.90	3.28
	ε_F (10^{-2})	2.52	0.29	11.62
	E (GPa)	24.69	9.89	40.06
Ultraviolet	Tensile Strength (GPa)	1015	34.82	3.43
	ε_F (10^{-2})	2.96	0.19	6.57
	E (GPa)	20.52	5.59	27.24
Atomic Oxygen	Tensile Strength (GPa)	366.51	45.21	12.33
	ε_F (10^{-2})	1.24	0.058	4.69
	E (GPa)	17.87	4.91	27.48

Results of Electrical Characterization

The electrical conductivities of the pristine, AO, and UV exposed specimens were 2.45±0.12, 1.91±0.07, and 2.45±0.021 MS/m, respectively. These measurements reflect a 22.04% decrease in conductivity of the AO exposed specimens and no significant change in the conductivity of UV exposed specimens.

It was expected that the application of vacuum pressure and elevated temperature due to the UV lights would cause a decrease in the electrical conductivity of the UV exposed yarns because of the diffusion of acid dopants from the fiber. The acid dopant is a leftover from the fiber spinning process and increases the electrical conductivity of the

yarns significantly. The expected drop due to acid diffusion may have occurred, but a competing mechanism may have increased the electrical conductivity. The yarns were held under tension during the duration of the UV exposure. As the fiber diffused, the fibers may have become more densely packed and aligned as the leftover acid molecules left the fibers. Greater fiber alignment and density are positively correlated with electrical conductivity so this may explain the apparent lack of change.

Microstructural analysis shows portions of the individual AO exposed filaments have been heavily eroded by the AO flux resulting in a reduced effective cross-sectional area for electron transport. The AO induced decrease in conductivity of 22.04% is very similar to results obtained in the work of Hopkins, *et al.* [11], who recorded conductivity decreases of 28.5% and 26.1% for LEO exposed specimens on two different exposure locations on the International Space Station. The operators of the AO flux utilized in this research estimate the exposure is equivalent to a year onboard the International Space Station, whereas, Hopkins' specimens experienced over two years of direct space exposure. The apparent discrepancy is likely due to the significant difference in yarn diameter between their work and this research.

The standard deviation of the conductivity of the UV exposed specimens is significantly less than the pristine specimens. This phenomenon may be due to reduced acid dopant content as well as improved packing and alignment of the CNTs in the yarn microstructure. The unchanged electrical conductivity and the significant decrease in standard deviation of the electrical conductivity of the UV exposed specimens warrant further investigation.

Table 6: Summary of Conductivity Results of Pristine, AO, and UV Exposed Yarns

Specimen	Mean Conductivity (MS/m)	SD (MS/m)	CV (%)
Pristine	2.45	0.12	5.12
Ultraviolet	2.45	0.021	0.87
Atomic Oxygen	1.91	0.07	3.66

Results of Electromechanical Characterization

Determination of GF values by Equation 3.27 was carried out to investigate whether the AO and UV exposures resulted in a change to the piezoresistive effect in the CNT yarns. The GF measurements were carried out during the tensile testing by making in-situ measurements of resistance of the CNT yarns by the four-probe method described in Chapter III.

The GF values of the CNT yarns tested in this research were calculated by utilizing the change in resistance and strain measured just prior to yarn failure. These GFs were averaged for all specimens of each exposure type. The pristine and AO exposed specimens exhibited similar GF values which indicates very little change occurred to the piezoresistive character of the yarns due to the AO exposure. The average GF of the UV exposed yarns was 7.98, which is a 247% increase over the average pristine yarn GF of 2.30. This dramatic increase requires a much more thorough and focused study to explore

why the UV exposure would lead to this result, but only small changes to the tensile strength and electrical conductivity of the yarn.

Miko, *et al.* [70] observed that very high intensity UV radiation did not damage the individual CNTs studied in their work. Their observation supports the tensile strength results described herein, which suggest the UV radiation does not weaken the CNT yarn micro- or macrostructures. The change in piezoresistive effect may be caused by the diffusion of chlorosulfonic acid from the CNT filaments, which is aided by the application of vacuum pressure and elevated temperature which were both present during the vacuum UV exposure. Chlorosulfonic acid strongly p-dopes CNT fibers resulting in increased electrical conductivity [71].

The chirality of SWNTs dictates their metallic or semiconducting character as well as their piezoresistive response, with zig-zag CNTs exhibiting the largest GFs and armchair CNTs with no GF contribution [72]. The dopant may suppress the GF contribution of the highest GF CNT chiralities, thereby lowering the overall GF of the CNT yarn network. So even removing a small amount of the acid dopant reduces the GF suppressing behavior and allows the high GF SWNTs to contribute more significantly to the piezoresistive effect, thereby increasing the yarn GF.

Table 7: Summary of Piezoresistance Results of Pristine, AO, and UV Exposed Yarns

Specimen	Mean Gauge Factor	SD	CV (%)
Pristine	2.30	0.15	6.48
Ultraviolet	7.98	0.38	4.82
Atomic Oxygen	2.99	1.04	34.82

Results of Raman Spectroscopy

Fifty Raman spectra each were collected at different points on pristine, AO, and UV exposed yarn sections. Each collected spectrum consisted of 1024 intensity values corresponding to the Raman shift wavenumbers of the scattered light along the collected spectrum. Data analysis proceeded by first finding the intensity noise floor of each spectrum and subtracting it from the list of intensity values. Then, each list of intensity values was normalized by dividing by the maximum intensity value of the spectrum, found at the G peak located around Raman shift wavenumber 1585 cm^{-1}. The normalized intensity of the D peak, which is the peak nearest 1350 cm^{-1}, is the D/G ratio. Normalizing each collection by the height of the G peak was necessary for comparison of data between collections and exposure types as the intensity of each spectrum may differ because of differences in beam focus or geometry differences between collections.

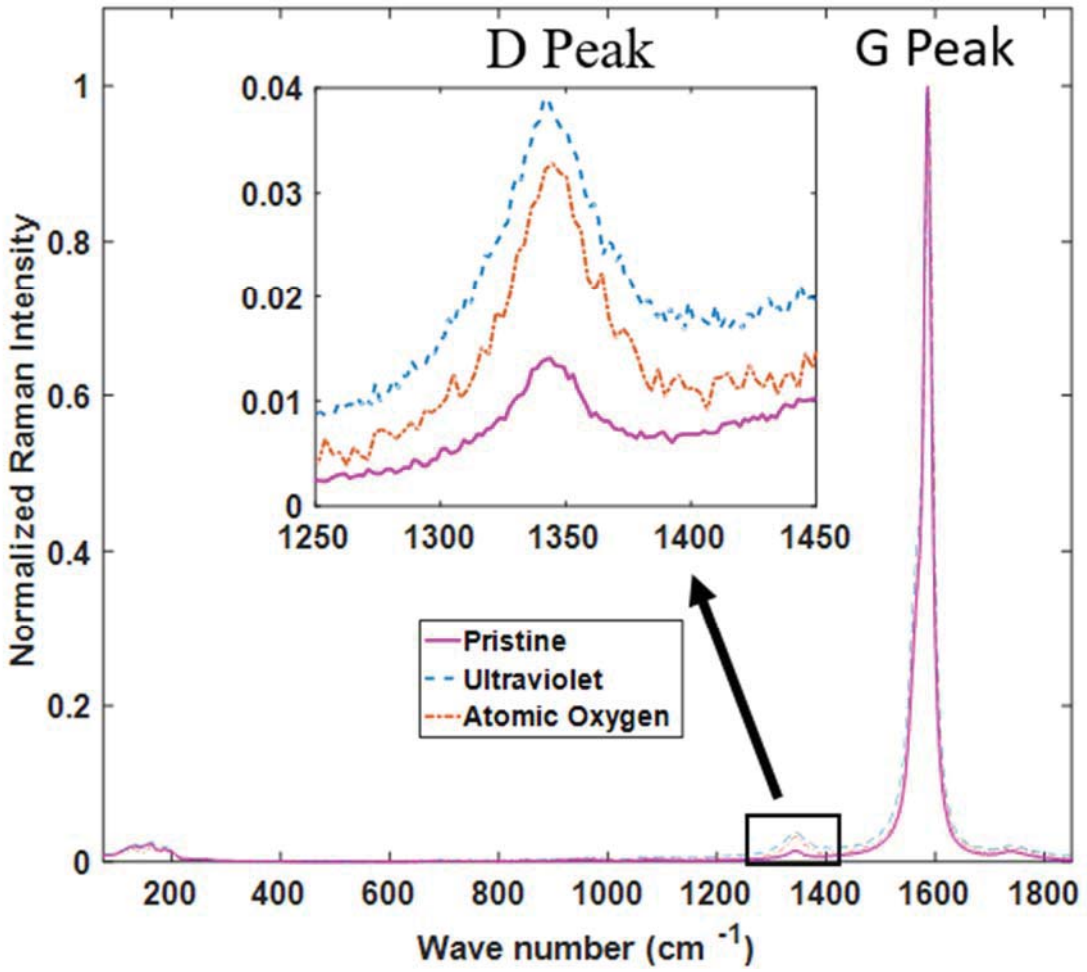

Figure 45: Representative Plots of Mean Raman Spectroscopy Results

The results of the analysis are summarized in Table 8 and Figure 45. The D/G ratio increased for both exposure types with UV light exposed specimens exhibiting the highest D/G ratio. Higher D/G ratios indicate more CNT molecular structure disorder. The increase in disorder in the AO exposed specimens is a result of erosion of carbon by monoatomic oxygen. The increase in disorder corresponding to the increase in D/G ratio observed in the UV exposed yarns are unexpected because of the observations of Miko, *et al.* [70] who observed no damage to CNTs from high intensity UV radiation.

The UV light does not penetrate deeply into the yarn surface and so the recorded damage may only affect the outer surface which was given a long time to develop during the 1000-hour UV exposure. Another explanation may be that as the acid dopant diffused through the yarn surface the microstructure was disturbed and became less aligned along the fiber longitudinal axis, which would result in an increased measure of disorder in the microstructure and a correspondingly larger D peak intensity. The lack of significant change to the tensile strength of the UV exposed specimens seems to suggest that the bulk properties of the yarn were unaffected by the light, which supports both hypotheses.

Table 8: Summary of Raman Spectroscopy of Pristine, AO, and UV Exposed Yarns

Specimen	Mean D/G Ratio (10^{-2})	SD (10^{-2})	CV (%)
Pristine	1.35	0.29	21.48
Ultraviolet	3.80	0.79	20.79
Atomic Oxygen	3.34	0.80	23.95

Results of Microstructural Characterization of AO and UV Exposed Yarns

The AO and UV exposed yarn sections were examined by SEM to investigate the microstructural effects of the exposures. The pristine and UV exposed yarn surfaces were almost indistinguishable apart from some streakiness on the UV exposed yarn surfaces which were highlighted by brightening the images (Figure 46 and Figure 47). The UV light may have caused carbon to disassociate from the CNT molecules to form a thin layer of amorphous carbon. The FIB was used to cross-section a CNT fiber within one of the UV exposed yarns. The cross-sectioned UV fiber is shown in Figure 48. The top of the fiber shows a distinct, darkened crust that is not present on the bottom half of the

fiber. The top of the fiber was exposed to the UV radiation whereas the bottom was not because it was buried within the bundle of fibers in the yarn. The darkened crust is most likely amorphous carbon induced by the UV radiation and the remaining microstructure of the cross-section appears to be unchanged from the exposure, which supports the other material characterization results which showed only small changes due to the UV radiation.

Energy dispersive x-ray spectroscopy measurements were taken on fibers of all exposure types which ruled out surface contamination in handling as the cause of the surface change. The x-ray spectroscopy measurements provided an elemental analysis of the surface of the CNT yarns. The results were indistinguishable and therefore not discussed further.

The AO exposed yarns (Figure 49-Figure 52) showed much more noticeable effects from the AO exposure. Long lengths of yarn show clear physical damage that presented itself as reduced fiber cross sections, deep pits, and frayed edges. The damage presented in the AO exposed yarn SEM images appears to be much more severe than those presented by Hopkins, *et al.* [11] and Misak, *et al.* [59]. The discrepancy in apparent fiber surface damage and change in tensile strength between the yarns studied herein and the CNT yarns studied in the works of Hopkins, *et al.* [11] and Misak, *et al.* [59] may be due to either their use of multi-walled CNT fibers, protection provided by proprietary post processing techniques by the yarn manufacturer, or the lack of chlorosulfonic acid which was present in the yarns studied herein. The microstructural characterization of the exposed CNT yarns studied herein suggests the need to completely

protect CNT materials from the space environment in LEO but that at higher orbits, where AO is not present, CNTs may do not require protection from UV radiation.

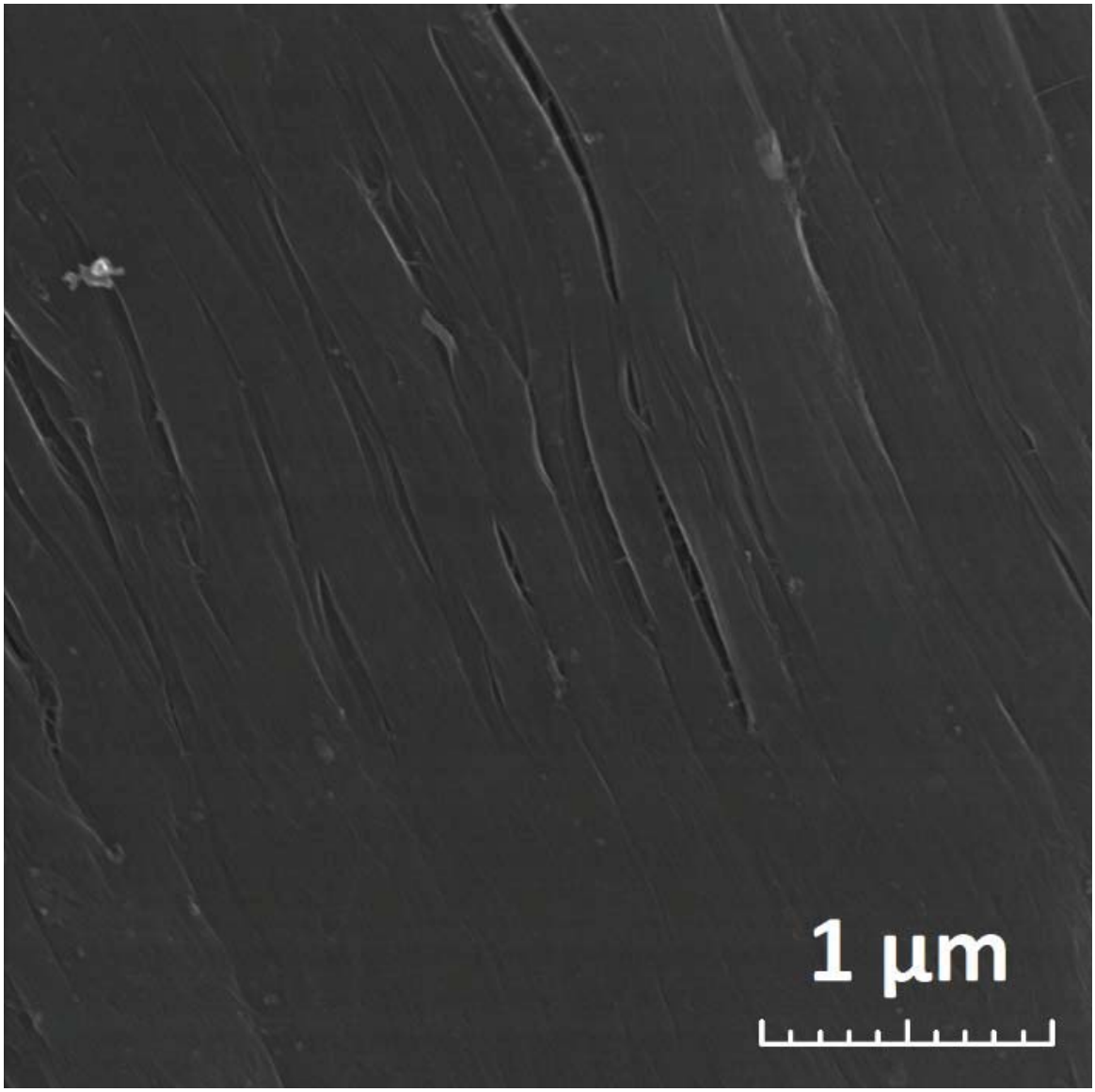

Figure 46: Pristine CNT fiber surface

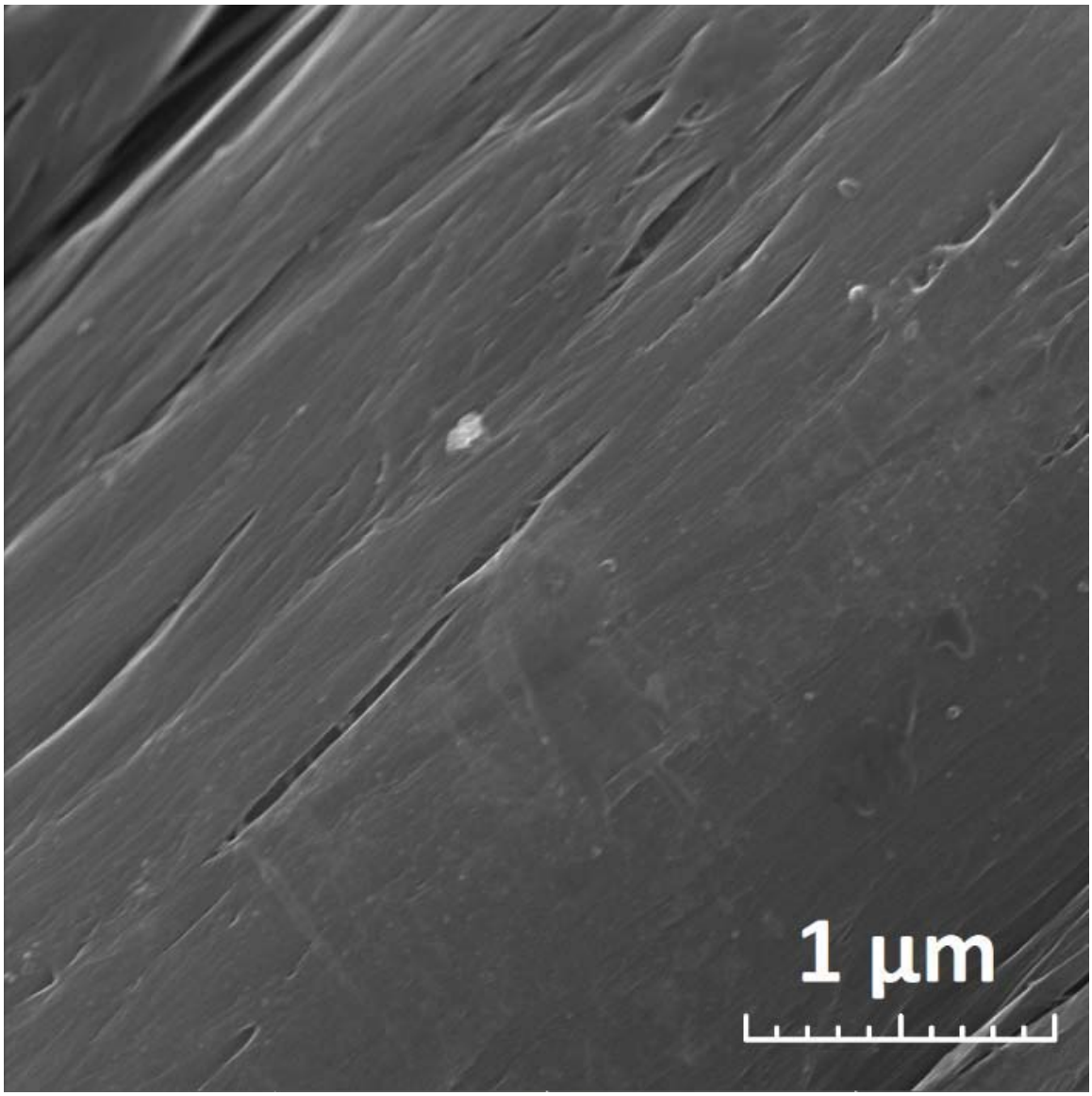

Figure 47: UV exposed CNT fiber surface

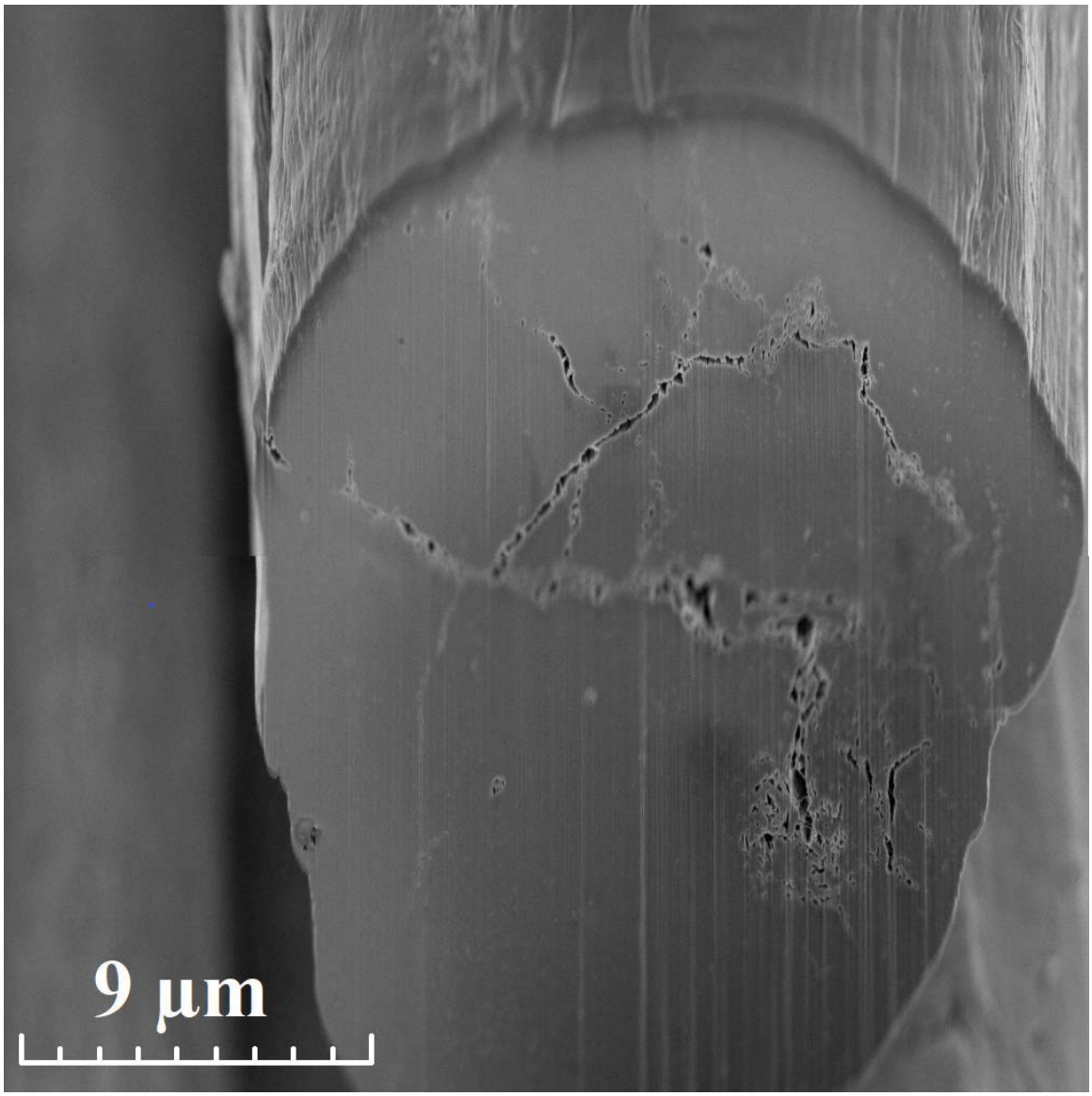

Figure 48: FIB Cross-Section of UV Exposed CNT Fiber

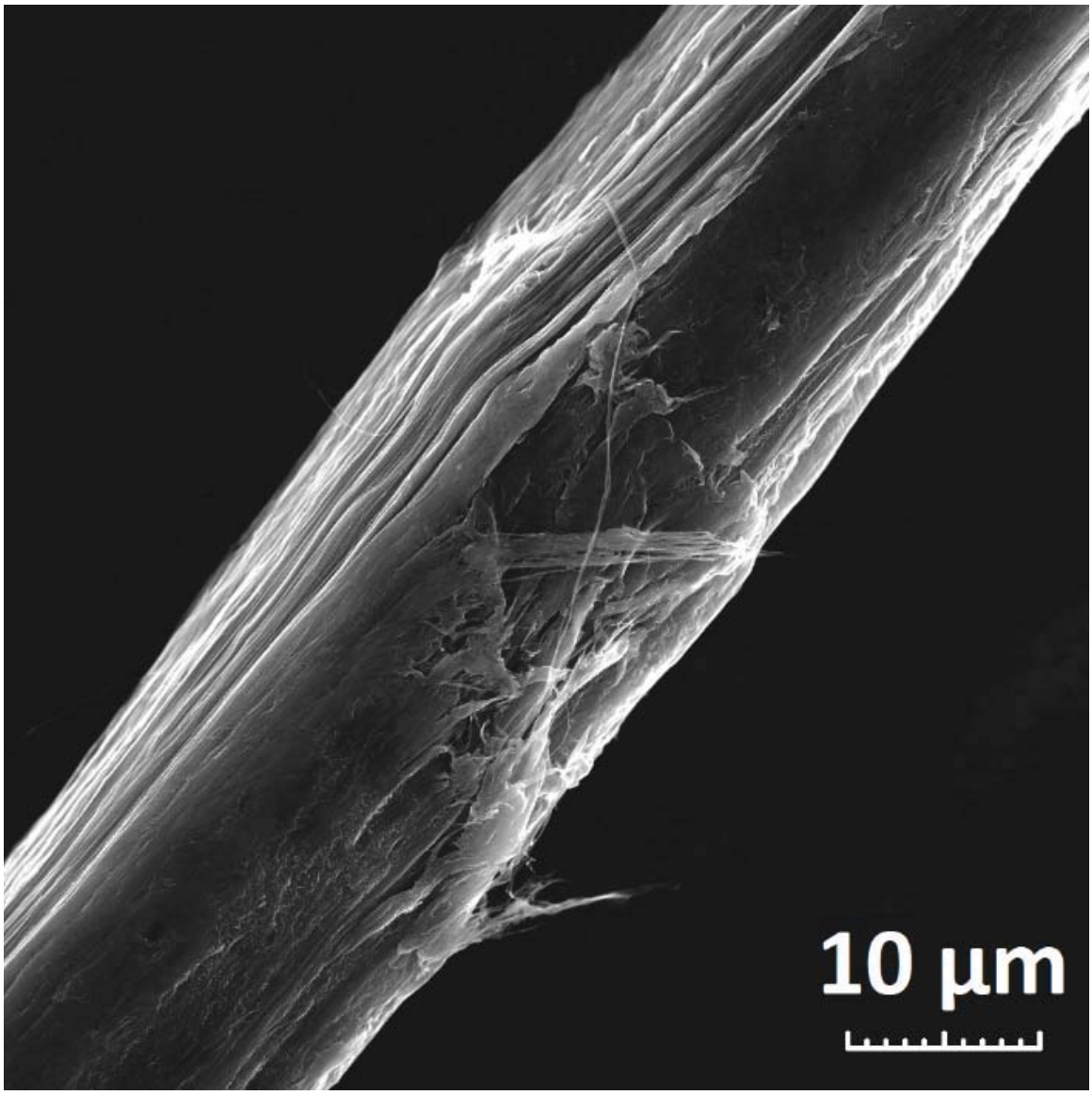

Figure 49: AO exposed CNT fiber showing surface erosion

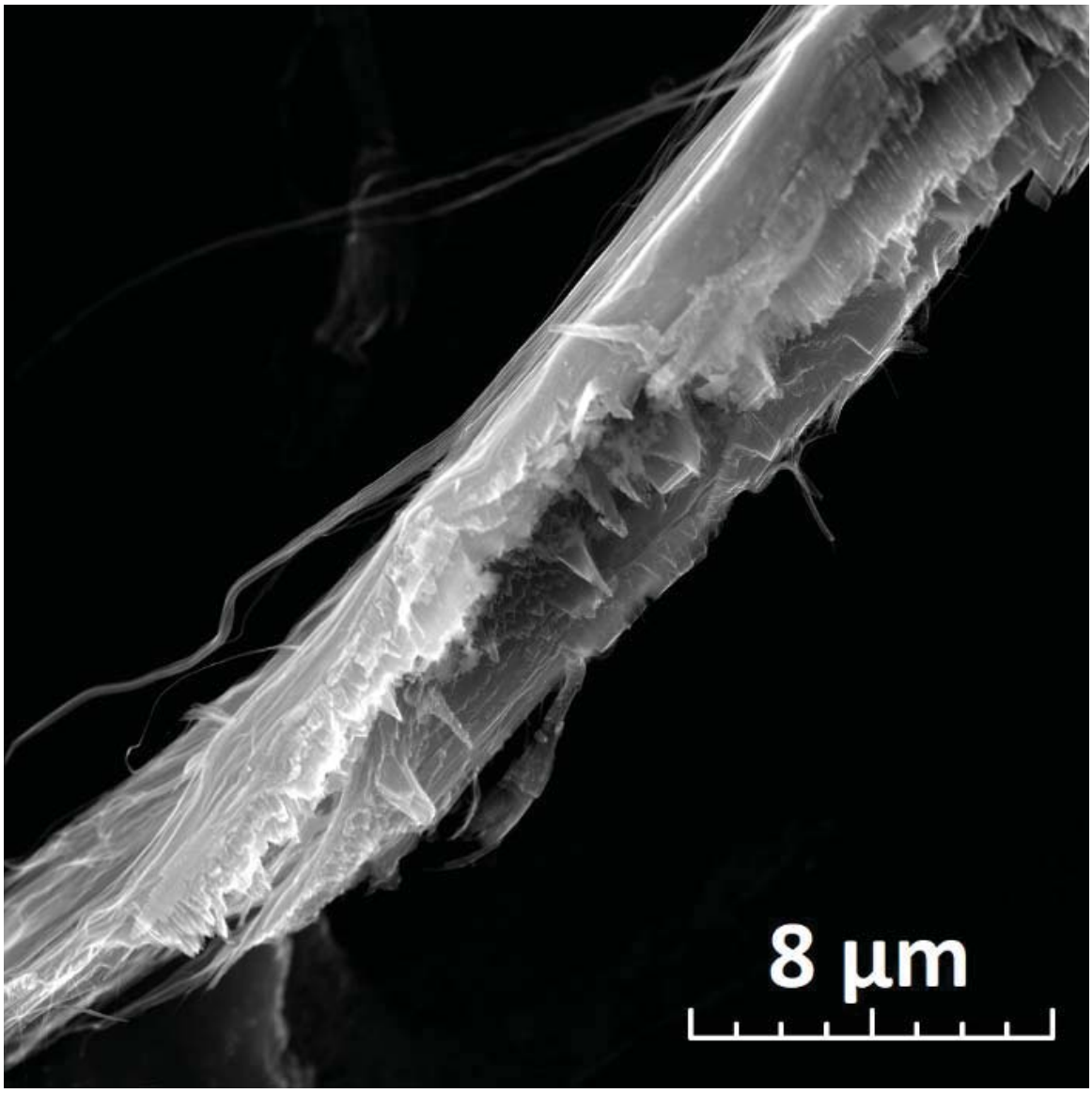

Figure 50: AO exposed and tensile tested CNT fiber with more severe surface erosion at fracture surface

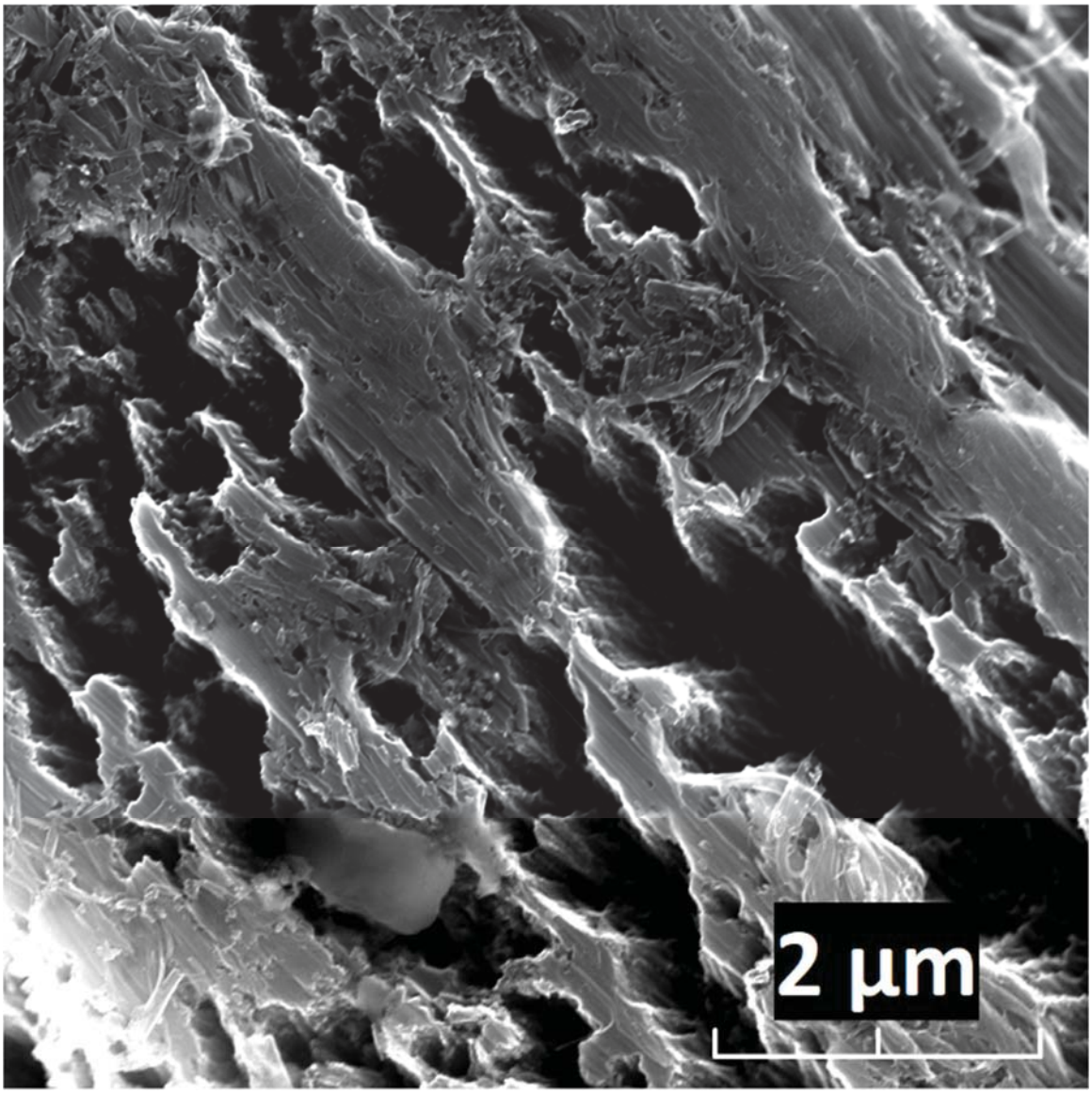

Figure 51: AO exposed CNT fiber showing surface erosion

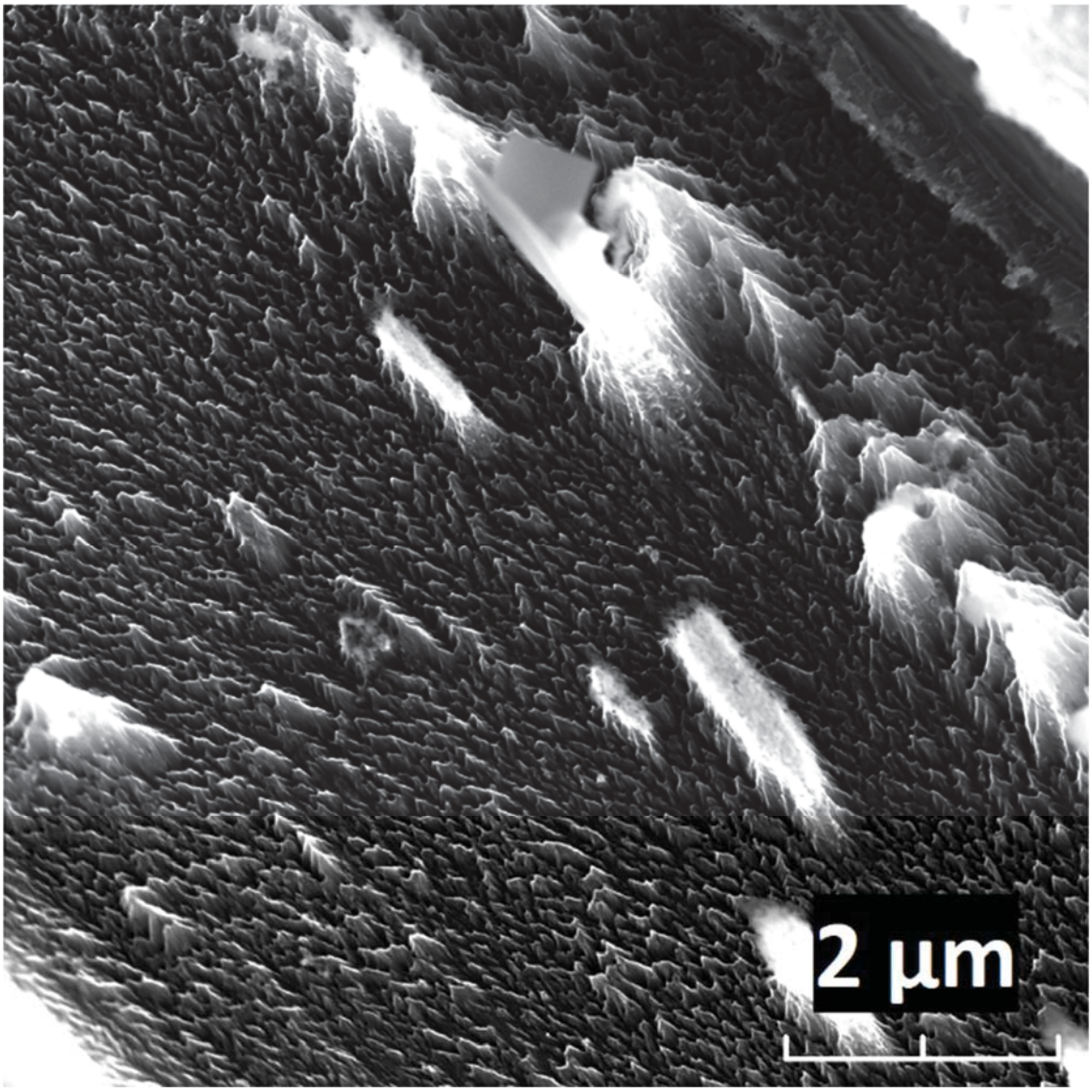

Figure 52: AO exposed CNT fiber showing surface erosion

Summary

This chapter covered the results of CNT fiber tensile testing, CNT fiber static loading, and the characterization of the effects of AO and UV exposures on the material properties of CNT yarns. Overall conclusions from the testing conducted herein along with recommendations for future work are presented in the following chapter.

V. Conclusions and Recommendations

Chapter Overview

This chapter concludes the discussion of the research conducted herein. A summary of the answers to the research questions posed in Chapter I is given. The significance of this work and future work which should follow this research are also presented.

Conclusions of Research

This research aimed to investigate three research objectives. The first was to determine the effects of microstructural defects on the mechanical properties of CNT fibers and determine whether these effects give rise to a dependence between fiber length and tensile strength. Single fiber tensile testing demonstrated a relationship between the fiber length and the tensile strength of CNT fibers. The fiber length and strength relationship was hypothesized to have resulted from the random distribution of voids of varying severity in the CNT fiber microstructure. FIB milling and SEM imagery were used to confirm the presence of cracks and voids of varying sizes in unstressed fibers. The empirical model developed to describe the dependence of strength upon length predicts that the strength of the fiber at length scales relevant to composite structures will not be significantly different than the strength measured on the tested CNT fibers. Weakest link theory was applied to the tensile strength data to test whether the theory provided a better statistical fit to all of the testing data versus applying statistical models to each gage length data set independently. Statistical model testing showed that the

weakest link theory was able to describe the different data sets with fewer parameters and sufficient goodness of fit.

The second objective was to determine the effect of the CNT fiber microstructure on the relationship between strain rate and tensile strength of the tested CNT fibers. The CNTs in the CNT fibers tested herein are bonded to each other by weak van der Waals forces so it was hypothesized that these fibers would exhibit strain rate dependent behavior which has been observed in similarly structured polymer fibers. Single fiber tensile tests with varying strain rates and single fiber static loading tests were conducted to investigate this behavior. These tests demonstrated the dependence of tensile strength on the strain rate and also demonstrated the large variability in time to failure of static loading tests. Coleman's [36] statistical approach to relate tensile strength and static loading behavior were found to apply to the mechanical behavior of CNT fibers studied herein. Microstructural examination was conducted with FIB milling and SEM imagery to study the development of voids and cracks in the CNT fiber microstructure. Void and crack development were observed to have dependence upon the time to failure, with greater development observed for longer test times.

The final objective was to determine the effects of the space environment on the material properties of CNT fibers. Laboratory AO and UV exposures were conducted on CNT yarns to simulate exposures in the LEO space environment. Tensile testing with simultaneous measurement of electrical resistance was conducted on pristine and exposed CNT yarns to characterize the effects of the exposures on the mechanical and electrical properties of the yarns. Raman spectroscopy, FIB milling, and SEM imagery were utilized to characterize the damage induced by both exposure types.

The mechanical and electrical testing revealed the deleterious effects of AO exposure and the minimal effects of intense UV exposure on the CNT yarns studied herein. The simultaneous mechanical and electrical characterization measurements revealed that the UV exposure resulted in a dramatic increase in the piezoresistive effect exhibited by the CNT fibers. This is the first such observation of the enhancement of the piezoresistive character of a CNT fiber. Raman spectroscopy revealed that both exposure types induced damage in the exposed yarn surfaces. FIB milling was utilized to reveal the cross-section of a UV exposed fiber. The cross-section showed that only the surface of the fiber was affected leaving the majority of the fiber unaltered. SEM imagery of the AO exposed specimens showed significant erosion of and damage to the yarn surfaces.

Significance of Research

The results of this research will equip spacecraft structural engineers with knowledge on how CNT fibers may be utilized in space structures. There were not any detailed studies on the mechanical behavior of CNT fibers produced by the modern fiber synthesis method prior this research, therefore this work will provide a baseline for future CNT fiber mechanical behavior research and space environment exposure research.

The characterization of the observed tensile strength-gage length relationship is useful for predicting the tensile strength and its variability of shorter gage length CNT fibers, which is useful for modeling fiber behavior in composites. The variable strain rate and static loading characterization work demonstrates a limitation on the strength of CNT fibers subjected to low strain rates and static loading; however, the downward trend in the observed effect with respect to the effect observed by Zhang, *et al.* [67] suggests that

further improvements and densification achieved in CNT fiber synthesis will further reduce the strain effect.

Finally, the space exposure characterization will inform how CNT fibers used in space structures should be protected to prevent their failure in service. UV radiation was found to penetrate less than a micrometer into the CNT fiber depth and not change the tensile strength or electrical conductivity of the CNT fibers. UV radiation was observed to have substantially increased the piezoresistive effect of the CNT fibers studied. This result indicates that this process may be used to safely enhance the piezoresistive character of CNT fibers enabling greater utilization of CNT fibers as strain sensing materials.

Atomic oxygen exposure was found to have a much more deleterious effect on the material properties of single-walled CNT fibers compared with the results obtained for multi-walled CNT fibers studied in previous research. This result indicates that multi-walled CNT materials are more appropriate for use in unprotected applications in LEO for limited duration missions.

Recommendations for Future Research

Future work should focus on the incorporation of wet-spun CNT fibers into composite structures to characterize their mechanical behavior while interacting with matrix materials. The gage length and strain rate effects observed and characterized herein may be extended to predict the behavior of CNT fibers in a matrix material and model the interaction between matrix and fiber. These models can then be tested with mechanical characterization of CNT fiber/polymer composites.

The preparation of fibers for incorporation into a composite matrix material is an important step that also requires study. The UV surface damage which was documented herein may influence the ability of CNT fibers to bond well with composite matrix materials. Surface functionalization by UV or others mean to promote matrix bonding behavior is an important field that has already received attention and will continue to grow as CNT fibers approach the mechanical strength of high-strength carbon fiber.

The effects of the space environment on composite structures which incorporate CNT fibers is also an important field which requires further development. Past research has touched on some impacts of CNTs on the matrix which limited the extent of UV damage, but requires on-going development as different types of CNTs are used as evidenced by the difference in behavior of single-walled versus multi-walled CNT fibers.

The effects of microstructural defects on CNT fiber tensile strength should be studied by non-destructive means during fiber loading to investigate how the observed defects deform and lead to fiber failure. Utilization of nano-computed-tomography is the only viable option for accomplishing this objective now which indicates that such a study will be very time intensive and require a great deal of measurements and different types of CNT fibers for comparison.

Finally, the piezoresistive effect modification accomplished by UV radiation was significant. This modification needs further study to understand the underlying mechanisms which caused the dramatic increase. Then further study may focus on utilizing the mechanisms to create a repeatable process to make CNT fibers an excellent piezoresistive material for future strain sensors. Following the identification and development of improvement mechanisms, CNT fibers which have been improved may

be incorporated into composite structures and test the viability of CNT fibers at multifunctional composite materials.

Summary

This research provides a first step into the understanding of the mechanical behavior of CNT fibers produced by the wet-spinning method. This work will inform future research into their mechanical behavior and provide feedback to fiber synthesis methods on the source of strength limitations. Space environment effects were also characterized for the first time for fibers spun by the wet-spinning method. These results will aid spacecraft designers in the utilization of these exceptional fibers.

Bibliography

[1] D. Tsentalovich, R. Headrick, F. Mirri, J. Hao, N. Behabtu, C. Young and M. Pasquali, "Influence of carbon nanotube characteristics on macroscopic fiber properties," *ACS applied materials & interfaces,* vol. 9, pp. 36189-36198, 2017.

[2] F. Mirri, N. Orloff, A. Forster, R. Ashkar, R. Headrick, E. Bengio, C. Long, A. Choi, Y. Luo, A. Hight Walker, P. Butler, K. Migler and M. Pasquali, "Lightweight, flexible, high-performance carbon nanotube cables made by scalable flow coating," *ACS applied materials & interfaces 8.7,* pp. 4903-4910, 2016.

[3] P. Jarosz, A. Shaukat, C. Schauerman, C. Cress, P. Kladitis, R. Ridgley and B. Landi, "High-performance, lightweight coaxial cable from carbon nanotube conductors," *ACS applied materials & interfaces 4.2,* pp. 1103-1109, 2012.

[4] P. Jarosz, A. Shaukat, T. Mastrangelo, C. Schauerman, C. Cress, R. Ridgley and B. Landi, "Coaxial cables with single-wall carbon nanotube outer conductors exhibiting attenuation/length within specification," *Micro & Nano Letters 7.9,* pp. 959-961, 2012.

[5] R. Burton, K. Brown and A. Jacobi, "Low-cost launch of payloads to low Earth orbit," *Journal of spacecraft and rockets 43.3,* pp. 1209-1214, 2006.

[6] D. Koelle, "Specific transportation costs to GEO—past, present and future.," *Acta Astronautica 53.4,* pp. 797-803, 2003.

[7] X. Zhang, S. Fujiwara and M. Fujii, "Measurements of thermal conductivity and electrical conductivity of a single carbon fiber," *International Journal of Thermophysics,* vol. 21.4, pp. 965-980, 2000.

[8] Dexmat. [Online]. Available: https://dexmat.com/. [Accessed 27 September 2018].

[9] M. Heaney, "Electrical Conductivity and Resistivity," in *Electrical Measurement, Signal Processing, and Displays*, CRC Press, 2003, pp. 7: 1-14.

[10] A. Lekawa-Raus, K. Koziol and A. Windle, "Piezoresistive Effect in Carbon Nanotube Fibers," *ACS Nano, 8, 11,* pp. 11214-11224, 2014.

[11] A. R. Hopkins, A. Labatete-Goeppinger, H. Kim and H. Katzman, "Space survivability of carbon nanotube yarn material in low Earth orbit," *Carbon 107,* pp. 77-86, 2016.

[12] B. Anderson and R. Smith, "Natural Orbital Environment Guidelines for Use in Aerospace Vehicle Development," NASA, Huntsville, 1994.

[13] M. Dresselhaus, G. Dresselhaus and P. Eklund, Science of Fullerenes and Carbon Nanotubes, San Diego: Academic Press, 1996.

[14] S. Iijima, "Helical microtubules of graphitic carbon," *Nature 354.6348,* pp. 56-58, 1991.

[15] B. Vigolo, A. Penicaud, C. Coulon, C. Sauder, R. Pailler, C. Journet, P. Bernier and P. Poulin, "Macroscopic fibers and ribbons of oriented carbon nanotubes," *Science 290.5495,* pp. 1331-1334, 2000.

[16] S. Ramesh, L. Ericson and V. Davis, "Dissolution of pristine single walled carbon nanotubes in superacids by direct protonation," *J. Phys. Chem. B 108,* pp. 8794-8798, 2004.

[17] L. Ericson, H. Fan, H. Peng, V. Davis, W. Zhou, J. Sulpizio, Y. Wang, R. Booker, J. Vavro, C. Guthy, A. Parra-Vasquez, M. Kim, S. Ramesh, R. Saini, C. Kittrell, G. Lavin, H. Schmidt, W. Adams, W. Billups and R. Smalley, "Macroscopic, Neat, Single-Walled Carbon Nanotube Fibers," *Science 305,* p. 1447, 2004.

[18] N. Behabtu, C. C. Young, D. E. Tsentalovich, O. Kleinerman, X. Wang, A. W. K. Ma, E. A. Bengio, R. F. ter Waarbeek, J. J. de Jong, R. E. Hoogerwerf, S. B. Fairchild, J. B. Ferguson, B. Maruyama, J. Kono, Y. Talmon, Y. Cohen, M. J. Otto and M. Pasquali, "Strong, light, multifunctional fibers of carbon nanotubes with ultrahigh conductivity," *Science 339.6116,* pp. 182-186, 2013.

[19] H. Zhu, C. Xu, D. Wu, B. Wei, R. Vajtai and P. Ajayan, "Direct synthesis of long single-walled carbon nanotube strands," *Science 296,* p. 884, 2002.

[20] Y.-L. Li, I. Kinloch and A. Windle, "Direct spinning of carbon nanotube fibers from chemical vapor deposition synthesis," *Science 304.5668,* pp. 276-278, 2004.

[21] K. Jiang, Q. Li and S. Fan, "Nanotechnology: Spinning continuous carbon nanotube yarns," *Nature 419.6909,* p. 801, 2002.

[22] M. Zhang, K. Atkinson and R. Baughman, "Multifunctional carbon nanotube yarns by downsizing an ancient technology," *Science 306.5700,* pp. 1358-1361, 2004.

[23] R. Headrick, D. Tsentalovich, J. Berdegue, E. Bengio, L. Liberman, O. Kleinerman, M. Lucas, Y. Talmon and M. Pasquali, "Structure-Property Relations in Carbon Nanotube Fibers by Downscaling Solution Processing," *Advanced Materials,* vol. 30, p. 1704482, 2018.

[24] C. C. Chang, I. -K. Hsu, M. Aykol, W. -H. Hung, C. -C. Chen and S. B. Cronin, "A New Lower Limit for the Ultimate Breaking Strain of Carbon Nanotubes," *ACS Nano, 4, 9,* pp. 5095-5100, 2010.

[25] B. Peng, M. Locascio, P. Zapol, S. Li, S. Mielke, G. Schatz and H. Espinosa, "Measurements of near-ultimate strength for multiwalled carbon nanotubes and irradiation-induced cross-linking improvements," *Nat. Nanotechnol. 3,* p. 626, 2008.

[26] K. Koziol, J. Vilatela, A. Moisala, M. Motta, P. Cunniff, M. Sennett and A. Windle, "High-performance carbon nanotube fiber," *Science 318.5858,* pp. 1892-1895, 2007.

[27] X. L. Q. Zhang, Y. Tu, Y. Li, J. Coulter, L. Zheng, Y. Zhao, Q. Jia, D. Peterson and Y. Zhu, "Strong carbon-nanotube fibers spun from long carbon-nanotube arrays," *Small 3,* p. 244, 2007.

[28] A. Rao, S. Tawfick, M. Bedewy and A. Hart, "Morphology-dependent load transfer governs the strength and failure mechanism of carbon nanotube yarns," *Extreme Mechanics Letters, 9,* pp. 55-65, 2016.

[29] L. Zhu, J. Wang and F. Ding, "The Great Reduction of a Carbon Nanotube's Mechanical Performance by a Few Topological Defects," *ACS Nano, 10,* pp. 6410-6415, 2016.

[30] M. Ouyang, J. Huang, C. Cheung and C. Lieber, "Atomically resolved single-walled carbon nanotube intramolecular junctions," *Science 291,* pp. 97-100, 2001.

[31] B. Yakobson, G. Samsonidze and G. Samsonidze, "Atomistic theory of mechanical relaxation in fullerene nanotubes," *Carbon 38,* p. 1675, 2000.

[32] M. Yu, O. Lourie, M. Dyer, K. Moloni, T. Kelly and R. Ruoff, "Strength and breaking mechanism of multiwalled carbon nanotubes under tensile load," *Science 287,* pp. 637-640, 2000.

[33] W.-L. Deng, W. Qiu, Y.-L. Kang, J.-G. Guo, Y.-L. Li and S.-S. Han, "Multi-Scale Experiments and Interfacial Mechanical Modeling of Carbon Nanotube Fiber," *Experimental Mechanics, 54,* pp. 3-10, 2014.

[34] F. Peirce, "Tensile tests for cotton yarns:“the weakest link” theorems on the strength of long and of composite specimens," *J. Textile Inst.,* vol. 17, p. 355, 1926.

[35] W. Weibull, "A Statistical Theory of the Strength of Materials," *Ing. Vet. Ak. Handl.,* 1939.

[36] B. Coleman, "Statistics and Time Dependence of Mechanical Breakdown in Fibers," *Journal of Applied Physics,* vol. 29, p. 968, 1958.

[37] A. Tobolsky and H. Eyring, "Mechanical Properties of Polymeric Materials," *The Journal of Chemical Physics,* vol. 11, p. 125, 1943.

[38] A. Watson and R. Smith, "An examination of statistical theories for fibrous materials in the light of experimental data," *Journal of Materials Science,* vol. 20, pp. 3260-3270, 1985.

[39] K. Naito, J. Yang, Y. Tanaka and Y. Kagawa, "The effect of gauge length on tensile strength and Weibull modulus of polyacylonitrile (PAN)- and pitch-based carbon fibers," *Journal of Materials Science,* vol. 47, pp. 632-642, 2012.

[40] Padgett, W.J., "Weibull Analysis of the Strength of Carbon Fibers Using Linear and Power Law Models for the Length Effect," *Journal of Composite Materials,* vol. 29, pp. 1873-1884, 1995.

[41] D. Wilson, "Statistical tensile strength of Nextel 610 and Nextel 720 fibers," *Journal of Materials Science,* vol. 32, pp. 2535-2542, 1997.

[42] A. De and K. Phani, "Gauge Length Effect on the Strength of Silicon Carbide and Sapphire Filaments," *Journal of Composite Materials,* vol. 24, pp. 220-232, 1990.

[43] G. Sun, J. Pang, J. Zhou, Y. Zhang, Z. Zhan and L. Zheng, "A modified Weibull model for tensile strength distribution of carbon nanotube fibers with strain rate and size effects," *Applied Physics Letters,* vol. 101, p. 131905, 2012.

[44] G. C. B. Amaniampong, "Statistical variability in the strength and failure strain of aramid and polyester yarns," *Journal of Materials Science,* vol. 29, pp. 5141-5152, 1994.

[45] R. Smith and S. Phoenix, "Asymptotic Distributions for the Failure of Fibrous Materials Under Series-Parallel Structure and Equal Load-Sharing," *Journal of Applied Mechanics,* vol. 48, pp. 75-82, 1981.

[46] H. Wagner, S. Phoenix and P. Schwartz, "A Study of Statistical Variability in the Strength of Single Aramid Filaments," *Journal of Composite Materials,* vol. 18, pp. 312-338, 1984.

[47] E. Castillo, Extreme Value Theory in Engineering, London: Academic Press, Inc., 1946.

[48] B. Coleman, "On the Strength of Classical Fibres and Fibre Bundles," *Journal of the Mechanics and Physics of Solids,* vol. 7, pp. 60-70, 1958.

[49] P. Schwartz, A. Netravali and S. Sembach, "Effects of Strain Rate and Gauge Length on the Failure of Ultra-High Strength Polyethylene Fibers," *Textile Research Institute,* pp. 502-508, 1986.

[50] B. Gao, Y. Chen, M. Fuhrer, D. Glattli and A. Bachtold, "Four-point resistance of individual single-wall carbon nanotubes," *Phys. Rev. Lett., 95, 19,* p. 196802, 2005.

[51] B. Wei, R. Vajtai and P. Ajayan, "Reliability and current carrying capacity of carbon nanotubes," *Appl. Phys. Lett., 79, 8,* pp. 1172-1174, 2001.

[52] H. Duckworth, Electricity and Magnetism, New York: Holt, Rinehart and Winston, 1960.

[53] H. Zhao, Y. Zhang, P. Bradford, Q. Zhou, Q. Jia, F. Yuan and Y. Zhu, "Carbon nanotube yarn strain sensors," *Nanotechnology,* vol. 21, p. 305502, 2010.

[54] C. Perry and H. Lissner, The Strain Gage Primer, New York: Mc-Graw-Hill, Inc., 1955.

[55] P. Bridgman, "The effect of tension on the transverse and longitudinal resistance of metals," *Proc. Am. Acad. Arts Sci. 60,* pp. 423-449, 1925.

[56] J. Cao, Q. Wang and H. Dai, "Electromechanical properties of metallic, quasimetallic, and semiconducting carbon nanotubes under stretching," *Physical review letters 90.15,* p. 157601, 2003.

[57] J. Yang and K. de Groh, "Materials Issues," *MRS bulletin 35,* 2010.

[58] D. Edwards, A. Tighe, M. van Eesbeek, Y. Kimoto and K. de Groh, "Overview of the natural space environment and ESA, JAXA, and NASA materials flight experiments," *MRS bulletin 35.01,* pp. 25-34, 2010.

[59] H. Misak, V. Sabelkin, S. Mall and P. Kladitis, "Thermal fatigue and hypothermal atomic oxygen exposure behavior of carbon nanotube wire," *Carbon 57,* pp. 42-49, 2013.

[60] H. E. Misak and S. Mall, "Characterization of carbon nanotube yarn after exposure to hyperthermal atomic oxygen and thermal fatigue," *Advances in Space Research 58.11,* pp. 2385-2392, 2016.

[61] J. Pitman, Probability, New York: Spinger, 2006.

[62] F. Massey, "The Kolmogorov-Smirnov Test for Goodness of Fit," *Journal of the American Statistical Association,* vol. 46, no. 253, pp. 68-78, 1951.

[63] Y. Pawitan, In All Likelihood, Oxford: Oxford University Press, 2001.

[64] S. van der Zwaag, "The Concept of Filament Strength and the Weibull Modulus," *Journal of Testing and Evaluation,* vol. 17, no. 5, pp. 292-298, 1989.

[65] B. Epstein, "Statistical Aspects of Fracture Problems," *Journal of Applied Physics,* vol. 19, pp. 140-147, 1948.

[66] W. Knoff, "Combined weakest link and random defect model for describing strength variability in fibres," *Journal of Materials Science,* vol. 28, pp. 931-941, 1993.

[67] Y. Zhang, L. Zheng, G. Sun, Z. Zhan and K. Liao, "Failure mechanisms of carbon nanotube fibers under different strain rates," *Carbon,* vol. 50, pp. 2887-2893, 2012.

[68] X. Zhang, Q. Li, T. Holesinger, P. Arendt, J. Huang, P. Kirven, T. Clapp, R. DePaula, X. Liao, Y. Zhao, L. Zheng, D. Peterson and Y. Zhu, "Ultrastrong, stiff, and lightweight Carbon-Nanotube fibers," *Advanced Materials,* vol. 19, p. 4198, 2007.

[69] H. Wagner, P. Schwartz and S. Phoenix, "Lifetime statistics for single Kevlar 49 filaments in creep-rupture," *Journal of Materials Science,* vol. 21, pp. 1868-1878, 1986.

[70] C. Miko, M. Milas, J. Seo, R. Gaal, A. Kulik and L. Forro, "Effect of ultraviolet light irradiation on macroscopic single-walled carbon nanotube bundles," *Applied Physics Letters,* vol. 88, pp. 151905:1-3, 2006.

[71] W. Zhou, J. Vavro, K. Guthy, K. Winey, J. Fischer, L. Ericson, S. Ramesh, R. Saini, V. Davis, C. Kittrell, M. Pasquali, R. Hauge and R. Smalley, "Single wall carbon nanotube fibers extruded from super-acid suspensions: preferred orientation, electrical and thermal transport," *J. Appl. Phys. 95,* p. 649, 2004.

[72] M. A. Cullinan and M. L. Culpepper, "Carbon nanotubes as piezoresistive microelectromechanical sensors: Theory and experiment," *Physical review B 82.11,* p. 115428, 2010.

REPORT DOCUMENTATION PAGE

Form Approved
OMB No. 074-0188

1. REPORT DATE *(DD-MM-YYYY)*	2. REPORT TYPE	3. DATES COVERED *(From – To)*
30-10-2018	Dissertation	August 2015 – October 2018

TITLE AND SUBTITLE

Carbon Nanotube Fibers: Mechanical Behavior and the Effects of the Space Environment

5a. CONTRACT NUMBER

5b. GRANT NUMBER

5c. PROGRAM ELEMENT NUMBER

6. AUTHOR(S)

Kemnitz, Ryan A., Major, USAF

5d. PROJECT NUMBER

5e. TASK NUMBER

5f. WORK UNIT NUMBER

7. PERFORMING ORGANIZATION NAMES(S) AND ADDRESS(S)
Air Force Institute of Technology
Graduate School of Engineering and Management (AFIT/ENY)
2950 Hobson Way, Building 640
WPAFB OH 45433-8865

8. PERFORMING ORGANIZATION REPORT NUMBER

AFIT-ENY-DS-18-D-036

9. SPONSORING/MONITORING AGENCY NAME(S) AND ADDRESS(ES)
Intentionally left blank

10. SPONSOR/MONITOR'S ACRONYM(S)

N/A

11. SPONSOR/MONITOR'S REPORT NUMBER(S) N/A

12. DISTRIBUTION/AVAILABILITY STATEMENT
DISTRUBTION STATEMENT A. APPROVED FOR PUBLIC RELEASE; DISTRIBUTION UNLIMITED.

13. SUPPLEMENTARY NOTES
This material is declared a work of the U.S. Government and is not subject to copyright protection in the United States.

14. ABSTRACT

Carbon nanotube materials are promising multifunctional materials for incorporation into aerospace structures because of their high tensile strength, high electrical conductivity, and low density. This research aimed to characterize the mechanical failure mechanisms of carbon nanotube fibers and examine the effects of the space environment on their material properties. Tensile tests were conducted at varying strain rates and on fibers of varying gage lengths to examine the underlying molecular failure mechanisms and impact of defects on fiber strength. Tensile strength and elastic modulus were observed to increase with increasing strain rate and decrease with increasing gage length. The observed effects were similar to those observed for polymeric fiber materials. Atomic oxygen exposure was found to severely degrade the tensile strength and electrical conductivity of CNT yarns after an exposure equivalent to one year in Low Earth Orbit. Intense ultraviolet radiation did not significantly impact the mechanical or electrical properties of the fibers after an exposure equivalent to 3 years in Low Earth Orbit.

15. SUBJECT TERMS
Carbon nanotubes, Gage length effects, Strain rate effects, Static Loading, Microstructural analysis, Space Effects,

16. SECURITY CLASSIFICATION OF:			17. LIMITATION OF ABSTRACT	18. NUMBER OF PAGES	19a. NAME OF RESPONSIBLE PERSON
a. REPORT	b. ABSTRACT	c. THIS PAGE			Carl R. Hartsfield, AFIT/ENY
U	U	U	UU	154	19b. TELEPHONE NUMBER *(Include area code)* (937) 255-6565, ext 4667 (NOT DSN) (carl.hartsfield@afit.edu)

Standard Form 298 (Rev. 8-98)
Prescribed by ANSI Std. Z39-18